UNIVERSITÀ DEGLI STUDI DI TORINO

DIPARTIMENTO DI BIOTECNOLOGIE MOLECOLARI E SCIENZE PER LA SALUTE

MOLECULAR BIOTECHNOLOGY CENTER "GUIDO TARONE"

TESI DI DOTTORATO

KIAA1217 is a novel protein in the synapse that interacts with PSD-95 and Shank3 and controls dendritic spines' number and morphology

Supervisor
prof.ssa **Paola DEFILIPPI**

Ph.D. **Candidate**
Alessandro MORELLATO

ANNO ACCADEMICO 2021-2022

SUMMARY

ABSTRACT

The synapse organization and the postsynaptic density (PSD) region, with the appropriate localization of receptors, ion channels, structural proteins, and signaling molecules, is crucial for proper synaptic transmission and function. Alteration of the synaptic function due to the abnormal expression or localization of specific components has been associated with neurological disabilities like schizophrenia and autism spectrum disorder, cognitive impairment, and neurodegenerative diseases. Here we analyze the role of the KIAA1217 (hSKT) protein, the human homolog of the murine sickle tail, Skt, gene, as a new highly expressed synapse component through the behavioral and electrophysiological characterization of Skt total knock-out ($Skt^{-/-}$) mice. We also study the functional molecular interactions of SKT with the principal post-synaptic components, such as the PSD-95 (the most abundant protein in the PSD) and with components of the Shank family. Primary cultured neurons from $Skt^{-/-}$ embryos showed a decreased total dendritic spines number, with a reduction of mature mushroom spines and a concomitant increase in immature filopodia spine structure. MEA analysis from primary hippocampal cultures was characterized by a ~~delay in~~ neuronal synchronization and maturation delay. Moreover, the Puzzle Box test revealed that $Skt^{-/-}$ mice present impairment in cortical function, suggesting possible ~~defects in~~ cognitive processes and memory establishment defects. Through biochemical approaches, we also found that SKT interacts with the PDZ domain of PSD-95 and with the Shank family member Shank3. This work puts the cellular and molecular basis for further investigating the role of this scaffold protein in the dendritic spine, and its relevance in signal transduction through the synapse. ~~All~~ together, these data allow us to hypothesize that SKT is a new player in the structural and functional organization of the PSD and that its absence is linked to alterations of synaptic plasticity.

INTRODUCTION

GENERAL INTRODUCTION AT THE CNS

The nervous system of many vertebrates and invertebrates can be divided into the central nervous system (CNS) and the peripheral nervous system. The brain is the main component of the CNS. It is composed of morphologically and functionally distinct structures, such as the cortex, the hippocampus, the striatum, the amygdala, the thalamus, and the hypothalamus. The brain comprises two categories of cells: neurons and glia. A typical neuron shows two neuronal processes: a long, thin process called the axon that extends far beyond the cell body or the soma; and dendrites, thick, tree-like processes found near the soma. The extremity of the axons are characterized by the presynaptic terminals, specialized structures that participate in the transfer of information between neurons; in contrast, dendrites are characterized by small protrusions called dendritic spines, which are also involved in the transfer of information between cells (Whitford et al., 2002). In neurons, structural integrity depends on two components of the cytoskeleton: filamentous actin (f-actin) and tubulin microtubules. In addition, there is a third structural element, the intermediate filaments, which in the neuron are called neurofilaments and are concentrated in the axon, giving it stability. The f-actin is mainly concentrated in the peripheral districts of the cell, such as the presynaptic terminals and the dendritic spines; actin is also present in the growth cones of axons and dendrites. On the other hand, the microtubules are the main component of the axon and dendrite trunk and play an essential role in the remote transport of cellular components, including synaptic vesicles, thanks to the association of particular motor proteins (kinesins and dyneins).

The development of CNS neurons is studied by generating primary neuronal cultures obtained from the hippocampus or the cortex of mouse/rat embryos. Neuronal development of cultured hippocampal neurons is classified into five stages: lamellipodia formation, creation of minor processes, axonal outgrowth, dendritic outgrowth, and maturation with the establishment of dendritic spines (Banker, 2018).

The dendrites of neurons are highly branched, and the extent of the dendritic tree's arborization correlates with the neurons' inputs and processes. Consequently,

the development of dendritic arbors is a crucial process that fundamentally impacts the establishment and function of neuronal circuits in the brain. The axonal and dendritic formation and dendritic spines maturation are strictly regulated by actin and microtubule dynamics, and this regulation is mainly driven by Rho GTPases activity, particularly RhoA, Rac1, and Cdc42 (Van Aelst and Cline, 2004). The signals that control Rho GTPases in neurons in vivo are still largely unclear. However, several specific brain-derived growth factors regulate Rho GTPases during axon growing (Dickson, 2001) and outgrowth (Luo, 2000; Luo et al., 1996b; Yamashita et al., 1999). Moreover, the Rho GTPases coupled with NMDAR activity are fundamental for dendrite branching and dendritic spines plasticity (Lee et al., 2000); (Nakayama et al., 2000; Rajan and Cline, 1998; Ruchhoeft et al., 1999; Tashiro et al., 2000; Threadgill et al., 1997; Wong et al., 2000). The morphogenesis in neurons is achieved through the mutual interaction of different Rho GTPases (Li et al., 2002b; Luo, 2000). This cooperation occurs via coordinated actions of individual GTPases that, in turn, specifically act on the cytoskeleton or as crosstalk between different GTPase pathways. Moreover, such multiple interactions could depend on the differential regulation of common targets by many small GTPases (Bishop and Hall, 2000). In addition, Rho GTPases can also modulate the activity of other Rho GTPases: for instance, RhoA activity is increased by Rac activation, while Rac is inhibited by RhoA activation. Finally, the effects of RhoA activity are the inhibition of actin branching, whereas Rac and Cdc42 promote additional actin branching and actin cytoskeleton stabilization. When neurons are non-stimulated, RhoA activity is high, sustaining low levels of Rac activity and thus restricting the growth of the dendritic arbor. In contrast, glutamatergic synaptic activity inhibited RhoA activity, while Rac was triggered, thus promoting dendritic arbor development (Li et al., 2002a; Li et al., 2002b). Overall, the correct brain development is highly dependent on space and time coordinated actions of genetic and environmental processes, and any aberration leads to neurodevelopmental disorders, Intellectual disability (ID), and autism spectrum disorders (ASDs) that affect 5% of the population, thus presenting a significant challenge to society.

THE SYNAPSE

Signaling between neurons in the human CNS is accomplished through a highly interconnected network of axon-dendrite contacts in which the neuronal axon contacts the dendrite (or the soma) of a targeted neuron. This unit is defined as the synapse and is subdivided into presynaptic and postsynaptic elements, both essential in conveying electrical and neurochemical pieces of information. The synapses can be classified according to their nature (chemical or electrical), localization, or action (excitatory or inhibitory). The excitatory synapse is constituted by a presynaptic and a postsynaptic terminal, separated by the synaptic space (defined as synaptic cleft) in which the neurotransmitters are released. The typical excitatory neurotransmitter is glutamate, freed from the presynaptic side vesicles. The glutamate receptors are present at the postsynaptic site, divided into ionotropic and metabotropic receptors. Ionotropic glutamate receptors are integral membrane proteins composed of four large subunits (>900 residues) that form a central ion channel pore (Traynelis et al., 2010). They are subdivided into AMPA (α-amino-3-hydroxy-5-methyl-4-isoxazole-propionate), kainate, NMDA (N-methyl-d-aspartate), and δ receptors (Traynelis et al., 2010) and the metabotropic mGlur receptors. The information arrives at the presynaptic terminal like a membrane action potential that determines the recruitment of presynaptic vesicles, their fusion to the plasma membrane, and the release of the proper neurotransmitter. Next, these molecules bind the postsynaptic receptors to transmit the information inside the target cell.

Synapses are the most complex cellular compartment in neurons: in fact, the synapse proteome from rodents consists of thousands of proteins assembled in multimolecular complexes, which compete for protein-protein interaction and protein regulation. The synapses act as biological and biochemical machines: presynaptic action potentials generation, synaptic vesicle trafficking, neurotransmitter release, neurotransmitter receptor activation, and postsynaptic signal propagation, as well as numerous other collateral processes that are necessary to establish synapses to modify their efficacy in responding to the stimuli of plasticity. In addition, the synapses contain all the apparatus to act as an independent cell compartment, i.e., they contain

ribosomes and endoplasmic reticulum for local protein synthesis. The mRNAs originate from the cell soma and can be stored in the vesicles localized at the postsynaptic side, where they are released and fast translated when required into proteins essential to support synapse growth.

Many synapses in the mammalian CNS exhibit long-lasting forms of synaptic plasticity that are strictly correlated to a different form of behavior, among them also learning and memory. In particular, long-term potentiation (LTP) and long-term depression (LTD) at the excitatory glutamate synaptic terminal represents the widely studied mechanism of synaptic plasticity, providing synapse reinforcement in case of LTP, or weakening for LTD in a learning-based manner (Iasevoli et al., 2013). A precise cascade of events occurs during LTP: after the neurotransmitter glutamate is released from the presynaptic terminal, it binds to the AMPA receptor in the postsynaptic membrane. These ion channels open, and Na^+ ions could flow into the postsynaptic terminal. This increase in positive ions induces the AMPA-mediated depolarization that causes the removal of Mg^{2+} from the NMDA ionotropic receptor. This event, and the glutamate binding to the NMDAR, induces the complete channel opening. Thus, the Na^+ and Ca^{2+} ions flow into the postsynaptic compartment. Calcium increase acts as a second messenger to activate calmodulin as CamKII. These proteins phosphorylate several components in the postsynaptic site, inducing protein-protein interaction, assembly of macromolecular signaling complexes, and finally, the reorganization of the synaptic cytoskeleton necessary for the morphological plasticity of the synapse. This complexity is found in humans, primates, mice, ~~or~~ rats.

The classical chemical synapse comprises presynaptic and postsynaptic elements; this scheme evolved in the last twenty years. In addition to neurons~~,~~ this new model includes astrocytes, NG2 glia, and microglial cells that play critical roles in regulating plasticity (Farhy-Tselnicker and Allen, 2018; Perea et al., 2009). More recently, the idea of the "tetrapartite synapse," made of presynaptic and postsynaptic elements, glial processes, and extracellular matrix (ECM), was proposed~~,~~ (Dityatev and Rusakov, 2011; Song and Dityatev, 2018).

THE PRESYNAPSE

A pool of synaptic vesicles (SVs) envelopes small molecules called neurotransmitters in the presynaptic terminal. When a stimulated neuron triggers an action potential, it opens presynaptic voltage-gated Ca^{2+} channels. The calcium influx controls calcium-dependent proteins, called Calmodulins, that regulate small G proteins such as Rab3a (Pavlos et al., 2010) to promote SV exocytosis and postsynaptic receptor activation.

This event is confined in a specific section of the presynaptic plasma membrane defined as the "active zone." Here P/Q and N-type Cav2 voltage-gated Ca2.1 channels are clustered to maximize the SV release when necessary (Benarroch, 2013). The presynaptic active zone achieves several roles for neurotransmitter release: 1) it is the presynaptic region dedicated to docking and priming the SV; 2) it favours synchronous and fast excitation and SV release coupling, contributing to the recruitment of calcium channels in specific presynaptic membrane domains; 3) it allows the proper location of the presynaptic compartment with the postsynaptic membrane and its specialized receptors; 4) it coordinates short and long term presynaptic plasticity directly (by second messengers) or indirectly (by recruiting proteins that control synaptic plasticity) (Sudhof, 2012). The final goal of all these functions is to finely regulate the SV exocytosis to promote the rapid neurotransmitter release and enlargement of the presynaptic terminal required for the information transmission and the proper function of the synapse. (Owald and Sigrist, 2009).

Almost all presynaptic functions deal with SV: in fact, in the nerve a trafficking cycle organized in different precise sequential steps can be observed. First, neurotransmitters are incorporated in SV, and these filled SVs cluster in the active zone. Then, SVs dock at the active zone and are primed and made competent, thanks to the calcium influx. At this point, SVs are ready and can fuse with the presynaptic membrane. Finally, the SVs are recycled through three different mechanisms: SVs remain docked near the synaptic plasma membrane and are reacidified and refilled with neurotransmitters (kiss and stay); SVs undock and recycle locally in the inner presynaptic site where they are supplied after reacidification (kiss and run); SVs could

be recycled via clathrin-coating pathway and pass through an endosomal intermediate or directly acidified and filled with neurotransmitter (Jahn and Fasshauer, 2012; Sudhof, 2004).

THE DENDRITIC SPINES AND THE POSTSYNAPSE

The dendritic spines are small protrusions originating from the dendritic shaft and are connected to the dendrite with a short neck. The formation of DSs starts once the dendritic arbor is complete, and the contact with the other neurons influences their plasticity properties. The DS density ranges from 0.2 to 3.5 spines per 1 um of the dendrite, and this number depends on the type of neurons, age, and localization along the dendritic shaft. DSs follow different stages of maturation. The immature form is called filopodial spine, formed by a long and thin structure with a restricted membrane area, low synaptic receptors composition, and low receptor-associated molecular complexes. These spines are not able to generate a proper synaptic transmission. Due to increased branching of the polymerized actin, the filopodial spine progresses towards a progressive enlargement of the head, expanding the synaptic "active zone." The synaptic site includes the membrane receptors and the postsynaptic density (PSD), where are localized the receptor-associated proteins essential for the postsynaptic pathway. This final stage of DS maturation is called mushroom spine, with the enlarged head. DS form is necessary for synaptic function; indeed, several neurological disorders are characterized by a significant decrease in mature mushroom spines, leading to electrophysiological anomalies. In literature is demonstrated that time-dependent changes in spine morphology are under regulation of glutamatergic synaptic activity (Engert and Bonhoeffer, 1999; Lendvai et al., 2000; Maletic-Savatic et al., 1999) and involve structural changes of the actin cytoskeleton (Fischer et al., 2000) that are finely controlled by Rho GTPases (Luo et al., 1996a; Nakayama et al., 2000; Tashiro et al., 2000). Furthermore, both GTPases activating proteins (GAPs) (Chen et al., 1998; Kim et al., 1998) and exchange factors (GEFs) (Penzes et al., 2001) are enriched in the postsynaptic density close of glutamate receptor and calcium/calmodulin-dependent protein kinase II (CaMKII) activity, to maximize signal transmission and regulation.

Beyond the emergence of the spines (spinogenesis), all the GTPases mentioned above continue to influence the plasticity of dendritic spines, modifying their shape and stability even with age. For instance, introducing a costively inactive Rac1 into

hippocampal neurons causes spine loss, indicating that Rac1 is crucial in long-term spine stability (Nakayama et al., 2000). In addition, Rac1 activates the WAVE family proteins among its downstream targets to stimulate the ARP2/3 complex. This complex is associated with F-actin in the core of the DS cytoskeleton, whose functions consist in nucleating new actin filament branches from existing actin filaments (Murakoshi et al., 2011).

In contrast to Rac1, activated Rho mutants or increased RhoA levels cause reductions in dendritic spine density (Koleske, 2013). RhoA inhibition or knockdown of the Rho activator guanine nucleotide exchange factor 1 (RhoGEF1) increases spine density (Tashiro et al., 2000). Inhibition of the primary Rho target Rho-associated protein kinase (ROCK) can block spine loss resulting from increased RhoA protein levels (Xing et al., 2012). Rho signaling through ROCK stimulates LIM kinase to phosphorylate Cofilin and inhibit its actin severing activity (Koleske, 2013; Xing et al., 2012).

THE PSD-95 ADAPTOR PROTEINS

Postsynaptic density 95 (PSD-95) protein 95, also known as SAP-90 (synapse-associated protein 90), is encoded from the drosophila melanogaster gene Disc Large Homolog 4 (Dlg 4) and is one of the principal structural proteins at the postsynaptic site (Migaud et al., 1998). PSD-95 is the most representative member of the membrane-associated guanylate kinase (MAGUK), which are scaffold proteins containing PDZ domains encoded by four genes (PSD-95/SAP90), PSD-93/chapsyn-110, SAP102, and SAP97 (Kim and Sheng, 2004). These proteins are all characterized by the presence of three different PSD-95/Dlg4/Zona Occludens 1, ZO-1 (PDZ) domain, one Src homology 3 (SH3) domain, and one Guanylate Kinase like (GK) domain (Kim and Sheng, 2004)). In particular, PSD-95 has a specific molecular structure that allows it to interact in an intermolecular and intramolecular fashion. It is described that the PDZ3 may interact loosely with SH3 (McGee et al., 2001), masking the proline binding domain (PBD) region and controlling the PSD-95 assembly. Furthermore, the correct conformation of PBD is the result of the combination ~~between~~of the SH3 and GK domains, thus affecting the intramolecular and intermolecular interactions and triggering an intricate molecular network in the PSD (Tavares et al., 2001).

In addition, it is also known that the N-terminal of PSD-95 interacts with other PSD-95 molecules allowing an expansion of the scaffolding region in the PSD. The accessibility of the N-terminal domain of PSD-95 is finely regulated by interaction with alpha-actinin1, which can bind and target PSD-95 near the PSD membrane: in the N-terminal region, two cysteines are thioesterificated with palmitate; when PSD-95 is palmitoylated, it could associate with postsynaptic membranes, that in turn favor PSD-95 multimerization, interaction with PSD ion channels and their clustering of the cell surface (Craven et al., 1999).

For instance, PSD-95 mediates AMPA receptors clustering at the synapse coupling to the accessory protein Stargazin, a transmembrane protein associated and regulated directly with AMPAR (Bats et al., 2007). PSD-95 function and localization are also dependent on phosphorylation at cysteines present at its N-terminal domain;

in particular, the kinase that phospholipases these sites is Cyclin-dependent kinase 5 (Cdk5) at its N-terminus, mediated by Cyclin-dependent kinase 5 (Cdk5) (Morabito et al., 2004). These phosphorylations inhibit PSD-95 multimerization and, in turn, PSD-95-mediated receptor clustering. In addition, many proteins have been discovered as interactors of PSD-95 on specific domains. For example, the PDZ domains bind the C-terminal of various proteins located at the cell-cell interface and associate with the receptors' subunits (like AMPAR's or NMDAR's subunits) (Hung and Sheng, 2002). This particular location within the neuron suggests an essential role for these PDZ-containing proteins in regulating synaptic contacts.

The SH3 and GK domains also mediate interactions of PSD-95 with several other scaffolding molecules. For instance, the GK domain interacts with A-kinase anchor protein AKAP5 (AKAP 79/150) (Bhattacharyya et al., 2009), and microtubule-associated protein 1A (MAP1a), and with another scaffold molecule in the PSD known as DLGAP1 (Dlg4 Associate protein, or GKAP) (Naisbitt et al., 1997), whereas the SH3 domain associates with the microtubule end binding proteins 3 (EB3) (Sweet et al., 2011).

Overall, PSD-95 could be considered the most crucial scaffold protein present in the PSD. Its central role in orchestrating the PSD lattice assembly is that PSD-95 is strictly linked to other scaffold proteins in the PSD, including the SH3 and ankyrin repeat-containing protein (Shank) and Homer1 (Kim and Sheng, 2004; Sheng and Kim, 2000; Sheng and Kim, 2002). Furthermore, these proteins are typically localized into the more profound (cytoplasmic) part of the PSD (Meyer et al., 2014), associated with additional signaling and cytoskeletal proteins.

THE SHANK ADAPTOR PROTEINS

The Shank proteins are large postsynaptic scaffolding proteins (about 200 kDa) and are the master regulator of the maturation of excitatory synapses, where they are crucial for proper synaptic development and function (Tu et al., 1999)), and tether and organize adaptor proteins located in the intermediate level of the synapse, in the broad layer of the PSD, from 20 to 80 nm from the postsynaptic membrane (Tao-Cheng et al., 2016). ~~In the mouse,~~ Shank proteins are encoded by the Shank1, Shank2, and Shank3 mouse genes (Lim et al., 1999).

Shank3 (also known as ProSAP2) is the best-studied of the three Shank protein family members (Monteiro and Feng, 2017). It is expressed in the whole brain with a peak of expression in the cerebral cortex and cerebellum (Bonaglia et al., 2001). Shank1 and Shank2 are widely expressed in early development, while Shank3 expression increases during postnatal development (Bockers et al., 2004). Shank3 can form protein complexes in a brain region-specific fashion, contributing to the related pathophysiological diversity of disorders (Solopov and Lunichkina, 1988). The scaffold role of Shank is embedded in its structure; in fact, Shank3 contains six domains for protein-protein interactions: protein domains of still unknown function 535 (DUF535), the ankyrin repeat domain (ANK); one SH3 domain; one PDZ domain, a proline-rich region (PRO) and sterile alpha motif (SAM) that allow Shank to form large sheets of protein stacked side by side.

Shanks members are abundant at the postsynaptic site of glutamatergic excitatory synapse. Both loss and overexpression of Shank result in defects in synaptic bouton number and maturation. In addition, Shank controls the internalization of Frizzled in a noncanonical Wnt signaling pathway, thus modulating the synaptic development. (Harris et al., 2016). Moreover, Shanks proteins target δ-Catenin in the DS and regulate its pathway interacting with other PSD proteins (Quitsch et al., 2005). Shank3 undergoes nucleus-synapse shuttling in an activity-dependent fashion. For example, Shank3 drives the entrance into the nucleus of proteins as β-Catenin and thus regulates the transcription of several genes ASD and SCZ related (Grabrucker et al., 2014). Haploinsufficiency or variants of Shank3 is associated with 22q13.3 deletion

syndrome (Bonaglia et al., 2001; Wilson et al., 2003) and causes the major neurodevelopmental features of Phelan-McDermid syndrome (Guilmatre et al., 2014), which is characterized by speech delay or absence, mental retardation, developmental delay and facial dysmorphisms (Boeckers et al., 2002; Phelan et al., 1993). These features are also related to autism spectrum disorders, intellectual disability, bipolar disorder, and schizophrenia (Meng et al., 2010). In addition, Shank3 is epigenetically regulated by MeCP2, a protein involved in the ASD-related Rett diseases (Waga et al., 2014).

Several mouse models with Shank3 loss were generated. These mice showed autism-like behavior, social deficits, altered interaction, and self-injuring due to repetitive grooming with diminished DS density (Bozdagi et al., 2010; Jiang and Ehlers, 2013; Peca et al., 2011). Moreover, Shank3 null mice exhibit reduced excitatory transmission (Yang et al., 2012) with diminished NMDAR synaptic distribution and function in the prefrontal cortex. From an electrophysiological point of view, null Shank3 primary culture displayed a reduced firing activity on the multi-electrode array (MEA) that evidenced an alteration in the excitation/inhibition balance. (Lu et al., 2016). Moreover, brain region-specific disruption of Shank3 results in altered cortical-striatal circuits and underpins socio-communicative impairments typically observed in ASD behaviors. (Bey et al., 2018; Pagani et al., 2019). Notably, early genetic restoration of wild-type Shank3 can recover wild-type mice behaviors.

Shank3's SH3 domain interacts with and mediates synaptic clustering of ASD-related voltage channel CaV1.3a (Chan et al., 2007), and this interaction is necessary for regulation in the cAMP pathway (Perfitt et al., 2020; Zhang et al., 2005). Mutations in the PDZ and SAM domains of Shank3 affect the interactions with postsynaptic partners Homer, Cortactin, Dynamin, and Abi-1; mutations in the N-terminal of Shank3 were found in ASD patients and altered the interaction with small Ras family GTPases (Guan et al., 2020; Hassani Nia and Kreienkamp, 2018). Variants of the Shank are causally associated with numerous neurodevelopmental and neuropsychiatric disorders, including autism spectrum disorder (ASD), bipolar disorder, intellectual disability, and schizophrenia SCZ.

Shank3 can act as a platform for assembling PSD protein complexes (Baron et al., 2006) brains region-specific, contributing to the different pathophysiological and

phenotypic diversity of disorders related to Shank3 mutations. The C-terminus of SHANK3 interacts with PSD95 associated protein 1 (SAPAP1; also known as GKAP1) and forms a ternary complex with PSD-95. In addition, Shank3 interacts with its PDZ domain with the glutamate receptor 1 (GluR1; also known as GRIA1) subunit of AMPA receptors (AMPARs), targeting the receptor at the synaptic sites and regulating its subunits composition (Ha et al., 2018; Hayashi and Majewska, 2005; Naisbitt et al., 1999; Tu et al., 1999; Uchino et al., 2006) and is linked through PSD-95 to NMADAR receptors that are necessary for synaptic transmission, and plasticity. Moreover, the PRD domain binds Cortactin (Durand et al., 2012) and Abp1 (actin-binding protein 1) at the tip of actin filaments (Qualmann et al., 2004), which plays a crucial role in actin dynamics and cytoskeleton regulation (Bockers et al., 2001; Haeckel et al., 2008).

Shank is also linked and regulated by the metabotropic receptors mGlur5 by Homer1 protein, which encodes for another PSD scaffold protein (Tu et al., 1999; Verpelli et al., 2011). Thus, Shank is a crucial hub for coupling ion and metabotropic channels to precisely control the synaptic plasticity during LTP or LTD. The carboxyterminal SAM domain of SHANK proteins is known to self-multimerize and is required to localize Shank3 and Shank2 to the PSD (Gundelfinger et al., 2006; Naisbitt et al., 1999). Besides all the proteins mentioned above, Shank members have several other interaction partners (Gundelfinger et al., 2006; Naisbitt et al., 1999). Shank3 deficiency induces NMDAR hypofunction and interferes with the RAC/PAK/cofilin actin signaling. Shank3 modulates the small GTPase Rac1 and CDC42 through the recruiting in the dendritic spine of the Guanine exchange factor βPIX and results in increased activity of the Cofilin, which is an actin-depolymerizing factor Shank3 sustains ERK-MAPK 30696942 and PI3K signaling. Shank3 also interacts with Rich2, a Guanine activating factor (GAP) of the RhoA GTPase. The disruption of this complex inhibited the insertion of GluA1 in the synaptic membrane of the enlarging dendritic spines necessary for sustaining LTP. The Shank3 over-expression enhances Rac1 activation and induces de translocation of the WAVE complex from the PSD. Finally, Shank3 mutation ASD-related impairs also the mGlur-dependent LTD (Lee et al., 2019), highlighting the critical role of Shank members in regulating the plasticity events occurring in the dendritic spine.

THE P140CAP FAMILY IN THE SYNAPSE

p140Cap is an adaptor protein of about 140 kDa, encoded by the *Srcin1* gene (Salemme et al., 2021). p140Cap is a negative regulator of the Src kinase through the interaction with the C-terminal Src kinase (Csk) (Di Stefano et al., 2007), with a reduction ~~of~~in the proliferative and invasive features of cancer cells. p140Cap is widely expressed in brain tissues of mice and humans, which is implicated in dendritic spines maturation and stability (Jaworski et al., 2009; Repetto et al., 2014). p140Cap in dendritic spines acts as a regulator of the actin branching and microtubules-mediated actin polymerization throughout the interaction of microtubule's (MT) capping protein EB3 (Jaworski et al., 2009). The EB3 depletion in primary hippocampal neurons causes a reduction of mushroom dendritic spines and a significant reduction of F-actin in the dendritic spines' heads.

p140Cap plays a ~~central~~significant role in regulating dendritic spines morphology, thanks to the binding and the direct regulation of p140Cap on Cortactin (cortical actin-binding protein). Cortactin is a protein that acts on the actin filaments inducing their branching and their stabilization; notably, Cortactin is a substrate for Src kinases (Ammer and Weed, 2008). Cortactin is necessary for spine maturation (Hering and Sheng, 2003). It was demonstrated that Cortactin binds F-actin and WAVE and promotes the actin branching through the recruitment of Arp2/3 complex (Weaver et al., 2003). Moreover, the interaction between WAVE and Cortactin is negatively regulated by Src activity (Martinez-Quiles et al., 2004)). As p140Cap inhibits Src kinase activity, the impairment of spine morphology caused by EB3 knockdown is explained by up-regulation of Src kinase activity and inhibition of Cortactin function (Jaworski et al., 2009).

Electrophysiological measurements showed that *p140Cap*$^{-/-}$ mice display defective long-term potentiation (LTP) and reduced long-term depression (LTD), two forms of synaptic plasticity necessary for learning and memory. In addition, behavioral tests on *p140Cap*$^{-/-}$ mice also demonstrated impairment in object recognition, suggesting defects in memory consolidation and learning, in accord with the

electrophysiological data; also, the Rotarod test was performed and, *p140Cap*$^{-/-}$ mice showed a deficit in motor memory (Repetto et al., 2014).

Recently our group demonstrated that p140Cap is a crucial scaffold molecule of the PSD compartment and is able to interact with about 370 proteins. KEGG analysis of these interactions revealed that p140Cap is involved in three main pathways that comprehend Synaptic transmission, Cell-cell interaction, and Axon Guidance. Moreover, we found that p140Cap interactions involved several proteins associated with neurodevelopmental diseases such as ASD and SCZ (Alfieri et al., 2017).

THE KIAA1217/SKT GENE AND PROTEIN

The Skt gene has been identified as a critical regulator of the normal development of intervertebral disks (Semba et al., 2006). Indeed, Skt(Gt) mice, established through large-scale gene-trap mutagenesis, exhibit progressive, postnatal onset abnormality of the intervertebral disks (Karasugi et al., 2009; Semba et al., 2006). However, despite this role in skeletal development, the role of SKT in the synaptic compartment is entirely unknown. Genome-Wide Association Studies for working memory abilities identified KIAA1217, the human homologue of SKT (from now called hSKT) as the best single gene hit for the Digit Span Backward test (Cirulli et al., 2010; Knowles et al., 2014). Only recently, patients carrying a mutation in the hSKT gene were described: the main clinical features are severe skeletal abnormalities with vertebral malformations. Moreover, the patient manifested Intellectual Disabilities and other brain-related diseases (Al Dhaheri et al., 2020).

Interestingly, the hSKT protein presents 60% homology with p140Cap, with a 37% identity, allowing clustering of these proteins as members of the same family. Sequence analysis allows identifying one putative actin-binding domain in the amino-terminal region, followed by a short proline-rich region and an extensive coiled-coil domain extending to the carboxyl-terminal part that may serve for protein-protein interactions (Suda et al., 2011).

AIMS

The primary aim of this work is to investigate the role of the SKT protein in the CNS. To achieve this goal, we have analyzed the protein expression in different tissue and brain regions, generated and characterized knock-out (*Skt*$^{-/-}$) mice, and investigated the impact of SKT depletion on morphological and functional synaptic properties. Moreover, we have also characterized the behavioral and electrophysiological features of *Skt*$^{-/-}$ mice. Overall, we show that, within the PSD, SKT may interact with p140Cap, PSD-95, and Shank3, and that its ablation can influence dendritic spine morphology in primary neuron hippocampal culture and can affect synaptic activity and mice behavior.

MATERIALS AND METHODS

MOUSE STRAINS AND ANIMAL PROCEDURES

All animals were maintained according to institutional animal welfare guidelines and legislation, approved by the local Animal Ethics Committee and the Ministry of Health. Mixed 129Sv × C57BL/6J *Skt* heterozygous mice were generated by inserting Neo-cassette and disrupting the ORF at the level of Exon 7. The animals were maintained in a C57/BL6 genetic background. Overall, the mice were normal, could feed and mate at regular rates, and did not show evident neurological or motor impairments. For the collection of embryos, heterozygous adult (P60) males and females were mated overnight, and the following day the females were examined for the presence of a vaginal plug. The day of the plug was considered day 0.5 of embryonic development (E0.5). Embryos were obtained by Caesarean section from anesthetized pregnant dams. Extra-embryonic tissues were used for genotyping by PCR. Male, 3-month-old wild-type (WT) and *Skt* knockout ($Skt^{-/-}$) littermates were used for synaptosomes preparations. Animals were sacrificed by cervical dislocation. For in vivo dendritic spines analysis $Skt^{-/-}$ females were bred with $Thy1::GFP^{+/-}$ male. The $Skt^{+/-;Thy1::GFP+/-}$ were inbreed to obtain the $Skt^{+/+;Thy1::GFP+/-}$ and $Skt^{-/-;Thy1::GFP+/-}$ that were used for the experiment.

All experiments were approved and performed in accordance with the Italian law (authorization D.M. n°279/95B 27/11/1995) and dispositions of "D.L. n°116, 27/1/1992 concerning animal use and protection in scientific research".

ALCIAN BLUE/ALIZARIN RED STAINING

One-month-old mice WT and $Skt^{-/-}$ were sacrificed, the skin and adipose tissue were accurately removed, mice were eviscerated, processed, and stained with alcian blue and alizarin red, according to the protocols previously described by (Ovchinnikov, 2009). Briefly, the specimens were fixed in 95% ethanol overnight at room temperature (RT), then acetone treatment overnight at RT. Staining with Alcian blue was performed overnight at RT. The following day the entire mouse should turn blue. Destaining was achieved through two washes with 70% ethanol and then 95% ethanol overnight. The following day, ethanol was replaced with 1% KOH solution for 1h, and

the solution was replaced with Alizarin Red Solution for 3-4h at RT. The mice were immersed in 2% KOH for one week. Finally the KOH solution was gradually substituted with Glycerol (100:0 - 80:20 - 60:40 - 40:60 - 20:80 - 0:100; 1h per step). Samples were maintained in 100% Glycerol. Images were acquired using Leica MZ12.5 stereomicroscope equipped with Leica IC80HD cam.

MOUSE PERFUSION AND STAINING

For the preparation of P60 $Skt^{+/+;Thy1::GFP+/-}$ and $Skt^{-/-;Thy1::GFP+/-}$ brains, mice were deeply anesthetized with an intraperitoneal injection of a mixture of Telazol (Zoletil: 80 mg/kg, Alcyon) and Xylazine (Nerfasin 2%: 10 mg/kg, Alcyon), transcardially perfused with 20 ml of PBS and then with 30 ml of 4% (w/v) PFA in PBS. After perfusion, brains were dissected and kept in the same fixative solution overnight at 4°C. Brains were sliced into coronary sections of 120 µm using a vibratome and moved in PBS for free-floating immunostaining; following a blocking step in a PBS solution containing 0.05% Triton X-100 and 10% normal donkey serum (NDS), sections were incubated overnight at 4°C with the GFP(Ck) primary antibodies diluted in PBS with 0.05% Triton X-100 and 3% NDS. Next, sections were washed in PBS (3 × 10 min) and incubated for 1h at RT with the fluorescent secondary antibodies anti-Chicken Alexa488 at 1/1000 dilution and finally mounted on glass slides.

PRIMARY CULTURES OF EMBRYONIC NEURONS

Primary cultures were established either from the hippocampus primordium at E18.5. First, heads were dissected in sterile conditions in Hank's Balanced Salt Solution (GIBCO® HBSS Invitrogen ThermoFisher Scientific) with Ca^{2+}, Mg^{2+} and completed with 1mM HEPES and 1% Pen/Strep. Next, hippocampi were dissected, deprived of the meninges, and dissociated in complete HBSS. At first, mechanical shearing was used, then 1X trypsin, 0,05% EDTA was added for 15 min at 37 °C, followed by three washing cycles in HBSS for 10 min at 37°C. Finally, the last mechanical dissociation was performed by tipping (30 times with the 1000 uL Tip, 30 times with the 200 uL tip). The cell number was determined by Countess (Life Technologies). Next, 1,2× 10^5 cells from each pool were plated on glass coverslips pre-coated with poly-L-lysine (1 mg/ml; Sigma), then washed three times with water and filled with Plating

Media (MEM, 1% Pen/Strep, Sodium Pyruvate(Thermofisher), Glucose(Sigma), 10% Heat Inactivated Donor Horse Serum), and allowed to adhere. Next, the medium was replaced with Neurobasal Complete Medium (Neurobasal (Thermofisher) supplemented with 1% Pen/Strep, 1% GlutaMAX (Thermofisher), 2, 1% B-27(Thermofisher). Neurons were incubated for 18 days at 37 °C in a humidified 5% CO_2 atmosphere.

NEURON TRANSFECTION

At 14 DIV, neurons were transfected with 1 µg of DNA expression vector, using Lipofectamine LTX with Plus Reagent (Thermofisher). Alternatively, neurons were Magnetofected using Neuromag (OzBioscience): 2 µg of DNA was added in 200 µL, then added to 4 µL of Neuromag magnetic beads, briefly vortexed, and incubated RT 15 min. Finally, the solution was added to the neuron, and the cell culture plate was placed on the magnetic plate for 15 minutes.

ELECTRICAL RECORDING FROM PRIMARY CULTURES

WT and *Skt*$^{-/-}$ hippocampi (E18.5) were enzymatically dissociated and plated at a density of 1200 cells/mm2 on poly-L-lysine/laminin-coated MEA devices and maintained for up to 18DIV in the neurobasal medium supplemented with 1% Pen/Strep, 1% Glutamine, 2.5% FBD, 2% B-27 neurobasal, in a humidified 5% CO_2 atmosphere at 37°C. One-third of the culture medium was changed once a week. Multisite extracellular recordings were carried out starting at 7 DIV and up to 18 DIV, using the MEA-MultiChannel System (MCS, Reutlingen Germany). Data acquisition was controlled through the MC_Rack software (MultiChannel System, Reutlingen, Germany), setting the threshold for spike detection at -15 µV and sampling at 10 kHz. Each recording lasted for 90 seconds. After spike sorting, burst analysis was performed using the Neuroexplorer software (Nex Technologies, Littleton, MA, USA). A burst is defined as a group of spikes with decreasing amplitude (Bean, 2007). Thus, we set a threshold of at least three spikes and a minimum of 10 ms duration. In addition, we set interval algorithm specifications such as maximum interval to start burst (0.17 sec) and maximum interval to end burst (0.3 sec) recorded in 0.02 s bins. Burst analysis was carried out by measuring the mean frequency and number of bursts. Cross-

correlation probability vs. time diagrams was constructed using the Neuroexplorer software, using ±0.5s and ±3.5s and 5 ms bin size to evaluate synchronicity. Data are expressed as means ±S.E.M., and statistical significance was calculated with the Student's unpaired T-test (Welch's t-test).

BEHAVIORAL TESTS

WT and *Skt*$^{-/-}$ males, between 120-150 days, were used for behavior, learning, and memory tests. The animals were housed in a standard home cage with food and water ad libitum and an inverted light/dark cycle (lights on at 8:00 pm). Statistical analyses were done with ANOVA, paired t-Student or unpaired t-Student (Welch t-test).

COGNITIVE SKILL AND FLEXIBILITY, PUZZLE BOX

For the Puzzle Box (Ben Abdallah et al., 2011), the "light-dark box" apparatus was used. The mouse initially placed in the illuminated compartment will have to solve tasks to pass into the dark chamber (target zone), covered by a thin layer of sawdust clean and will contain cage material (sawdust, paper, and food). The two compartments were separated by barriers of different nature (described below), making it possible to enter the target compartment. The difficulty of moving to the target will gradually increase with the progress of the trials. The box was placed on a table so that it was possible to observe the mouse without direct visual contact. The mouse was placed in the illuminated compartment at the beginning of each trial, with the muzzle facing the wall opposite the target zone. The trial duration lasted 4 minutes, and the intervals between one trial and another will be 1 minute. At the end of each trial, the mouse will be placed in the dark target compartment for 20 seconds and then put back into its cage. If the animal could not solve the test alone, the barriers were removed, and the experimenter assisted the mouse in entering the dark compartment. The apparatus was cleaned with paper and water in the interval between two trials, and sawdust was changed entirely after five mice.

The following protocol was executed: Day 1: setting Trial 1: Moving to the target zone consists of a simple opening. The mouse had 4 minutes to pass into the protected area. Trials 2 and 3: The "full barrier" was used, so the two compartments were entirely separated by a wall and were given 3 minutes for the mouse to enter the target zone through a subway. Day 2: Burrowing Trial 4: The last trial of the previous day

(underpass) was repeated. Trials 5 and 6: We used the complete barrier, and the underpass was blocked with sawdust, giving 3 min to the mouse to dig out the sawdust and reach the target zone. Day 3: Stop Catch Trial 7: The last trial of the previous day (under scrubbed under scrub) was repeated. Trials 8 and 9: The complete barrier was used, and the underpass was locked with a 2.8g cardboard, with a maximum duration of 4 min. Day 4: Stop Catch Trial 10. The last trial of the previous day was repeated (cardboard plug in the underpass). The behavioral performance was evaluated as the ability to resolve the test and reach the target compartment (success) or not solve it (failure). Data were expressed as means ± S.E.M., and statistical significance was calculated with the Student's unpaired T-test and ANOVA for repeated measurements.

SPATIAL MEMORY, BARNES TEST, FAST VERSION (ATTAR ET AL., 2013)

The Barnes apparatus consisted of a circular plastic platform (140 cm diameter) placed on a pedestal raised 90 cm from the ground. At a distance of about 2 cm from the deck edges, there are 36 holes of 5 cm in diameter, of which 39 are free and one in communication with a darkened and comfortable box that constitutes the escape box or escapes. The test, much like the Morris test, is to give the animal a stress stimulus and motivate it to remember that achieving the escape route coincides with the cessation of the stimulus itself. In this case, stress is composed of deck-oriented solid illumination and an annoying, high-volume sound that is activated and stuck through a PC.

The test consists of the first stage of acclimatization, where the animal is placed in the center of the platform contained within a transparent glass container, which is removed at the same time as the tone is introduced after 30 seconds. At this point, the mouse has two minutes to explore the platform and find the dark box. If this does not happen, the mouse is gently driven and pushed inside the box, which coincides with the sound off, and is left to rest for two minutes. After the first day of acclimatization, the mice were subject to a learning phase in which they were placed every 15 minutes four times at the center of the platform within a cylindrical container. After about 10 sec the container was removed, and the sound activated. In the next two minutes, the animal was left free to explore the platform in search of the access hole for the dark box. Eventual entry into the box coincides with the sound off and with about a 1' rest. This exercise was repeated four times a day for three days (day 2 to day 4) and the target

time. At the end of each trial, the platform and box were cleaned with 70% ethanol and water to eliminate possible olfactory traces. For the same reason, the platform was rotated 90 degrees every three trials. On day 6, the mouse was subjected to the memory test, which consists of the same test but was removed by the experimenter in the absence of the rescue room. Recorded footage was used to evaluate the time elapsed in each platform quadrant using the Ethovision (Noldus) software. Data were expressed as means ± S.E.M. The statistical significance was calculated with the Student's unpaired T-test and two-way ANOVA for repeated measurements.

TISSUE AND CELLS LYSATE PREPARATION

Mouse tissues were obtained by surgical removal and immediately frozen in liquid nitrogen. Next, the tissues were pounded and homogenized with Turax (5 strokes of 30 sec) in ice-cold lysis buffer (150 mM NaCl, 50 mM Tris pH=7,5, 5% Glycerol, 1% NP-40, 1mM $MgCl_2$, 1X Roche protease inhibitors). Finally, cell membranes were pelleted by centrifugation (4°C, 16000g, 45 min).

Cell lysates were obtained by washing cells were washed two times in 1X PBS, then added Lysis buffer (150 mM NaCl, 50 mM Tris pH=7,5, 5% Glycerol, 1% NP-40, 1mM $MgCl_2$, 1X Roche protease inhibitors) and put in gentle shaking (4°C, 10 min). Next, cells were scraped and collected in a centrifuge tube. After 10 minutes, cell membranes were pelleted by centrifugation at 4°C, 17000g, 10 min). Finally, the supernatant was collected, and protein concentration was determined using the Bio-Rad protein assay method (Biorad, Hercules, CA, US.

CRUDE SYNAPTOSOMES AND POST-SYNAPSE PREPARATION

Synaptosomes were prepared from the telencephalon. The tissue was homogenized with a Dounce glass homogenizer and glass pestle in 8 ml ice-cold synaptosome buffer (4mM Hepes pH=7.3, 320mM sucrose, 1mM EGTA, 1X Roche protease inhibitors). The homogenate was centrifuged at 1000g for 10 min at 4°C. After discarding the nuclear pellet, the supernatant was centrifuged at 12500g for 20 min at 4°C. The pellet containing the synaptosomal fraction was resuspended in the synaptosome buffer and further centrifuged at 12500g for 20 min at 4°C obtaining the Crude Synaptosome Fraction. To get the Post-Synapse Membrane purification, the crude synaptosomes

were resuspended in H_2O, 4mM HEPES, and gently mixed at 4°C for 30 min. Then the solution was centrifuged at 25000g for 30 min to isolate the post-synaptic pellet from the presynaptic vesicles. The final pellet was resuspended in 2 ml of ice-cold lysis buffer (150 mM NaCl, 50 mM Tris pH=7,5, 5% Glycerol, 1% NP-40, 1mM $MgCl_2$, 1X Roche protease inhibitors) and immediately processed for immunoprecipitation.

WESTERN BLOT

Western blots were performed with Mini-PROTEAN® TGX™ Precast Gels from Bio-Rad (California 94547 USA).gradient 4–15% Gels were transferred on Nitrocellulose blotting membrane (GE Healthcare Life Sciences) using Towbin buffer (25 mM Tris, 192 mM Glycine, 20% Methanol). Membranes were blocked with Tris-buffered saline TBS (50 mM Tris pH 7, 150 mM NaCl) with 5% Milk for 1 h at room temperature, incubated with primary and secondary antibodies as indicated below, and then developed with Bio-Rad's Clarity ECL on ChemiDoc Touch Imaging System (Biorad). For the western blot of crude synaptosomal proteins, 30µg of proteins were used.

ANTIBODIES

Specific rabbit polyclonal antibody (pAb) against SKT was homemade produced at the Molecular Biotechnology Center (MBC), University of Torino. The antibodies used are as follows: Dlg4 (Mab, Abcam, 1:1000), panShank (rabbit polyclonal, Synaptic System, 1:1000), rabbit polyclonal CamKII (Cell Signaling, 1:1000), Homer-1 (rabbit polyclonal, Thermo Scientific, 1:1000), GluN1 (Mab, Thermo Scientific, 1:1000), Citron-N (rabbit polyclonal, 1:500, Camera et al, 2013), Homer1a (rabbit polyclonal, Thermofisher, 1:1000), Cdkl5 (rabbit polyclonal, Thermofisher, 1:1000), CDC42 (rabbit polyclonal, Cell signaling, 1:1000), β-Catenin(mAb Cell signaling, 1:1000), Axin (Cell Signaling, 1:1000) GAPDH (mAb, SCBT, 1:1000), Actin (mAb, Thermofisher, 1:1000), Tubulin (1:8000, T5168, Sigma-Aldrich), Myc monoclonal antibody 9E10 (American Type Culture Collection), Tiam1 (1:1000, C-16, Santa Cruz Biotechnologies, Palo Alto, CA, USA), Srcin1/p140Cap (clone 2A8, homemade produced at Molecular Biotechnology center, university of Torino, 1:500). Mouse and

rabbit IgGs were purchased from Santa Cruz Biotechnology. Secondary antibodies anti-mouse and anti-rabbit were purchased from Sigma Aldrich. Secondary antibodies for WB were anti-Mouse (Sigma, 1:10000) and anti-Rabbit (Sigma 1:10000). Secondary antibodies for immunofluorescence were Alexa-405, Alexa-488, Alexa-568, and Alexa-647 (Thermofisher, 1:1000).

IMMUNOPRECIPITATION

7µL of Dynabeads protein G (30mg Dynabeads®/mL Invitrogen, Carlsbad, CA, USA) were initially washed using Phosphate Saline Buffer (PBS) 1X 0.05% Tween and incubated with 1µg of selected antibody diluted in the same buffer for 10 min at RT under gentle rotation. Antibody-coupled Dynabeads were then washed twice with PBS 1X 0.05% Tween and then incubated with 1mg of crude synaptosomes or total cell extract for 2 h at 4°C under gentle rotation. Beads were washed five times with cold Lysis Buffer (150 mM NaCl, 50 mM Tris pH = 7, 5% Glycerol, 1% NP-40, 1mM $MgCl_2$, 1X Roche protease inhibitors), then resuspended in 2% SDS-PAGE sample buffer (Laemmli 2X) in reducing conditions and incubated at 95°C for 10 min.

IMMUNOFLUORESCENCE

Neurons at 17DIV cells were gently washed with PBS, fixed for 20 min with 4% PFA, and washed in PBS. Coverslips with adhering neurons were laid on slides, mounted with Mowiol. Fluorescence images were acquired using a combined optical video-confocal microscope (ViCo, Nikon). Images were digitally captured using a 16-bit camera (Nikon) with Nikon NIS-Elements software. For colocalization, neurons were acquired using Leica SP8 confocal system with HyVolution 2 (Leica Microsystems) 4 excitation laser lines (405 Diode, Argon, DPSS561, HeNe633). Fixed cells were imaged using an HCX PL APO 63×/1.4 NA oil immersion objective. Series of x-y-z images were collected.

PLASMID CONSTRUCTS

KIAA1217 (hSKT) cDNA were purchased from RZPD, ID:IRAVp698B0149D6 (alias DKFZP761L0424, GenBank accession n° AL833280.1). First, the cDNA was cloned in the pSPORT1 vector and then cloned in the pBlueScript SK(+) cut with KpnI-SalI to remove the STOP codon and DNA amplification. hSKT was cloned into pcDNA3.1

Myc-His (-) A in frame with the Myc-His tag using the restriction enzymes kpnI and HindIII. Then hSKT was cloned into the pEGFP-C1 vector and pmRFP C1 in frame with GFP and RFP, respectively, using the restriction enzyme XhoI and HindIII.
The cDNA fragments for human kiaa1217 brain cDNA obtained by a combination of molecular cloning and PCR amplification to add unique restriction enzime site with adjust the frame for the GFP (pEGFP-C2 vector) and Myc-Hys tag (pcDNA 3.1 myc-His(-)C. The following primers were used:
hSKT/1/Xho-Fw:ccgctcgagcaccatggaagaaaatgaaagccag;
hSKT/187/KpnI-Rev:gccggtacctgagaacccccagagatctttcttt;
hSKT/184/XhoI-Fw:ccgctcgagtaccatggctctgggggttctctatctcc;
hSKT/321/XhoI-Fw:ccactcgagtaccatggcacattccatgccccctcc;
hSKT/640/KpnI-Rev:ggggtaccttgaggtgcccacaggtggaggctg;
hSKT/641/XhoI-Fw:ccgctcgagaaccatggtagccatccacatgagc;
hSKT/823/KpnI-Rev:ggggtacccatcagtgacatgtctccgcag;
hSKT/824/Kpn-XhoI-Fw:ggggtacctcgagaaccatggggctcctgaaaggcacg;
hSKT/1943/HindIII-Rev:cccaagctttagaggtttcttttgctgt.
hSyn::hSKT/KIAA1217-GFP was generated by combining gene synthesis and molecular cloning approach. hSYN::Cherry was purchased from Addgene (pAAV-hSyn-mCherry, #114472). hSyn promoter was amplified with the following primers:
hSYN-AseI-Fw:ctgattaatcacgcgtgtgtctagactgcagaggg;
hSYN-NheIAgeI-Rev:tttaccggtgctagcggatccggtaccttc.
hSYN, pEGFP-C2, and pEGFP-C2-FLhSKT were cut with AseI and NheI to remove CMVpromoter and CMV enhancer and replace them with hSYN promoter. MCS-BirA(R118G)-HA and pcDNA3.1 mycBioID (R118G) plasmids were a gift from Professor Thilo Kähne (Otto-Von-Guericke, University of Magdeburg). To generate the Myc-BirA-(hSKT construct, we used pcDNA3.1 mycBioID (R118G) plasmid (BirA* located at the N-terminal end of hSKT); we combined gene synthesis and molecular cloning approach. N-terminal hSKT PCR-fragment (aa:2-187) was generate with the following primers:
hSKT/2/XhoI-Fw: ccgctcgagggctctgaagaaaatgaaagccag;
hSKT/187/KpnI-Rev:gccggtacctgagaacccccagagatctttcttt.
XhoI and BglII restriction enzymes were used to cut hSKTaa(2-187); BglII and

HindIII were used to cut the cDNA hSKT sequence; mycBioID(R118G) was cut with XhoI and HindIII to generate the final construct myc-BirA-hSKT.

To generate the hSKT-BirA-HA constructs, we used MCS-BirA(R118G)-HA plasmid (BirA* located at the C-terminal end of hSKT), and we combined gene synthesis and molecular cloning approach. C-terminal hSKT PCR-fragment (aa:1707-1943) was generate with the following primers:

hSKT/1707/BglI-Fw:acatagcccaagaggcctctccccga;

SKT/1943/EcoRI-Rev:cgcgaattcaagcttagaaccagaggtttcttttgctgt.

BglII and EcoRI restriction enzymes were used to cut hSKTaa(2-187); NheI and BglI were used to cut cDNA SKT sequence; MCS-BirA(R118G)-HA was cut with NheI and EcoRI to generate the final construct hSKT-BirA-HA.

Rat GFP-(myc)-PSD-95 was a generous gift from Dr. Matteoli (CNR, University of Milano); mouse HA-Shank1 and mouse HA-Shank3 were kindly gifted by Prof. Giustetto and Prof. Sala (Neuroscience Department, University of Torino and CNR, Univerity of Milan, respectively). pCI-EGFP-GluN1 was purchased from Addgene (plasmid # 45446) pCI EGFP-GluN2A was obtained from Addgene (plasmid #45445), pEGFP-GluN2B (Addgene #45447), pCMV2-PSD95-Flag (plasmid #15463). We generate PSD-95 specific sub-domains by gene synthesis and molecular cloning approach using pCMV2-PSD95-flag as a template. PSD95-N-term(aa 1-53) was generate with the following primers:

PSD95/1/BamHI/NTerm Fw:ggatcctcatggactgtctctgata;

PSD95/53/HindIII/NTerm Rev:aagctttcactcatactccatctcccc;

PSD95-PDZ123(aa 1-394) was generate with the following primers: PSD95/1/BamHI/NTerm Fw:ggatcctcatggactgtctctgata;

PSD95/394/HindIII/PDZ3 Rev:aagctttcatttatactgagcgatgatcgtgac

PSD95-SH3GKEnd(aa 430-724) was generated by the following primers: PSD95/430/XbaI/SH3 Fw:ggatcctcaaccccaagaggggcttctac,

PSD95-End/724/HindIII Rev:aagctttcagagtctctctcgggctgggac. The amplified DNA was first inserted in the pGEM-T Easy vector (Promega, cat #A1360), then amplified. Next, the inserts were cut with a specific restriction enzyme (BamHI and HindIII were used for pEGFP-C2-N-term and pEGFP-C2-PDZ123; XbaI and HindIII were used for pEGFP-C2-SH3GKEnd). Finally, DNA fragments were inserted in the peGFP-C2

vector cut with an appropriate couple of restriction enzymes.

TOP-F10 Escherichia Coli bacteria were heat-shock transformed (42°C, 90 sec, on ice 120 sec with the plasmids described above. For working DNA preparation, bacteria were grown overnight at 37°C in Lysogeny broth 200mL added with the proper antibiotic. The following day DNA preparation was obtained using PureLink™ HiPure Plasmid Maxiprep Kit (Thermofisher, cat #K210006) and quantified by Nanodrop2000 (Thermofisher, cat #ND-2000).

HEK293T CELL TRANSFECTION

HEK293T cells were transiently transfected by calcium phosphate precipitation (Kingston et al., 2003). Briefly, cell density was 50-80% confluent on the day of transfection. Next, 15 µg of DNAs were mixed with sterilized Milli-Q water and 50 µL of $CaCl_2$ 2,5M to a final volume of 500 µL. Twenty-four hours after transfection, the medium was gently removed, and prewarmed fresh medium was added to the plates. The following day, the cells were harvested, and proteins were extracted.

BIOID ASSAY

HEK293T cells were cultured in DMEM 4,5mg/mL Glucose (Thermofisher: 11965084) supplemented with 10% FBS and 1% Pen/Strep. Cells were transiently transfected by calcium phosphate precipitation, as described above. The culture medium was changed one day after transfection (Kumar et al., 2019). Two days after transfection, cells were treated for 3 h with D-biotin 50 µM (Thermofisher, cat #B20656) diluted in the culture medium. Cells were incubated twice with a biotin-free medium for 1 h, lysed with 500 µl Buffer2 (NaCl 150mM; TRIS-HCl pH 7,5 20mM; EDTA 5mM; Deoxycholate sodium 12mM), scraped and incubated for 15 min at 4°C. Lysed cells were collected, cropped with a 26G injection needle, sonicated 4 strokes for 15 sec 30% amplitude, and centrifuged at 4°C, 15000g for 15 min. Supernatants were collected and quantified. 500 µg of extracts were incubated overnight with 10 µL of streptavidin-conjugated resin (PierceTM Streptavidin Agarose; cat #20353). The day after, resins were centrifuged at 4°C, 2500 g, 2 min. Five stepped washes of 1 ml were performed alternating resuspension and centrifugation: one wash in Buffer1 (SDS 2%); two washes in Buffer2 (NaCl 150mM; TRIS-HCl pH 7,5 20mM; EDTA

5mM; Deoxycholate sodium 12mM); one wash in Buffer3 (NaCl 150mM; TRIS-HCl pH 7,5 20mM; EDTA 5mM; Deoxycholate sodium 12mM; NP40 1%; SDS 0,01%; Triton X-100 1%); one wash in Buffer4 (NaCl 150mM; TRIS-HCl pH 7,5 20 mM; EDTA 5 mM; Deoxycholate sodium 12mM; NP40 1%; SDS 0,01%). After the last washing, the resin was dried with a Hamilton needle. Biotinylated proteins were detached from the resin by adding a volume of reduced Sample Buffer (4% SDS) with an excess of D-biotin (1mM) and heating them at 95°C for 15 min. Finally, eluted proteins were collected with a Hamilton needle (Chapelle et al., 2020).

PHYTON ALGORITHM

```
import pandas as pdimport matplotlib.pyplot as plt

astro = input('Inserisci il nome del file: ')

while astro != 'no':

file = pd.read_csv(astro, names=['lenght', 'boh'])

"""

fig, ax = plt.subplots()

ax.scatter(proteins['lenght'])

ax.set_title('proteomics & co-expression')

ax.set_xlabel('Co-expression')

ax.set_ylabel('Fold-change')

"""

dispari = []

pari = []

rapporto = []

a = file.to_dict()

names2 = a['lenght']

#collo

i = 0
```

```
while i <= len(names2.keys()) - 2:
dispari.append(names2[i])
i = i + 2
#testa
l = 1
while l <= len(names2.keys()) - 1:
pari.append(names2[l])
l = l + 2
Mushroom = 0
m = 0
while m <= len(pari) - 2:
if pari[m] > 0.5 and dispari[m] > 0.25:
Mushroom = Mushroom + 1
m = m + 1
else:
m = m + 1
Stubby = 0
s = 0
while s <= len(pari) - 2:
if pari[s] > 0.5 and dispari[s] < 0.25:
Stubby = Stubby + 1
s = s + 1
else:
s = s + 1
Filipodia = 0
f = 0
```

```
while f <= len(pari) - 1:
if pari[f] < 0.2 and dispari[f] > 0.2:
Filipodia = Filipodia + 1
f = f + 1
else:
f = f + 1
Thin = 0
t = 0
while t <= len(pari) - 2:
if 0.2 < pari[t] < 0.5 and dispari[t] > 0.2:
Thin = Thin + 1
t = t + 1
else:
t = t + 1
fine = len(names2) - 1
dendrite = names2[fine]
densità = (fine/2)/dendrite
print('--------------------------------')
print('')
print('Name:', astro)
print('')
print('')
print('Mushroom spines:', Mushroom)
print('')
print('Thin spines:', Thin)
print('')
```

```
print('Stubby spines:', Stubby)
print('')
print('Filopodia:', Filipodia)
print('')
print('Spines density:', densità, 'spines/um')
print('')
print('')
print('--------------------------------')
print(Mushroom)
print('')
print(Thin)
print('')
print(Stubby)
print('')
print(Filipodia)
print('')
print(densità)
print('')
print('')
print('--------------------------------')
astro = input('Vuoi inserire un nuovo file?: ')
print('--------------------------------')
print('')
print('')
print('OK! CIAO!')
print('')
```

print('')

print('------------------------------')

SYNAPTIC INTERACTOME BY MASS SPECTROMETRY

PREPARATION AND IN-GEL DIGESTION OF PROTEINS

As described above, proteins were prepared from WT and *Skt*$^{-/-}$ synaptosomes. After SKT immunoprecipitation, eluted were stacked on the top of a 4–12% NuPAGE gel (Invitrogen) and stained with R-250 Coomassie blue. Gel bands were manually excised and cut into pieces before being washed six times with 25 mM NH_4HCO_3 for 15 min, followed by six washes in 25 mM $NH_4HCO_3$3 containing 50% (v/v) acetonitrile. Gel pieces were then dehydrated with 100% acetonitrile and incubated with 10mM DTTm, 25mM NH_4HCO_3 for 45' at 53°C and with 55mM iodoacetamide, 25mM NH_4HCO_3 for 35, in the dark. Alkylation was stopped by adding 10mM DTT in 25 mM NH_4HCO_3 (10 min). Gel pieces were then rewashed by incubation in 25mM NH_4HCO_3 3followed by dehydration with 100% acetonitrile. Modified trypsin (Promega, sequencing grade) in 25 mM $NH_4HCO_3$3 was added to the dehydrated gel pieces before overnight incubation at 37°C. Peptides were extracted from gel pieces in three sequential extraction steps (each 15') using 30 µl of 50% acetonitrile, 30 µl of 5% formic acid, and 30µl of 100% acetonitrile. The pooled supernatants were dried in vacuo.

NANO-LC-MS/MS ANALYSES

The dried extracted peptides were resuspended in 5% acetonitrile and 0.1% trifluoroacetic acid and analyzed by online nanoLC-MS/MS (UltiMate 3000 RSLCnano, Q-Exactive Plus, Thermo Scientific) with 2 replicates per sample. Peptides were sampled on a 300µm x 5mm PepMap C18 precolumn and separated on a 75 µm × 250 mm C18 column (PepMap, Dionex). The nanoLC method consisted of a 120 min gradient at a flow rate of 300 nL/min flow rate, ranging from 5 to 37% acetonitrile in 0.1% formic acid for 114 min, before reaching 72% acetonitrile in 0.1% formic acid for the last 6 min. Spray voltage was set at 1.6 kV; heated capillary was adjusted to 270°C. Survey full-scan MS spectra (m/z = 400–1,600) were acquired with a resolution of 70,000 after accumulation of 106 ions (maximum filling time 200 ms).

The ten most intense ions were fragmented by higher-energy collisional dissociation after the accumulation of 105 ions (maximum filling time 50 ms). MS and MS/MS data were acquired using the software Xcalibur (Thermo Scientific).

DATA ANALYSES

RAW files were processed using MaxQuant, version 1.5.1.2 (Cox and Mann, 2008). Spectra were searched against the Uniprot database (Mus musculus taxonomy, March 2015 version) and the frequently observed contaminants database embedded in MaxQuant. The I = L option was activated. Trypsin was chosen as the enzyme, and two missed cleavages were allowed. Peptide modifications allowed during the search were: carbamidomethylation (C, fixed), acetyl (Protein N-term, variable), and oxidation (M, variable). The minimum number of unique peptides was set to 1. The matching between runs option was activated.

STATISTICAL ANALYSES

The following steps were mainly performed using the Perseus toolbox (version 1.5.1.6) available in the MaxQuant environment. First, proteins identified in the reverse and contaminant databases were identified with less than two razors + unique peptides or exhibited less than six iBAQ values in one condition (3 biological replicates with two analytical replicates each for control and *Skt*$^{-/-}$ co-IPs) were discarded from the list. iBAQ values of the 1952 remaining proteins. After log2 transformation, iBAQ values were normalized by condition-wise centering, missing data imputation was realized (replacing missing values by a constant weak value calculated independently for each injected sample as the 2.5-percentile value of the column), and statistical testing of differential abundances between control and Skt conditions were conducted using Welch t-testing. Considering a protein as a potential binding partner of SKT must have passed our significance criteria: FDR threshold of 1% on p-values using the Benjamini-Hochberg method and a minimum 2-times enrichment in WT samples compared to the *Skt*$^{-/-}$ controls.

BIOINFORMATIC ANALYSES OF MS DATA

The over-representation of annotation terms (disease, function, etc.) was estimated by use of the hypergeometric distribution to test whether the number of selected proteins is larger than would be expected by chance;

$$p = 1 - \sum_{i=0}^{k-1} \frac{\binom{M}{i}\binom{N-M}{n-i}}{\binom{N}{n}}$$

where N is the total number of proteins in the background distribution, M is the number of genes within the distribution that are annotated to the node of interest, n is the size of the list of genes of interest, and k is the number of genes within the list, which are annotated to the node. Obtained p-values were adjusted for multiple testing by Bonferroni correction at 0.05 or 0.01 significance levels.

A list of 6,688 proteins was selected for literature comparison as a synaptic universe based on combined results from 35 published synapse proteome studies. Protein lists from those studies were curated, mapped to stable IDs (Entrez, Uniprot, MGI) for humans and mice, and combined into a single list containing unique protein/gene names, IDs, and publication sources. Enrichment analysis of annotation in the interactome was performed in R, specifically using the Bioconductor package ClusterProfiler for Gene Ontology (GO) and KEGG enrichment analysis (Yu et al., 2012) and Bioconductor ReactomePA package for pathway over-representation analysis (http://bioconductor.org/packages/release/bioc/html/ReactomePA.html). For each enrichment type (GO, KEGG, Reactome), two background sets of proteins were used: (1) the default mouse genome list from Bioconductor and (2) our list of 6688 published synaptic proteins to reveal the consistency in enriched terms.

A PSD network was constructed from a list of 1,443 proteins obtained from a study of the PSD in the human brain (Bayes et al., 2011). Mining publicly available databases obtained Protein-protein interactions: HIPPIE (Schafer et al., 2012), BioGRID (Chatr-Aryamontri et al., 2015), IntAct (Kerrien et al., 2012), and performing an InterologWalk over different species using Bio::Homology::InterologWalk (Gallone et al., 2011). The connected PSD network consists of 1,312 proteins and 8,031 protein interactions. This PSD network was clustered, making use of the spectral properties of the network; the network was expressed in terms of its eigenvectors and eigenvalues and partitioned recursively (using a fine-tuning step) into communities based on maximizing the Modularity clustering measure (Luo et al., 2007; Simpson et al., 2010). Where first, we found the node that gave the maximum change in Modularity when moved from one community to the other, provided the maximum change in Modularity. This node's community was then fixed, and we repeated the process until all nodes had been moved. The process was repeated from this new state until the

change in the Modularity between the new and old state was less than the predefined tolerance. The Modularity of the full PSD network was found to be 0.36.

The robustness of the full PSD network communities was assessed by running the algorithm 500 times, randomly selecting 80% of the network node-set and related interactions each time. The package clusterCons (21129181) was used to build a consensus matrix to test the robustness of the communities and proteins found inside the communities. Community and protein robustness values range from 0, indicating no confidence in existing, to 1, indicating absolute confidence in the existing cluster. Community robustness values range from 0,1 to 0,7, and from 0,01 to 0,9 for protein robustness. Clusters C4(p=0,0004), C11(p=0,0015), C56(p=0,0034), C62(p=0,005), C68(p=0,00096) showed evidence of being robust.

ANALYSIS OF DENDRITIC SPINE AND FLUORESCENCE CO-LOCALIZATION

Fiji ImageJ software was used to analyze spine density, morphology, and fluorescence colocalization. ImageLab (BioRAD) was used for WB analysis of band intensity. Fluorescence images were acquired using an optical combined video-confocal microscope (ViCo, Nikon). Images were digitally captured using a 16-bit camera (Nikon) with Nikon NIS-Elements software. Fluorescent images for Thy1::GFP Brain Slices were acquired using Leica SP8 confocal system with HyVolution 2 (Leica Microsystems) 4 excitation laser lines (405 Diode, Argon, DPSS561, HeNe633). Fixed cells were imaged using an HCX PL APO 63×/1.4 NA oil immersion objective. Series of x-y-z images were collected.

STATISTICAL ANALYSIS

All statistical analysis was performed with Prism GraphPad (v.9.0.1). The “n” represents the number of biological replicates for each experiment, as indicated in each figure legend. To compare one variable, the two-tailed paired Student’s t-test was performed. All bar graphs are represented as means ± standard error of the mean (SEM). Two-ways ANOVA with Bonferroni correction was used for repeated measurements Significance is expressed as follows: * p-value<0.05, ** p-value <0.01, *** p-value <0.001,**** p-value <0.0001, ns: not significant.

RESULTS

SKT is highly expressed in the brain and is mainly confined in the postsynaptic compartments

To address the physiological role of the SKT protein in the brain, we first analyzed its expression in different mouse tissues by western blotting (WB) with a specific homemade polyclonal antibody. We found that SKT is highly expressed in the brain and testis, where, in SDS-PAGE, we observed a doublet with an apparent MW of 170 kDa. In contrast, it is almost undetectable in organs like the kidney and spleen and expressed at low levels in the other tissues (Figure 1A). Furthermore, the WB revealed the presence of additional bands at different MW, which reflects the presence of different isoforms, likely the result of an extensive alternative splicing process or the presence of other starting sites (Figure 1A). Furthermore, within the brain, analysis of protein extracts of specific regions revealed that SKT is more expressed in the cortical areas than in other brain regions (Figure 1B). Furthermore, the protein is present in the synaptic p140Cap interactome (Alfieri et al., 2017), raising the hypothesis of its possible functions in the synaptic compartment. Indeed, WB analysis of crude synaptosome preparation showed that SKT is exclusively confined in the postsynaptic fractions prepared from adult mouse brains, according to PSD-95, a canonical PSD marker (Figure 1C). These data show a tight association of SKT to dendritic spines and suggest a role of SKT in the PSD architecture. Finally, the analysis of the temporal expression of SKT in the whole mouse brain or primary cortical neurons revealed that SKT is already expressed in the early phases of brain development, with a discrete expression since P7 and a peak between P10 and P14 (Figure 1D). These data suggest a role for SKT in spinogenesis and dendritic spines development.

Generation of the *Skt*$^{-/-}$ mouse model.

To evaluate the SKT role *in vivo*, we generated a total SKT knock-out mouse (*Skt*$^{-/-}$) by disrupting the *Skt* gene by inserting a neomycin cassette within exon 7. The ablation of the SKT protein was verified by WB analysis of total brain extracts from wild type (WT) and *Skt*$^{-/-}$ mice (Figure 2A, Figure B). In homozygous mice, the insertion abolished SKT expression (Figure 2C). *Skt*$^{-/-}$ mice were born with a Mendelian ratio. They did not display grossly phenotypic alterations, except for the presence of the spinal dysmorphism already shown in (Semba et al., 2006) with the involvement of the intervertebral disks, which causes the characteristic phenotype of the "sickle tail" (Figure 2D). The mice were vital and survived like the WT controls. The primary defect observed was the sub-fertility of *Skt*$^{-/-}$ male, which was constantly present in the colonies and could be ascribed to a yet unknown role of the protein in the testis (Karasugi et al., 2009)

Skt$^{-/-}$ mice show abnormal behavior features.

To assess whether the absence of SKT in the synaptic compartment could affect behavior in *Skt*$^{-/-}$ mice, we performed a broad spectrum of behavioral tests, including i) the Open Field Test to analyze the anxiety behavior ii) the Puzzle Box Test that allows exploring the capacity of the solving task, hence the cognitive behavior, iii) the Barnes Maze to investigate the long term spatial memory, and iv) the Burrowing Test to observe the arousing normal mice behavior. While no statistically significant results were obtained from spontaneous and anxiety behavior (data not shown), we obtained promising results in the Puzzle Box Test, which measures executive behavior, involving mice's ability to solve increasingly complex tasks and remember how to settle them. Briefly, mice's movement from a bright arena to a dark arena (a place considered safer for the mice) is made day by day more difficult (solve the "puzzle"), thus increasing the time taken by the animals to reach the dark area (Ben Abdallah et al., 2011). The time taken to cross the tunnel that connects the two different environments is valued (Figure 3A). In this test, *Skt*$^{-/-}$ mice showed significative worse performance than the WT mice (point sum: 23.17±2.78 WT, 27.59±1.57 *Skt*$^{-/-}$, (t)student p-value=0,0189; n=9 WT, n=9 *Skt*$^{-/-}$) (Figure 3B), with *Skt*$^{-/-}$ mice remarkably incapable of solving the more complex tasks with a statistically difference compared to the WT controls ($F_{(1-9)}$= 4.96; Two-Ways ANOVA for Repeated measures with Bonferroni correction, p-value=0,04) and compared to trials ($F_{(9-72)}$ = 24,83; Two-Ways ANOVA for Repeated measures with Bonferroni correction p-value<0,0001. (Figure 3C). These results suggest that *Skt*$^{-/-}$ mice have a functional deficit that involves executive functions. Since the Puzzle box allow the investigation of specific brain areas' dysfunction depending on mice behavior during the different tasks (Ben Abdallah et al., 2011), we analyzed the Kaplan-Meyer survival analysis for trail 3-6-9 (Short Term Memory, hippocampal function) and compared trial 4-7-10 (Long Term Memory, cortical function) to reveal impairment of specific brain regions. We found that there is a significant difference in trials 9 (Figure 3D) and trials 10 (Figure 3E) related to habituation and learning (T_9 p-value=0,0285; T_{10} p-value=0,0123; n=9 WT, n=9 *Skt*$^{-/-}$), suggesting involvement of SKT mainly in the cortex than in other brain regions.

To test spatial memory, we performed the Barnes Maze Test (Attar et al., 2013), where

mice should escape from a brightly light, exposed, circular open platform surface to a small dark recessed chamber located under one of the 36 holes around the perimeter of the platform. The test consists of 15 trials (3 the first day and 4 per day the following days) where the time required to enter the box is evaluated. At the end of the learning phase (the first four days), the animals rested for one day, thus, in the following days, the mice have placed again in the arena, but the box was removed from the old position. This phase (Probe trial) lasts one minute. The time the mouse spends in the quadrant in which the box was present in the learning phase is measured as a parameter that is a direct measure of long-term spatial memory. On the sixth and seventh days, the box is moved to the opposite position to measure the ability of the mouse to find a new solution (reversal phase). Both *Skt*$^{-/-}$ and WT mice similarly learned the test without statistically significant differences ($Day_{(1-4)}$ p-value<0.001, Day_4 WT 24,47±4,12 vs *Skt*$^{-/-}$ 26,18±4,14 p-value=0.275) (Figure 3F). During the Probe trial (Memory), the two-way ANOVA for repeated measurements revealed a statistically significant difference in the percentage of time spent in the different quadrants; in particular, the *Skt*$^{-/-}$ mice spent significantly more time in target zones than the WT mice (39.75±5.4 % time WT, 60.54±10.45 % time *Skt*$^{-/-}$, n=9 WT, n=9 *Skt*$^{-/-}$) (Figure 3G), suggesting a possible inflexibility behavior. However, the reversal phase was similar in the two genotypes.

Skt$^{-/-}$ cultures display abnormal spontaneous firing properties and delayed network synchronization during neuronal maturation.

To investigate whether the decreased activity in *Skt*$^{-/-}$ mice brain could affect altered spontaneous firing properties during neuronal maturation, we compared the electrical properties of WT and *Skt*$^{-/-}$ hippocampal networks using Micro-Electrode Arrays (MEAs). Spontaneous firing of hippocampal neurons was monitored at different developmental stages (from 7 days in vitro (DIV) up to 21 DIV) to assess the network's maturation. As shown previously (Gavello et al., 2012), the firing properties of hippocampal neurons vary significantly over time in these conditions. Spontaneous activity has been mainly characterized by an asynchronous spike train activity with a limited number of bursts in immature cultures that switches to a burst activity characterized by a higher degree of synchronization in mature cultures.

The MEA analysis revealed that neurons from *Skt*$^{-/-}$ cultures significantly reduce burst number, frequency, and duration (Figure 4A). In mature cultures (18DIV) there are significant difference between *Skt*$^{-/-}$ and WT firing properties, with decreased mean frequency (0.57±0.04 Hz *Skt*$^{-/-}$ vs 1.6±0.09Hz WT; p-value<0.0001, Welch's t-test) (Figure 4B), burst number (7.7±0.5 *Skt*$^{-/-}$ vs 9.4±0.3 WT; p-value=0.0016, Welch's t-test) (Figure 4C) and burst duration (0.086±0.003 sec *Skt*$^{-/-}$ vs 0.2±0.006 sec WT; p-value<0.0001, Welch's t-test) (Figure 4D). Moreover, in *Skt*$^{-/-}$ neurons, channels with no burst activity were increased (37% *Skt*$^{-/-}$ vs. 16% WT) (Figure 4E).

We analyzed the raster plot generated by the MEA to compare the network synchronization in WT and *Skt*$^{-/-}$ neurons and, therefore, the ability of cultured neurons to create a coordinate organization between each other. At 18DIV, the *Skt*$^{-/-}$ cultures were less synchronized than the WT controls (Figure 4F). Synchronization was quantified as the probability of coincidence of single events between electrodes, computing cross-correlation histograms between a reference electrode and the remaining ones. The activity within the *Skt*$^{-/-}$ cultures showed a decreased cross-correlation peak compared to WT (Figure 4G), indicating a loss of synchronicity (Figure 4F). Overall, the MEA tracks indicated that at 18DIV, the *Skt*$^{-/-}$ neurons displayed a typical signature of immature cultures. Furthermore, the Raster Plot Analysis at 18DIV cultured neurons revealed a significant delay in neuronal synchronization in *Skt*$^{-/-}$ neurons.

SKT absence causes a decrease in dendritic spines number and altered dendritic spines morphology *in vivo* and *in vitro*.

To further confirming the localization of SKT in the synaptic compartment, we detected the presence of the protein by immunofluorescence. Primary cortical neuron staining for SKT and the main PSD scaffold proteins PSD-95 and Shank revealed that SKT is present in specific neuronal structures, including dendrite and dendritic spines. In this last compartment, SKT co-localizes with both PSD-95 and Shanks, suggesting a particular role of SKT in spinogenesis and dendritic spine organization (Figure 5A and Figure 5B). Therefore, we assessed *in vivo* and *in vitro* whether SKT absence could significantly affect synaptic maturation and morphogenesis.

To study the *in vivo* effects of SKT on dendritic spines, we used a mouse model that expresses the GFP protein under the Thy1 promoter (THYmocyte differentiation antigen 1) (Zheng et al., 2013). These mice have permanently labeled specifically excitatory neurons. In particular, the populations that can be analyzed are the pyramidal neurons of the cortex, the striatum, the CA1 region of the hippocampus, the granular cells of the dentate gyrus, and finally, the interneurons of the striatum and amygdala (Chakravarthy et al., 2008).

We crossed the *Thy1::GFP* transgenic mouse with the $Skt^{-/-}$ mouse to obtain $Skt^{+/+;Thy1::GFP+/-}$ and $Skt^{-/-;Thy1::GFP+/-}$. Mice were deeply perfused, and the brain was rapidly removed. Brain slices (120 µm thickness) were obtained by vibratome. A high-resolution image was taken by confocal microscopy, acquiring 80 um length of the primary dendrites (Figure 5C). To avoid any bias, we draw ROI for each dendritic spine to measure the length of the neck (l) and the width of the head (h).

We wrote a Python Based algorithm for automatically analyzing the density and the shape of the dendritic spines (filopodial >0,2 µm - w<0,2 µm; stubby l <0,2 µm - w<0,2 µm, thin l >0,2 µm - 0,2<w<0,6 µm, mushroom l >0,2 µm - w>0,6 µm) (Figure 5D). We found a significant decrease in dendritic spine density in the $Skt^{-/-}$ mice compared to WT controls (0,6±0.4 spine/µm $Skt^{-/-;Thy1::GFP+/-}$ vs 1,4±0.3 spine/µm $Skt^{+/+;Thy1::GFP+/-}$; p-value<0.001 Student t-test) (Figure 5E), with a reduction in each type of morphology taken in consideration (mushroom 19.2±5.9 $Skt^{+/+;Thy1::GFP+/-}$ vs 10.3±8.1 $Skt^{-/-;Thy1::GFP+/-}$; thin 68.3±22.3 $Skt^{+/+;Thy1::GFP+/-}$ vs 37.6±22.1 $Skt^{-/-;Thy1::GFP+/-}$ -; stubby $Skt^{+/+;Thy1::GFP+/-}$ vs 5.7±2.1 $Skt^{-/-;Thy1::GFP+/-}$; filopodia 22.8±15.4

Skt$^{+/+;Thy1::GFP+/-}$ vs 9.6±7.8) (Figure 5F).

Moreover, to explore the *in vitro* effects of SKT on dendritic spines, we exploited hippocampal neuron primary cultures prepared from WT and *Skt*$^{-/-}$ embryos at E18.5. After 14 DIV, the primary neurons were transfected with a Green Fluorescence Protein (GFP) empty vector to fill the dendritic shaft and the dendritic spines. At 16 DIV, the neurons were fixed and analyzed at confocal microscopy to evaluate GFP-transfected neurons' spine number and morphology (Figure 6A). The spines were counted and classified into filopodia, stubby, and mushroom using the ImageJ software according to the length of the neck and the width of the dendritic spine head (Figure 6B). *Skt*$^{-/-}$ neurons displayed a decrease in overall spine density (0,48±0.02 spine/µm *Skt*$^{-/-}$ vs 0,55±0.02 spine/µm WT; p-value=0.011) (Figure 6C). Furthermore, the analysis of the spine morphology revealed a significant increase of filopodial-like spines (44,98%±1,87 *Skt*$^{-/-}$ vs 23.6%±0,99 WT ; p-value<0.001), and a significant decrease in mushroom-like spines in *Skt*$^{-/-}$ neurons compared to WT neurons (28,19%±1,78 *Skt*$^{-/-}$ vs 51,83%±1,12 WT p-value<0.001) (Figure 6D). Overall, these results showed that the loss of SKT impaired spine number and maturation, with a shift towards a less immature phenotype.

To further investigate the causal role of SKT in the regulation of synapse morphology, we examined the effects of exogenous expression of hSKT in the *Skt*$^{-/-}$ primary neurons. We generated a plasmid with GFP-tagged hSKT under the human Synapsin1 promoter (hSYN1), and we magnetofected this plasmid in *Skt*$^{-/-}$ neurons at DIV14. The neurons were fixed at DIV16 and analyzed at confocal microscopy to count and classify the dendritic spines (Figure 6E). We found that the overexpression of exogenous hSKT partially rescued dendritic spine density (0,31±0.02 spine/µm *Skt*$^{-/-}$ vs 0,36±0.12 spine/µm hSYN1::hSKT-GFP vs 0,57±0.13 spine/µm WT; p-value=0.011, n=21 *Skt*$^{-/-}$, n=35 hSYN1::hSKT-GFP, n=36 WT) (Figure 6F) and significantly restored the mushroom morphology in *Skt*$^{-/-}$ primary neurons, with a concomitant decrease in filopodia spines (mushroom 55,8%±7,8 WT vs 64,9±8,4 hSYN1::hSKT-GFP vs 26,3±10.0 *Skt*$^{-/-}$, p-value<0,001; filopodia 24,0%±7,7 WT vs 22,3±9,8 hSYN1::hSKT-GFP vs 60,9±10.9 *Skt*$^{-/-}$, p-value<0,001)(Figure 6G).

hSKT interacts with the PSD components PSD-95 and Shank3.

Based on the previous data showing that the loss of SKT causes morphological, electrophysiological, and behavioral alterations, we asked whether SKT may interact with known PSD components in the postsynaptic compartment, in particular with MAGUK and Shanks family proteins. Moreover, in previous proteomic papers, SKT has been detected as a PSD protein (Roy et al., 2018). Therefore, we immunoprecipitated SKT from WT synaptosomes and looked for the presence of PSD-95, Shanks, and p140Cap in the immunoprecipitates (IP), with *Skt*$^{-/-}$ synaptosomes as negative controls. We found that SKT immunoprecipitated with PSD-95, Shanks, and p140Cap PSD proteins by WB analysis. Furthermore, the interaction is confirmed by reversal immunoprecipitation (Figure 7A), indicating that these proteins are associated in this compartment. Therefore, to further investigate and better characterize the interactions of SKT with PSD components, we used Human Embryonic Kidney (HEK) 293T cell line, a non-synaptic cell that does not express endogenous hSKT (Figure 7B). Here we performed transfection and co-immunoprecipitation (Co-IP) with a plasmid vector coding for hSKT, alone or combined with plasmids coding for the PSD protein of interest. To this end, we generated two tagged versions of hSKT, either tagged with Green Fluorescence Protein (GFP) or Red Fluorescent Protein (RFP) protein. In addition, HEK293T cells were co-transfected with RFP-hSKT and GFP-PSD-95, GFP-p140Cap, GFP-NR1, GFP-NR2A, GFP-NR2B, Emerald-Homer1a. The co-IP experiments showed that hSKT interacted strongly with PSD-95 and, to a lesser extent, with p140Cap, while it did not interact in this system with the NMDA receptors and with Homer1a (Figure 7C).

To focus on the interaction with PSD-95, we generated mutant constructs to express different GFP-tagged PSD-95 subdomains: PSD-95(1-53), which is the N-Terminal part of PSD-95, PSD-95(1-397), that comprehends the three PDZ domains, and PSD-95(430-724) that include the SH3 and GK domain of PSD-95 and that are necessary for the correct PSD-95 folding (McGee et al., 2001) (Figure 7D). We co-transfected HEK293T with the RFP-hSKT vector and with the GFP-PSD-95 full length or specific subdomains, and we perform Co-IP assays. We found that hSKT interacted strongly with the full-length PSD-95 and, even if to a lesser extent, with the first half of the protein (PSD95 1-397, which comprehends the three PDZ domains), while it did not

interact with the other domains of PSD-95 (Figure 7E).

PDZ domain-containing proteins play a critical role in the organization of the synapse, regulating PSD protein assembly and orchestrating signal transduction (Kim and Sheng, 2004). Since a PDZ domain is present in other synaptic proteins, we tested if hSKT can interact with other PDZ domain-containing proteins, particularly the Shank family proteins Shank1 and Shank3. Thus, to explore this interaction, we co-transfected GFP-hSKT in combination with either Shank1 or Shank3, both tagged with Human influenza hemagglutinin (HA). By immunoprecipitating GFP, we detected Shank proteins by WB using an antibody that recognizes all the Shank family isoforms (anti-pan Shank). The band corresponding to Shank proteins was present only in cells co-transfected with Shank 3 and not with Shank1 (Figure 7F), thus concluding that hSKT interacts with Shank3 and not with Shank1 in this system. Overall, the biochemical analysis indicated that hSKT might interact with PDZ domain-containing proteins, particularly PSD-95 and Shank3, likely through their PDZ domains. Moreover, hSKT can also bind to p140Cap, thus contributing to the assembly and the regulation of the molecular network of scaffold proteins in the post-synapse compartment.

hSKT proximally interacts with PSD-95 and Shank3 in HEK293T transfected cells.

To investigate the proximal interaction between hSKT and the postsynaptic scaffold proteins PSD-95 or Shank3, we applied the BioID assay that allows detection by biotinylation proximal direct interactions in the range of 30nm. We co-transfected HEK293T cells with hSKT-BirA* fusion proteins and Flag-PSD-95 or HA-Shank3 plasmids. We transfected HEK293T cells with BirA*HA or MycBirA* vectors as negative controls. We performed a BioID assay (see Materials and Methods) 24 hours after transfection, and we quantified the biotinylated protein levels by WB, measuring the ratio between the BioID pull-down signal and the related normalized extract. We found that both PSD-95 and SHANK3 were highly biotinylated in the presence of Myc-BirA-hSKT. In contrast, when HEK293T cells were transfected with hSKT-BirA-HA, we observed a low enrichment of PSD-95 (Figure 8A) or Shank3 (Figure 8B) in the BioID pull-down, which was similar to the negative control. This analysis indicates that hSKT can proximally interact with the postsynaptic scaffold proteins PSD-95 and Shank3 in vitro, and the N-terminal of hSKT may be involved in both the proximal interactions.

The N-terminal half of hSKT is responsible for the association with PSD-95 and Shank3.

Given the results obtained in the BioID experiments, we sought to validate the interaction between the N-terminal region of hSKT and Shank3 or PSD-95 through co-immunoprecipitation in HEK293 transfected cells. First, we cloned the N-terminal half, hSKT(1-823), or the C-terminal half, hSKT(824-1943) of hSKT in a pEGFP vector. As a result, highly conserved protein regions of hSKT were identified as conserved putative domains in the two half-hSKT constructs (Figure 8C). Then, we co-transfected HEK293T cells with either HA- Shank3- or PSD-95-flag and each of the half-hSKT GFP vectors. Finally, we immunoprecipitated PSD95 or Shank3, and we found that only hSKT(1-823) and not hSKT(824-1943) co-immunoprecipitates with the postsynaptic scaffold proteins PSD-95 (Figure 8D) and Shank3 (Figure 8E). These results confirmed the BioID experiments and indicated that only the N-half region of SKT participated in the interaction with PSD-95 and Shank3 proteins.

SKT synaptic interactome analysis by Mass Spectrometry.

The synapse is a complex network of thousands of proteins that interact to form an extensive lattice and organize the signaling platform necessary for the proper information transmission (Grant, 2019). The study of synapse networks and how protein-protein interaction alteration could be related to specific pathology remain the main challenge for discovering, classifying, and treating neurobiological disorders. Therefore, we performed quantitative proteomic and interactome analysis to evaluate the complexes in which SKT is involved. We immunoprecipitated SKT from 1mg purified crude synaptosomes from WT and the negative control *Skt*$^{-/-}$ crude synaptosomal preparations. As expected, the IP showed a specific signal of SKT only in the WT and not in the KO synaptosomes (Figure 9A). Moreover, in the S-Ponceau stained nitrocellulose, we detected several bands in the IPs from WT samples but not from *Skt*$^{-/-}$ synaptosomes, indicating that several proteins selectively co-immunoprecipitate with SKT in the WT samples and not in the *Skt*$^{-/-}$ negative control. (Figure 9B).

To identify SKT-binding partners, we applied label-free quantitative MS-based proteomics to the SKT-IPs from WT and *Skt*$^{-/-}$synaptosomes. First, proteins eluted from the IPs were stacked in the SDS-gel, then the gel was isolated, digested with trypsin, and the resulting peptides analyzed by nano liquid chromatography coupled to tandem MS (two analytical replicates per sample). Identities and intensities of the recovered peptides and proteins in each sample were obtained using MaxQuant (Cox and Mann, 2008). After filtering and statistical analysis of iBAQ values (Schwanhausser et al., 2011), 748 (included SKT) proteins enriched in the WT samples than *Skt*$^{-/-}$were identified (Table 1), as represented in the Volcano plot (Figure 9C). We tested several postsynaptic proteins listed in the interactome on the SKT immunoprecipitates to validate the proteomic results. As already shown, we validated SKT interactions with p140Cap (Alfieri et al., 2017). Moreover, we detected co-immunoprecipitation also with GluN1, PSD-95, Shank members, and Homer1a are receptor and core scaffolds members in the PSD; and with CamkIIβ, β-Catenin, CitronN, Cdkl5 that are important functional members in the postsynaptic compartment (Figure 9D). We also verified that four proteins (CDC42, Tiam1, Axin,

and ERK), not included in the interactome, were not immunoprecipitated with anti-SKT antibody (Figure 9E). Thus, these data indicated that the SKT synaptic interactome we isolated contains bona fide SKT-containing protein complexes. Then we analyzed the SKT interacting proteins dataset to evaluate their distribution between presynaptic (2236 proteins dataset) and postsynaptic compartments (5507 proteins dataset). 730 of the 748 SKT interactors overlap with the datasets considered. Of these proteins, the majority were described as specifically postsynaptic (249) or found in both PSD and Presynaptic compartments (481), while none were specifically presynaptic (Figure 9F).

To analyze the functional role of SKT, we investigated the KEGG (Kyoto Encyclopedia of Genes and Genomes) enrichment in biological processes based on the SKT interactome. We found that SKT is enriched in Biological Process terms that include Synaptic Vesicle (Synaptic vesicle endocytosis (p-value=7.37E-07), Vesicle-mediated transport in synapse (p-value=3.76E-06), Cytoskeleton Regulation (Positive regulation of MAP kinase activity (p-value=4.68E-03), and Glutamate Receptor Signaling (Chemical synaptic transmission (p-value=0.035). (Figure 9G) The functional enrichment analysis suggests that the SKT interactors are involved in important processes in the synaptic compartment that regulate cytoskeleton, vesicle cycle, and glutamate receptor signaling pathways.

The Proteomap (Liebermeister et al., 2014) allows visualizing the KEGG pathway derived Gene Ontology (GO) in which proteins obtained from SKT interactome are organized. The representation size of the category is influenced by the abundance of proteins in GO categories. In addition, the Proteomap highlighted the involvement of SKT in processes that regulate cytoskeleton assembly, vesicular transport, signaling, and transducing molecules (Figure 9H). These results indicate that the SKT interactome contains proteins relevant to postsynaptic organization and function.

DISCUSSION

In the present study, we demonstrate for the first time the involvement of the adaptor protein SKT in CNS biology, with a specific focus on the postsynaptic dendritic spine development and maturation. We focus our attention on the SKT protein in the CNS based on our previous studies on the p140Cap adaptor protein. Indeed, we found that SKT and p140Cap are two members of a small family of proteins with a high homology at the aminoacidic level. Moreover, we recently found SKT as a binding partner of p140Cap in the p140Cap interactome analysis from the synaptosome (Alfieri et al., 2017).

SKT is ubiquitously expressed; however, to address the relevance of SKT in CNS, we generated specific antibodies, and we analyzed its expression in different tissues by classical western blotting. Our data highlight that SKT is highly expressed in the brain, particularly in the brain cortex and other brain areas such as the hippocampus, striatum, and cerebellum. These results agree with those found in the Allen Brain Atlas data, where the relative amount of SKT RNA was obtained by in situ hybridizations (http://www.brain-map.org/).

Therefore, to assess its putative role in the CNS, we generated a total knock-out mouse ($Skt^{-/-}$) by disrupting the gene by inserting a neomycin cassette within exon 7. As a result, $Skt^{-/-}$ mice were born in a Mendelian ratio, without macroscopic phenotypic alterations, except for the already described (Semba et al., 2006) kinky tail phenotype (sickle tail), found in mice where the SKT gene has been ablated by random insertion mutagenesis.

Since the CNS controls many aspects of animal behavior, we first evaluated phenotypic functional consequences of deleting the *Skt* gene with different paradigms. Starting from the behavior, remarkably, $Skt^{-/-}$ mice showed significantly worse performances in the Puzzle box, a test exploring executive functions involving both the hippocampus and the prefrontal cortex (Ben Abdallah et al., 2011). The mutant mice were also defective in the Barnes Maze Test, which studies explorative behavior and spatial memory more correlated with hippocampal function. In this test, $Skt^{-/-}$ mice learned as the WT mice how to solve the trial; but they spent more time exploring the target quadrant during the probe test than the control mice. This behavior can be related

to an attitude of cognitive inflexibility, already observed in animal models of schizophrenia (Brigman et al., 2010; Mirnics et al., 2001), where the connections between the circuit system of the hippocampus, cortex, and limbic system are altered. (Benes, 2000). Taken together, these data suggest an impairment in cognitive function, especially in problem-solving. We will plan additional behavioral tests that could further explore the relevance of SKT in memory and the emotional and motivational sphere. Interestingly, Cirulli et al. analyzed common genetic variations in executive function in 1,086 healthy individuals of mixed ethnicity, with additional cognitive tests to explore working memory in 514 individuals. The gene KIAA1217, hSKT, was the best hit for digit-span backward with a high significance (Cirulli et al., 2010; Knowles et al., 2014). At that time, the functional characterization of SKT was still unknown. The present work expands the data discussed in the review of Knowles et al. and sheds light on SKT involvement in working memory, thought to be extremely important for general cognitive ability and psychiatric and neurodegenerative illness.

Other neuronal functional aspects have also been investigated in *Skt*$^{-/-}$ mice. In particular, the primary cultures were also exploited to assess the relevance of SKT in the electrophysiological features measured with the MEA analysis. *Skt*$^{-/-}$ cultures display abnormal spontaneous firing properties and delayed network synchronization during neuronal maturation. These data are consistent with the abnormalities found in the morphological analysis, linking the defect in spine maturation with the delay in neuronal network synchronization (Gavello et al., 2012). Interestingly, the MEA experiments were also performed in the *p140Cap*$^{-/-}$ neurons, with an opposite result since the absence of p140Cap ensures a more effective synchronous activity within the network. Further analysis shows that p140Cap, in addition to its role in the postsynaptic excitatory compartment (Repetto et al., 2014; Tomasoni et al., 2013), plays a fundamental role in the development and refinement of the inhibitory network by regulating both the number and the activity of GABAergic synapses (Russo et al., 2019). Therefore, these results suggest that SKT may play differential roles compared to p140Cap, irrespective of its sequence homology. Future experiments on SKT localization in the excitatory versus inhibitory compartment and electrically-evoked excitatory postsynaptic currents (eEPSCs) will shed light on this crucial aspect.

Dendritic spines can be classified according to their morphology (Matsuzaki et al., 2001; Yuste and Bonhoeffer, 2001), identifying their functional state. First, the dendritic spines emerged as protrusions from the dendritic shaft with filopodial structures. Then, also based on the presynaptic activation state, the dendritic spines can receive the stimuli that lead them to mature (Bourne and Harris, 2007). Thus, they evolved in a mushroom structure, given their typical morphology with a narrow neck and a wide head containing thousands of functional proteins, the most steady dendritic spines. (Holtmaat et al., 2005; Paulin et al., 2016; Trachtenberg et al., 2002).

The neurodevelopmental stage determines dendritic spines' density and shapes, and their alterations in the number or shape typology are crucial in neuropsychiatric disorders like Autism Spectrum Disorders, Schizophrenia, or related diseases. (Penzes et al., 2011; Phillips and Pozzo-Miller, 2015). For those reasons, dendritic spine density and morphology can be considered fundamental parameters for synaptic maturation and function. THY1::GFP transgenic mice are widely used to investigate several neuronal morphological parameters, such as those characterizing dendritic spine plasticity. Moreover, it has already been demonstrated that THY1::GFP neurons can be assumed to represent the entire neuronal cells (Vuksic et al., 2008).

To study how the absence of SKT affected dendritic spines features in vivo, we generated $Skt^{+/+;Thy1::GFP+/-}$ and $Skt^{-/-;Thy1::GFP+/-}$ mice. Density and morphological analysis of the dendritic spines present in the primary dendrite of cortical neurons was deeply analyzed, showing a significant reduction in dendritic spines density in the $Skt^{-/-;Thy1::GFP+/-}$ mice compared to the $Skt^{+/+;Thy1::GFP+/-}$ controls, with a loss in each of the specific subtypes of dendritic spines.

Furthermore, a detailed morphological analysis of dendritic spines from primary hippocampal neuron cultures from the $Skt^{-/-}$ mice shows a defect in dendritic spine number and dendritic spines maturation. Indeed, $Skt^{-/-}$ neurons revealed an increased percentage of immature structures such as filopodia, with a concomitant decrease in the mature form of mushroom dendritic spines. These phenotypic changes are comparable to those we already found in the $p140Cap^{-/-}$ primary neurons (Repetto et al., 2014), even if it is well known that mutations in genes or proteins involved in spine biology frequently confer a similar phenotype (Durand et al., 2012; Grant, 2013; Sala et al., 2015). Notably, introducing exogenous human SKT (hSKT) in $Skt^{-/-}$

primary neurons partially rescues the dendritic spines density and significantly restores the mature mushroom morphology. Overall, from *in vitro* and *in vivo* analysis, our results indicate that the SKT protein is a new functional component of the dendritic spine. Although LTP and LTD analysis from brain slices will be crucial to uncovering whether dendritic spines' morphological alterations can affect activity-dependent remodeling, these data indicate that SKT plays a critical role in dendritic spines dynamics, regulating both spinogenesis and dendritic spines' maturations.

MAGUK adaptor proteins are the most abundant adaptor proteins in the PSD of excitatory synapses, assembled in large and dynamic supramolecular complexes. Between them, PSD-95 is well characterized for generating a complex backbone for protein-protein interactions necessary for mature dendritic spines stabilization (Cane et al., 2014; Sheng and Kim, 2011). Beneath the PSD, the family of Shank proteins links ionotropic glutamate receptors and mGluR1 receptors, thus orchestrating efficient mechanisms to control the actin cytoskeleton that sustain the dendritic spines (Tu et al., 1999; Wang et al., 2016). Understanding how scaffold proteins accurate assembly and how new proteins may play a role in maintaining synapse stabilization is crucial for addressing the genetic mechanisms underneath neuropathological disorders such as ASD (Grove et al., 2019).

Our results indicate that SKT can be ascribed as a new functional component of dendritic spines. Biochemical analysis from synaptosomes reveals the ability of SKT to associate with critical scaffold elements of the excitatory PSD, such as PSD-95 and Shank3. The biochemical analysis in HEK293T allows identifying the PDZ domains of PSD-95, and likely Shank3, as the putative binding site for SKT.

However, traditional biochemical methods such as co-immunoprecipitation return high noise signals due to transient and weak interactions and the different degrees of solubility of specific proteins (Cheah and Yamada, 2017). For this purpose, we decided to study SKT's ability to interact at least with Shank3 or PSD-95, exploiting the recently developed BioID assay (Roux et al., 2018). The fusion protein is made up of BioID, and the protein of interest allows to follow protein-proximity labeling in living cells, which can be isolated and identified by western blot or mass spectrometry (Sears et al., 2019).

We applied a BioID assay to study the interactions between human hSKT and Shank3 or PSD-95 in HEK293T transfected cells. We found that the N-terminal of hSKT is involved in the proximal interaction with both PSD-95 and Shank3. These data highlight the ability of SKT to participate in the PSD network, extending from the proximal membrane domain, where PSD95 is preferentially localized, to the inner part of the dendritic spine together with Shank3 (Alie and Manuel, 2010) in a multimeric complex (Figure 10). As shown in the Figure 10, two SKT molecules may effectively homodimerize to connect the two synaptic regions. However, whether the binding of hSKT to PSD-95 or Shank3 can affect their functional properties remains to be established.

Finally, we also generated an SKT interactome from synaptosomes exploiting immunoprecipitation of specific complexes containing SKT and the mass spectrometry. In this way, we shed new light on which pathways and complexes SKT is involved. For example, we found that not only does SKT interacts with PSD-95 and Shank3, but it is also involved in processes that regulate fundamental neuronal functions such as the cytoskeleton assembly, the vesicle cycle, and the glutamate receptor signaling pathways.

Overall, this work clearly shows that SKT is a postsynaptic protein involved in dendritic spine generation and maturation, possibly through the interaction with the most relevant scaffold proteins in the PSD. Furthermore, the absence of SKT greatly impairs the cognitive abilities of mice and electrophysiological properties *in vitro.* Although additional work is required to explore the electrophysiological relevance of SKT, this work puts the cellular and molecular basis for further investigating the role of this scaffold protein in the synapse as a link between the upper and the inner PSD region in the dendritic spine, and its relevance in signal transduction through the synapse. In addition, these data pave the way for future translation experiments to address the role of SKT alteration in neurological disorders.

FIGURES AND TABLES

Figure 1 - SKT is early and highly expressed in the mouse brain and is enriched in postsynaptic preparations.

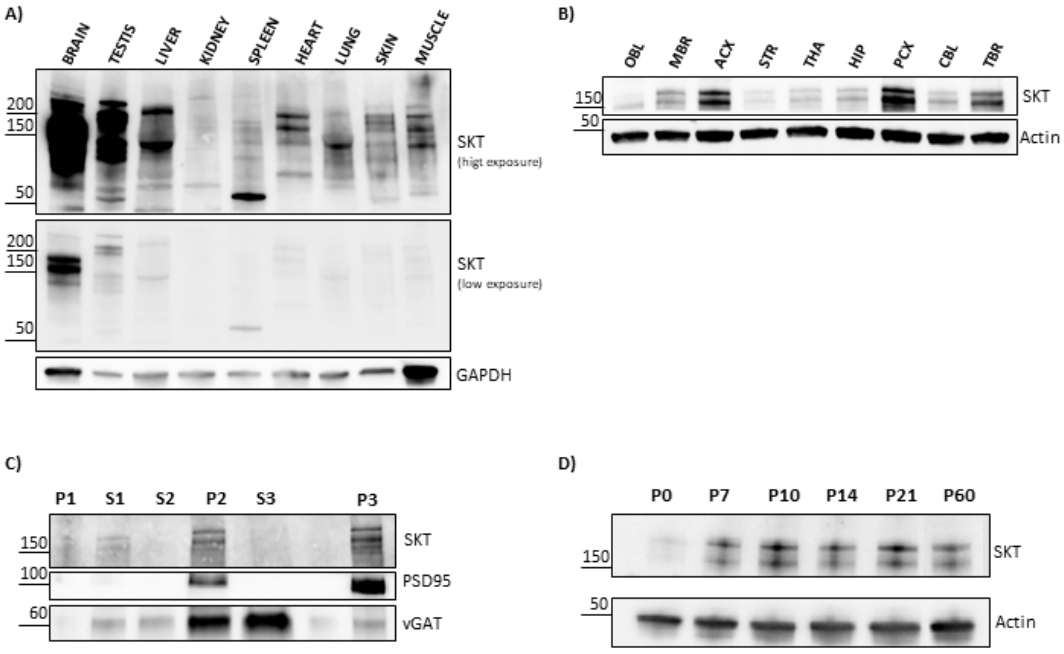

Figure 1 - SKT is early and highly expressed in the mouse brain and is enriched in postsynaptic preparations.

A) SKT is highly expressed in the brain and testis. WT mouse tissue homogenates (50 µg tissue extract per lane) were analyzed by immunoblotting using the homemade SKT antibody. SKT bands were specifically detected in the brain and testis. In the brain, proteins migrated as a doublet just above 150 kDa, while in the testis, a higher isoform is present (about 200 KDa), highlighting the presence of several isoforms of SKT. Several bands are present to a lesser extent in the other tissues. GapdH was used as loading control.

B) SKT is expressed in whole brain regions and is particularly represented in cortical areas. The homogenates of the mouse brain regions (30 µg tissue extract per lane) were analyzed by immunoblotting using the SKT antibody. Proteins migrated as a doublet just above 150 kDa. β-Actin was used as loading control. OBL=Olfactory Bulb; MBR=Midbrain; ACX=Anterior Cortex; STR=Striatum; THA=Thalamus; HIP=Hippocampus; PCX=Posterior Cortex; CBL=Cerebellum;TBR=Total Brain.

C) SKT is enriched in Crude Synaptosome Preparation and is exclusively detected in the PostSynaptic Fractions. WT purified crude synaptosomes and postsynaptic Fractions (30 µg tissue extract per lane) were analyzed by immunoblotting using the SKT antibody. PSD95 was used as a postsynaptic marker, while vGAT was used as a presynaptic marker. P1=nuclear fraction; S1=First cytosolic fraction; S2= synaptosome washing; P2=crude synaptosome, S3=presynaptic vesicles fraction; P3=post-synaptic fraction.

D) Time course expression of SKT in total brain lysates. Western blot analysis of the whole mouse brain extracts at different postnatal days. SKT expression is detected since P7 with an increase at P10 that remains constant over P60.

Figure 2 - Generation of the *Skt*$^{-/-}$ model.

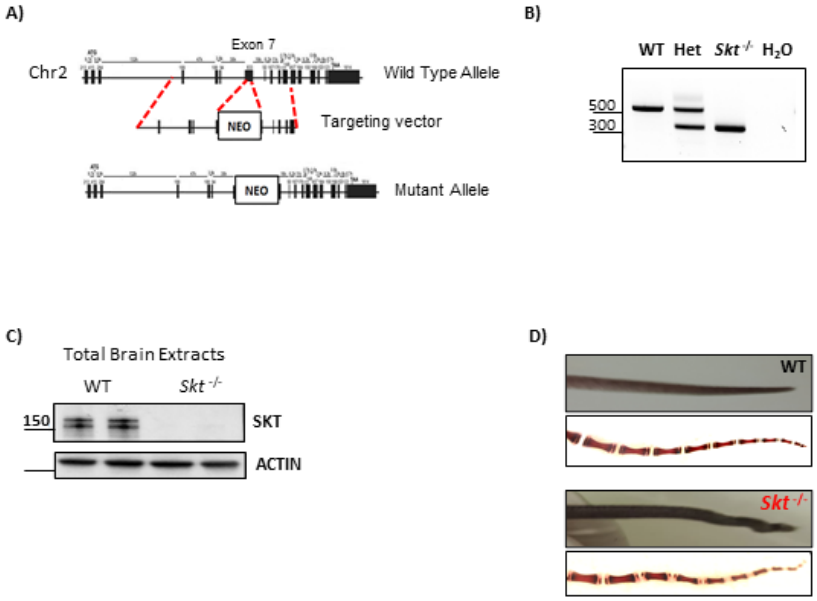

Figure 2 - Generation of the *Skt*$^{-/-}$ model.

A) Schematic representation of mouse recombinant *Skt* construct. The neomycin cassette (NeoR) disruption was targeted into exon 7 of the *Skt* gene on mouse chromosome 2.

B) Representative PCR screening of genomic DNA. DNA was obtained from a biopsy of littermate from heterozygous mice breeding. Water was used as negative control.

C) Ablation of the SKT protein. Western blot detection of SKT protein levels in total brain cell extracts from mice of the indicated genotypes. Actin was used as loading control.

D) The Sickle tail phenotype. The tail phenotype of one-month-old mice. *Skt*$^{-/-}$ mice show kinked tails compared to WT. Alcian-Blue/Alizarin-Red staining showed the presence of intervertebral disk herniation causative of the kinky tail phenotype.

Figure 3 - The *Skt*$^{-/-}$ mice are defective in behavioral tests.

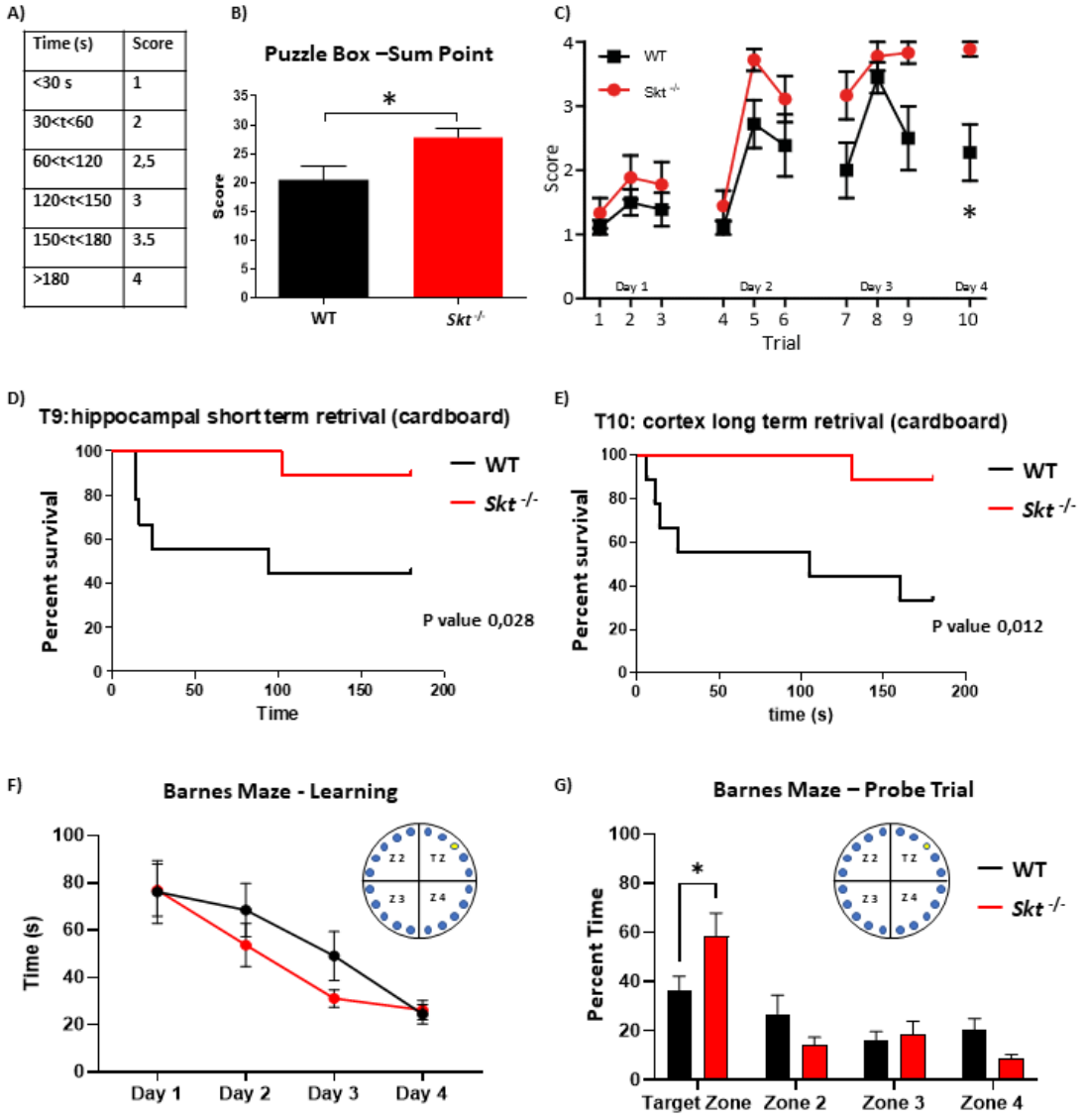

Figure 3 - The *Skt*$^{-/-}$ mice are defective in behavioral tests.

A) Puzzle-Box. In the Puzzle box, the mouse moves from a bright arena to a dark arena connected with an underpass. This tunnel is open at first (trial1-4), then is filled with sawdust that the mouse has to remove (trial5-7). Finally, a cardboard plug replaced the sawdust in the last trials (trial8-10). The time taken to cross the tunnel that connects the two different environments is evaluated with the score shown in A).

B) Puzzle-Box quantification. The graph shows the sum of the scores obtained during the Puzzle-Box test. 23.17±2.78 WT, 27.59±1.57 *Skt*$^{-/-}$, Student (t) Test p-value = 0,0189.

C) *Skt*$^{-/-}$ mice require longer times to reach the goal zone compared to WT littermates. Scores to reach the goal zone during the 9 trials of the test. T_1 WT=1,11±0,12, *Skt*$^{-/-}$=1,36±0,20; T_2 WT=1,61± 0,21, *Skt*$^{-/-}$=2,00±0,30; T_3 WT=1,33±0,25, *Skt*$^{-/-}$=1,73±0,31; T_4 WT=1,22±0,16, *Skt*$^{-/-}$=1,59±0,31; T_5 WT=2,89±0,42, *Skt*$^{-/-}$=3,77±0,15; T_6 WT=2,44±0,53, *Skt*$^{-/-}$=3,18±0,32; T_7 WT=2,17±0,52, *Skt*$^{-/-}$=3,32±0,33; T_8 WT=3,44±0,26, *Skt*$^{-/-}$=3,55±0,33; T_9 WT=2,50±0,53, *Skt*$^{-/-}$=3,59±0,31; T_{10} WT=2,44±0,51, *Skt*$^{-/-}$=3,50±0,31. Differences were wider when the mice have to resolve the most complex task ($F_{(1-9)}$ = 4.96; Two-Ways ANOVA for Repeated measures with Bonferroni correction, p-value=0,04 for genotype correlation. $F_{(9-72)}$=24,83; Two-Ways ANOVA for Repeated measures followed by Bonferroni correction p-value <0,0001 for trials correlation).

D) and E) Kaplan–Meier survival analysis. The behavioral deficit in long-term retrieval in *Skt*$^{-/-}$ mice compared to WT. A mouse is censored when it reaches the goal zone.

F) Learning time in Barnes Maze. Both *Skt*$^{-/-}$ and WT mice revealed a significant time difference in reaching the hole in the various days, which means that all of the animals learned the test in similar ways. ($Day_{(1-4)}$ p-value < 0.001; Day_4 WT 24,47 s ±4,12 vs *Skt*$^{-/-}$ 26,18 s ±4,14 p-value = 0.275 Two-way ANOVA analysis for repeated measurements followed by Turkey post-hoc correction.

G) Probe trial in Barnes Maze. Percentage of time traveled during the probe trial in the four different zones subdivided the arena. There are significant difference in the percentage of time elapsed between the different zones ($F_{(1,3)}$ = 13.75; p-value < 0,001) and respect for the interaction between genotype zones ($F_{(1,3)}$ = 2,83; p = 0,047) with

Skt$^{-/-}$ that spend significantly more WT time in the Target Zone (p-value=0,014 Two-way ANOVA analysis for repeated measurements followed Neumann-Keuls post-hoc test).

In the tests, error bars correspond to ±SEM. * = p-value ≤ 0.05 (n=9 WT and n=9 *Skt*$^{-/-}$)

Figure 4 - *Skt*$^{-/-}$ primary neuron cultures display abnormal electrophysiological properties when tested by MEA.

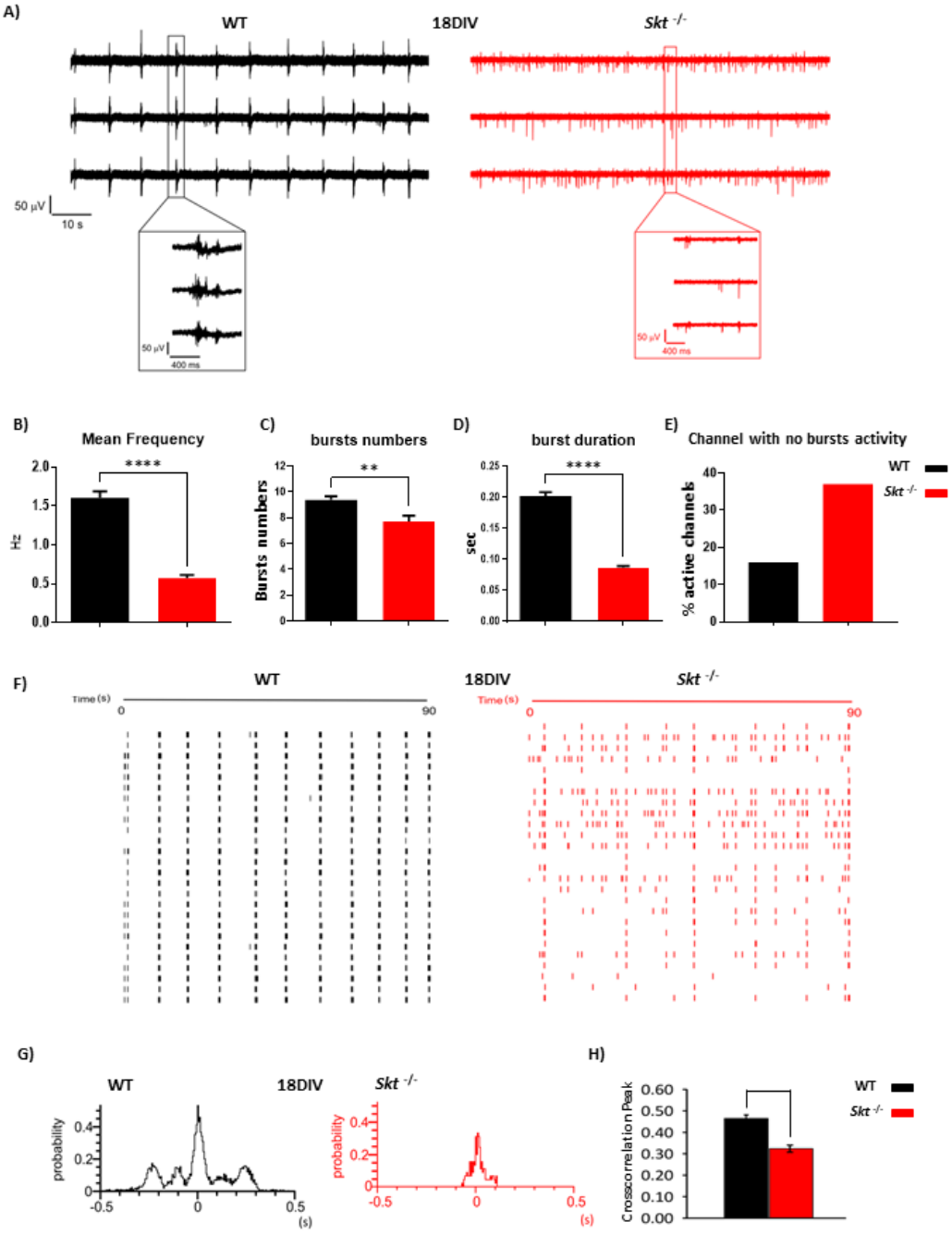

Figure 4 - *Skt*$^{-/-}$ primary neuron cultures display abnormal electrophysiological properties when tested by MEA.

A) Representative recordings (3 channels each) of cultures of late embryonic (E18.5) primary hippocampal neurons. The data were obtained from WT (left) or Skt-/- *Skt*$^{-/-}$ embryos (right), maintained for 18 days in vitro (DIV).

B) Quantification of firing frequency. At 18DIV is significantly lower in *Skt*$^{-/-}$ than in WT controls (1,6±0.09 Hz vs WT0,57±0.04 Hz *Skt*$^{-/-}$; n=383 WT and n=402 *Skt*$^{-/-}$; p-value=0.0016, Welch's t-test)

C) Burst number. At 18DIV is significantly lower in *Skt*$^{-/-}$ than in WT controls (9.4±0.3 WT vs 7.7±0.5 *Skt*$^{-/-}$; n=322 WT and n=254 *Skt*$^{-/-}$; p-value=0.0016, Welch's t-test)

D) Burst duration. At 18DIV is significantly lower in *Skt*$^{-/-}$ than in WT controls (0.2±0.006 sec WT vs 0.086±0.003 sec *Skt*$^{-/-}$; n=322 WT and n=254 *Skt*$^{-/-}$; p-value<0.0001, Welch's t-test)

E) Channel without burst activity. is signicantly higher in *Skt*$^{-/-}$ than WT controls (16% WT vs 37% Skt-/- ; n=383 WT and n=402 *Skt*$^{-/-}$)

F) Representative raster plots of the spontaneous activity of MEA recordings. Data from WT (left) or *Skt*$^{-/-}$ (right), primary hippocampal cultures at 18 DIV.

G) Representative Cross-correlogram plots. The data show the probability of coincidence of the events versus time of WT (black trace) and *Skt*$^{-/-}$ (red trace) primary hippocampal cultures.

H) The mean peak of correlation at 18 DIV. Data from *Skt*$^{-/-}$ neurons compared to WT controls (WT 0,56±0,02 vs *Skt*$^{-/-}$ 0,32±0,03; n=383 WT and n=402 *Skt*$^{-/-}$; p-value<0,001,Welch t-test) .

Error bars correspond to ±SEM. ** = p-value ≤ 0.01; *** = p-value ≤ 0.001; **** = p-value ≤ 0.0001

Figure 5 - *Ex vivo* analysis of dendritic spines.

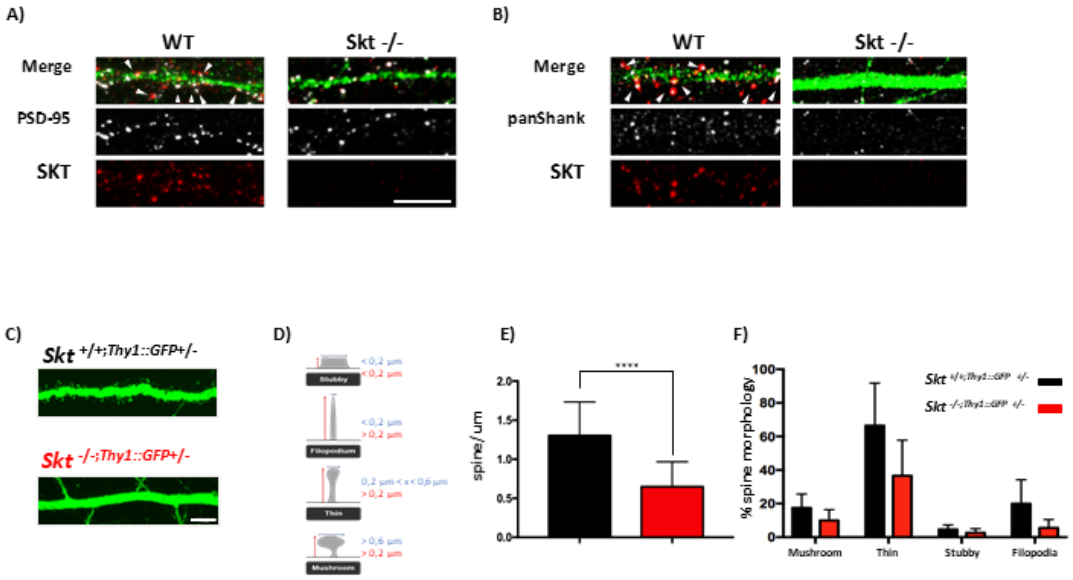

Figure 5 - *Ex vivo* analysis of dendritic spines.

In A) and B), primary neuronal cultures derived from *Skt*$^{-/-}$ or WT embryos from E18.5 littermates were plated at 1,2*10^5 cells per glass coverslip and analyzed by immunofluorescence. In C-F, mice brain slices were obtained from *Skt*$^{+/+;Thy1::GFP+/-}$ and *Skt*$^{-/-;Thy1::GFP+/-}$.

A) PSD95 and SKT colocalization in primary neurons. Confocal microscopy of WT and *Skt*$^{-/-}$ DIV18 primary cortical neurons immunolabeled with dye-labeled antibodies to MAP2 (Alexa-488), SKT (Alexa-568), PSD-95(Alexa-647). Scale bar 10µm. PSD-95 and SKT colocalization are indicated by the arrowheads.

B) Shanks and SKT colocalization in primary neurons. Confocal microscopy of WT and *Skt*$^{-/-}$ DIV18 primary cortical neurons immunolabeled with dye-labeled antibodies to MAP2(Alexa-488), SKT(Alexa-568), panShank(Alexa-647). Scale bar 10µm. Shanks and SKT colocalization is indicated by the arrowhead.

C) Representative confocal images of *Thy1::GFP* fluorescent-labeled dendritic spines protruding from cortical pyramidal neurons in primary dendrites of *Skt*$^{+/+;Thy1::GFP+/-}$ and *Skt*$^{-/-;Thy1::GFP+/-}$ P60 littermates. Dendritic spines of *Skt*$^{+/+;Thy1::GFP+/-}$ and *Skt*$^{-/-;Thy1::GFP+/-}$ were counted and classified according to the Python algorithm process of ROI measurement of dendritic spines' neck length and head width (n=5 mice for each genotype). For each mouse, 20 slides were taken; at least 8 neurons were analyzed for each slide. A segment of 80µm of primary dendrite was considered for the analysis.

D) Representative draw of the shape of the dendritic spines: filopodia l >0,2 µm - w<0,2 µm; stubby l <0,2 µm - w<0,2 µm, thin l >0,2 µm - 0,2<w<0,6 µm, mushroom l >0,2 µm - w>0,6 µm.

E) Quantitative analysis of the frequency distribution of dendritic spine density: 1,4±0.3 spine/µm *Skt*$^{+/+;Thy1::GFP+/-}$ vs 0,6±0.4 spine/µm *Skt*$^{-/-;Thy1::GFP+/-}$; p-value < 0.001 Student t-test)

F) Quantitative analysis of the frequency distribution of the dendritic spine morphology. The analysis shows an overall decrease in all the dendritic spines' types (mushroom 19.2±5.9 *Skt*$^{+/+;Thy1::GFP+/-}$ vs 10.3±8.1 *Skt*$^{-/-;Thy1::GFP+/-}$; thin 68.3±22.3 *Skt*$^{+/+;Thy1::GFP+/-}$ vs 37.6±22.1 *Skt*$^{-/-;Thy1::GFP+/-}$; stubby 8.2±2.2 *Skt*$^{+/+;Thy1::GFP+/-}$ vs

5.7±2.1 *Skt*$^{-/-;Thy1::GFP+/-}$; filopodia 22.8±15.4 *Skt*$^{+/+;Thy1::GFP+/-}$ vs 9.6±7.8 *Skt*$^{-/-;Thy1::GFP+/-}$).

Error bars correspond to ±SD. **** = p-value ≤ 0.0001

Figure 6 - *In vitro* Analysis of dendritic spines in primary neuronal cultures.

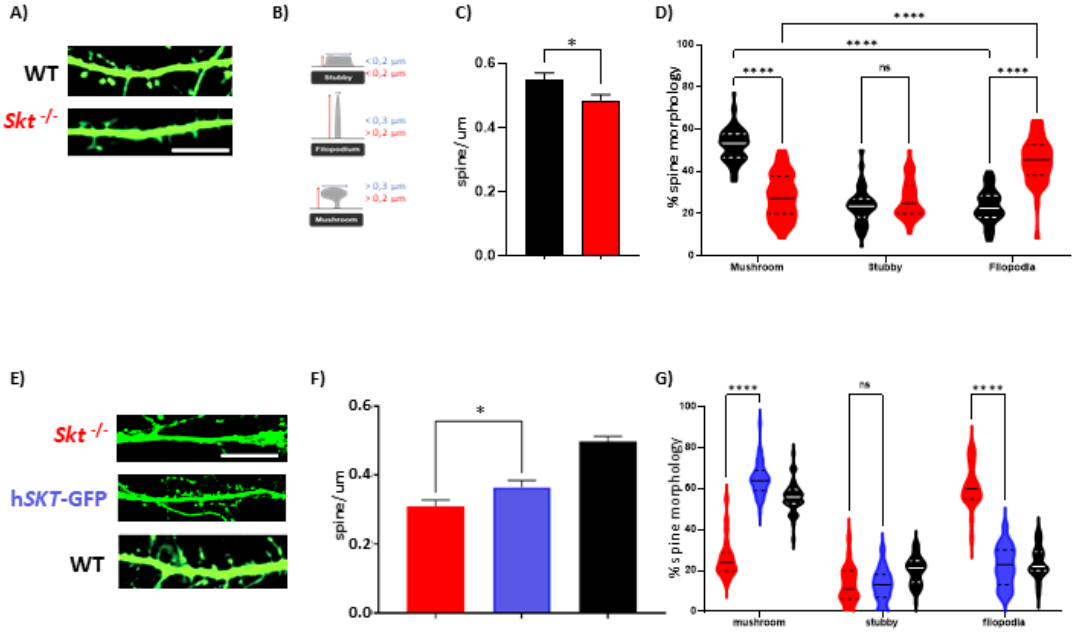

Figure 6 - *In vitro* Analysis of dendritic spines in primary neuronal cultures.
Primary neuronal cultures derived from *Skt*$^{-/-}$ or WT embryos from E18.5 littermates were plated at 1,2*10^5 cells per glass coverslip and transfected with pEGFP, or GFP-hSKT. Dendritic spines were counted and classified according to the Python algorithm process of ROI measurement of dendritic spines' neck length and head width. At least 2 segments per neuron (n) were counted.

A) Representative confocal images of dendritic spines. pEGFP transfected primary cortical neurons of Skt-/- and WT embryos. The lipofectamine transfection was performed at DIV14, and the primary neurons were fixed at DIV16. Scale bar 10µm.

B) Representative draw of the shape of the dendritic spines. filopodia l >0,2 µm - w<0,3 µm; stubby l <0,2 µm - w<0,2 µm, mushroom l >0,2 µm - w>0,3 µm.

C) Quantitative analysis of the frequency distribution of dendritic spine density: 0,48±0.02 spine/µm *Skt*$^{-/-}$.vs 0,55±0.02 spine/µm WT; p=0.011; Welch t-test; n=64 WT, n=37 *Skt*$^{-/-}$.

D) Alteration in spine morphology. We observed a significant increase in filopodia spines (44,98%±1,87 *Skt*$^{-/-}$ vs 23.6%±0,99 WT ; p-value<0.001, Two-ways ANOVA for repeated measures with Bonferroni correction), and a significant decrease in mushroom-like spines in *Skt*$^{-/-}$ neurons compared to WT neurons (28,19%±1,78 *Skt*$^{-/-}$ vs 51,83%±1,12 WT p-value<0.001, Two-ways ANOVA for repeated measures with Bonferroni correction).

E) Representative confocal images of dendritic spines in primary hippocampal neurons obtained from E18.5 *Skt*$^{-/-}$ and WT littermates in rescue experiments. The *Skt*$^{-/-}$ cultures were transfected with hSYN1::SKT-GFP or hSYN1::GFP, and the WT culture was transfected with hSYN1::GFP. The magnetofection was performed at DIV14, and the primary neurons were fixed at DIV16. Scale bar 10µm.

F) Quantitative analysis of the frequency distribution of dendritic spine density upon rescue experiments. hSYN1::hSKT-GFP vector transfected in *Skt*$^{-/-}$ neurons significantly rescues the dendritic spines density over the *Skt*$^{-/-}$ control (0,31±0.02 spine/µm *Skt*$^{-/-}$ vs 0,36±0.12 spine/µm hSYN1::hSKT-GFP vs 0,57±0.13 spine/µm WT; p-value$_{(Skt\text{-}/\text{-};hSYN::hSKT\text{-}GFP)}$ = 0.011; Welch t-test; n=21 *Skt*$^{-/-}$, n=35 hSYN1::hSKT-GFP, n=36WT)

G) Quantitative analysis of the frequency distribution of dendritic spine mushroom morphology upon rescue experiments. hSYN1::hSKT-GFP vector transfected in *Skt*$^{-/-}$ neurons significantly restores the dendritic spines mushroom morphology with a concomitant loss in filopodial dendritic spines. (mushroom 55,8%±7,8 WT vs 64,9±8,4 hSYN1::gSKT-GFP vs 26,3±10.0 *Skt*$^{-/-}$, p-value < 0,001; filopodia 24,0%±7,7 WT vs 22,3±9,8 hSYN1::gSKT-GFP vs 60,9±10.9 *Skt*$^{-/-}$, p-value < 0,001, Two-ways ANOVA for repeated measures with Bonferroni correction).

Error bars correspond to ±SEM. *= p-value ≤ 0.05; ***= p-value ≤ 0.001; **** = p-value ≤ 0.0001

Figure 7 - SKT interacts with the adaptor proteins PSD-95, Shank3 and p140Cap.

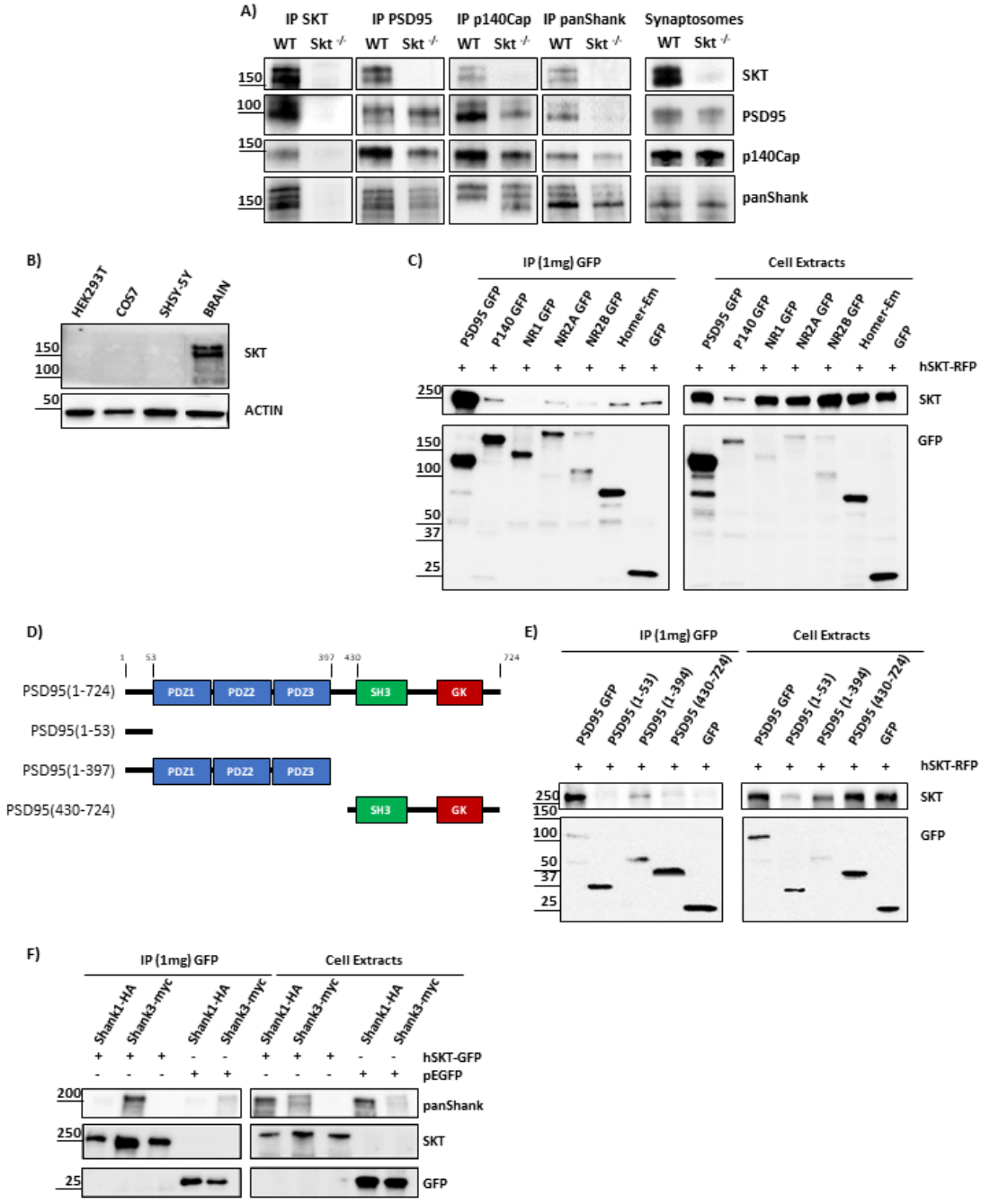

Figure 7 - SKT interacts with the adaptor proteins PSD-95, Shank3 and p140Cap.
A) Co-immunoprecipitation assay in crude synaptosomal preparations from WT mice. The co-IP showed the interaction of SKT with PSD-95, Shanks, and p140Cap in vivo; *Skt*$^{-/-}$ crude synaptosomes were used as negative control. Each co-IP assay was validated by the reverse immunoprecipitation experiments. 1 mg of crude synaptosome extract was used for each immunoprecipitation. 30µg of the crude synaptosomal extract was loaded as input control.
B) Lack of expression of SKT in extracts of HEK293T, COS7, and SHSY-5Y cells. 50 µg of cell extract was loaded and analyzed by WB with the SKT antibody. Mouse WT total brain was used as positive control.
C) Co-immunoprecipitation assay in HEK293T cell extracts. Extracts were prepared from HEK293T cells co-transfected with RFP-tagged hSKT construct, together with GFP-tagged PSD-95, p140Cap, NMDAR subunit GluN1, GluN2A, GluN2B, Homer1a plasmids or empty-GFP as negative control. Co-immunoprecipitations from HEK293T cell extracts (1 mg) were performed with GFP antibodies. Empty GFP was used as negative control. WB analysis revealed that hSKT strongly interacts with PSD-95 and p140Cap. Faint or no interactions were detected with the NMDA receptor subunits (GluN1, GluN2A, GluN2B) and Homer1a.
D) Schematic drawing of different GFP-tagged PSD95 fragments.
E) Co-immunoprecipitation assay in HEK293T cell extracts with PSD-95 domains. Extracts were prepared from HEK293T cells co-transfected with RFP-tagged hSKT, together with GFP-tagged PSD-95 full length or PSD-95 subdomains, as shown in D. Co-immunoprecipitation from HEK293T cell extracts (1mg) were performed with GFP antibodies. Empty GFP was used as negative control. WB analysis revealed that hSKT interacts with the PSD-95 (1-390) fragment that includes the three PDZ domains of PSD-95.
F) Co-immunoprecipitation assay in HEK293T cell extracts with Shank members. Extracts were prepared from HEK293T cells co-transfected with GFP-tagged hSKT, together with Shank members HA-tagged Shank1 or Shank3 plasmids. Co-immunoprecipitations from HEK293T cell extracts (1mg) were performed with GFP antibodies. Empty GFP was used as negative control. Antibodies that detect all

the Shank members (panSHANK) revealed that hSKT interacts with HA-Shank3 but not with HA-Shank1.

Figure 8 - The hSKT N-terminal region proximally interacts with the proteins PSD-95 and Shank3 in HEK293T cells.

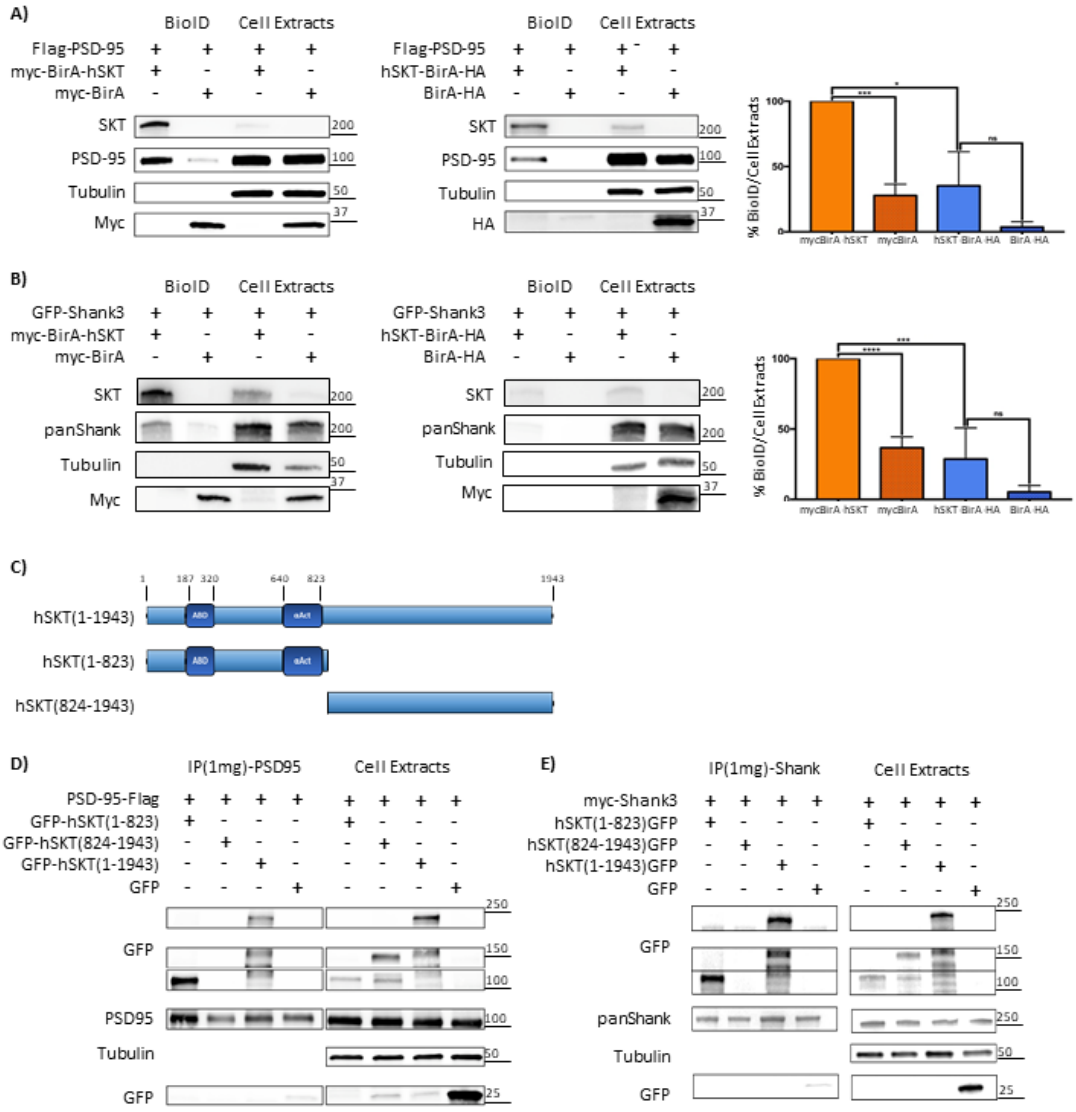

Figure 8 - The hSKT N-terminal region proximally interacts with the proteins PSD-95 and Shank3 in HEK293T cells.

A, B) BioID assay in HEK293T cell extracts. HEK293cells were co-transfected with each of the hSKT-BirA* fusion proteins, together with Flag-tagged PSD-95 **(A)** or HA-Shank3 **(B)** plasmids. As negative controls, HEK293T cells were transfected with empty BirA vectors. Biotinylated proteins were isolated through BioID assay and visualized through WB analysis. 30µg of extracts were subjected to SDS-PAGE and WB analysis. Proteins were detected using the indicated antibodies. hSKT proximally interacts with PSD-95 and Shank3. Tubulin was used as loading control. The ratio between the BioID assay and the normalized extract was performed; Student T-test was used. BioID assay of PSD-95 (n=3) and Shank3 (n=4) revealed that both proteins were biotinylated by Myc-BirA-hSKT, suggesting that the N-terminal region of hSKT is mainly involved in the interaction with both PSD-95 and Shank3.

Error bars correspond to ±SEM. *= p-value ≤ 0.05; ***= p-value ≤ 0.001; **** = p-value ≤ 0.0001

C) Schematic drawing of different GFP-tagged hSKT fragments.

D) Co-immunoprecipitation assay in HEK293T cell extracts for PSD-95 interaction. HEK293T cells co-transfected with GFP-tagged hSKT, or hSKT(1-823) and hSKT(824-1943) subdomain, as shown in C), or Flag-tagged PSD-95 full-length plasmids. Co-immunoprecipitations from HEK293 cell extracts (1mg) were performed with GFP antibodies. Empty GFP was used as negative control. The WB revealed that only the N-terminal part of hSKT, hSKT(1-823), interacts with PSD-95.

E) Co-immunoprecipitation assay in HEK293T cell extracts for Shank3. HEK293T cells co-transfected with GFP-tagged hSKT, or hSKT(1-823) and hSKT(824-1943) subdomain, as shown in C), or myc-tagged Shank3 plasmids. Co-immunoprecipitations from HEK293 cell extracts (1mg) were performed with GFP antibodies. Empty GFP was used as negative control. The WB revealed that only the N-terminal part of hSKT, hSKT(1-823), interacts with Shank3.

Figure 9 - SKT synaptic interactome identified by Mass Spectrometry analysis.

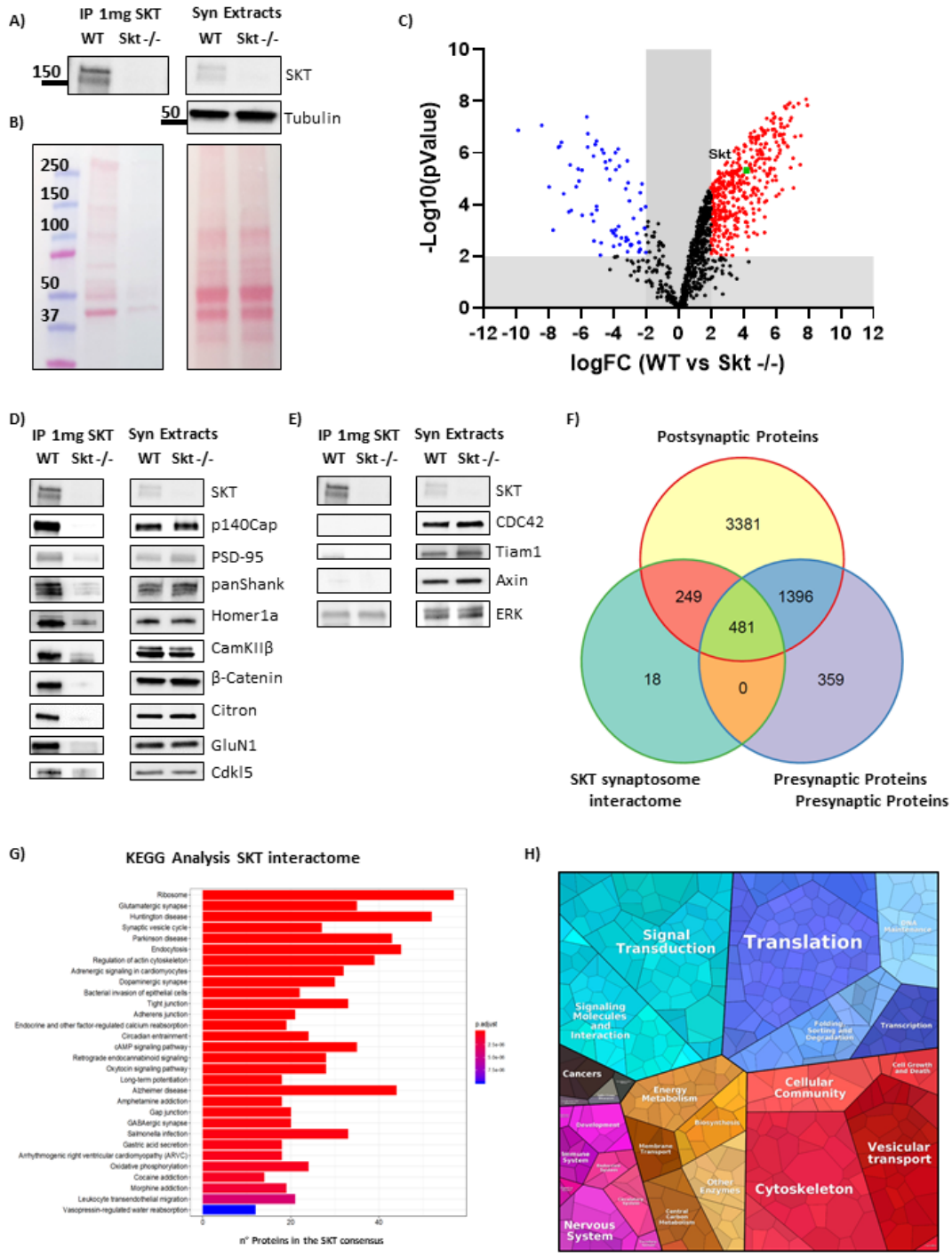

Figure 9 - SKT synaptic interactome identified by Mass Spectrometry analysis.

A) Specificity of the SKT immunoprecipitation. SKT was immunoprecipitated from 1mg synaptosomes prepared from WT and *Skt*$^{-/-}$ brain extracts. WB was performed by blotting with the SKT antibody.

B) S-Ponceau staining of 1mg SKT immunoprecipitates. Several specific bands were enriched in WT immunoprecipitate samples compared to *Skt*$^{-/-}$ immunoprecipitations.

C) The Volcano plot. The Volcano plot represents the log10(p-value) (y-axis) plotted against the logFC (fold change) (x-axis) for proteins quantified in SKT IPs from WT synaptosomes. *Skt*$^{-/-}$ crude synaptosomes were used as negative control. 748 different proteins (red dots), including SKT (green square dot), were significantly enriched in SKT specimens.

D) Validation of synaptic SKT interacting proteins identified in the interactome. 1mg of crude synaptosomal extract was immunoprecipitated with SKT antibody. 30µg of the crude synaptosomal extract was loaded as loading control. co-immunoprecipitated proteins are shown on the right.

E) Negative controls of synaptic SKT interactome. 1mg of crude synaptosome extract was immunoprecipitated with SKT antibody. 30 µg of crude synaptosomal extracts were used as loading control. Proteins that did not co-immunoprecipitated with SKT are shown on the right.

F) Venn diagram showing the overlap of 748 SKT interactors (green) mapped in presynaptic (purple) and postsynaptic (yellow) datasets. The chart shows that SKT interactors are exclusively postsynaptic or shared between pre and postsynapse compartments, while no exclusive presynaptic proteins are present.

G) KEGG pathway enrichment results of the WT SKT interactome. KEGG (Kyoto Encyclopedia of Genes and Genomes) analysis revealed that SKT is mainly involved in processes that regulate cytoskeleton, vesicle cycle, and glutamate receptor signaling pathways.

H) Proteomaps for the synaptic set of proteins (Liebermeister et al., 2014). The map is built corresponding to KEGG functional division for SKT synaptic interactome.

Figure 10 - Schematic model of hSKT in the association with PSD-95 and Shank3 platforms in dendritic spines.

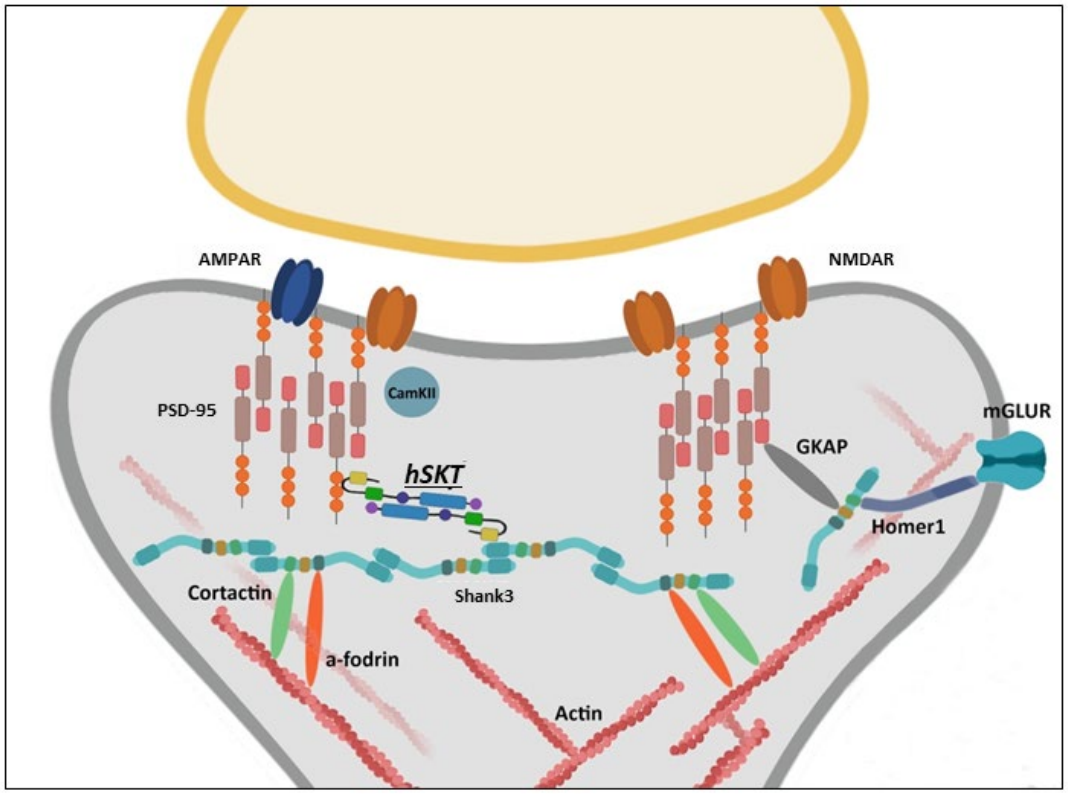

Figure 10 - Schematic model of hSKT in the association with PSD-95 and Shank3 platforms in dendritic spines.

The supposed role of hSKT complex in the organization of PSD-95 and Shank3 platforms during dendritic spines maturation.

Table 1 - Significantly enriched proteins in mass spectrometry.

First 60 enriched proteins found in SKT co-immunoprecipitation MS analysis. At the top of the list there are proteins used for interactome validation.

Gene Name	iBAQ Sum	logFC (WT vs SKT -/-)	Stoichiometry
Skt	**4,65E+06**	**7,050826868**	**1,0**
Dlg4	6,63E+07	4,023239185	**14,2**
Shank1	1,09E+07	4,6990798	**2,3**
Shank2	1,14E+07	4,433203486	**2,4**
Shank3	1,53E+07	4,622788675	**3,3**
Cit	1,59E+06	4,710692435	**0,3**
Ctnnd1	6,64E+05	6,573032136	**0,1**
Ctnna2	1,55E+07	5,348689539	**3,3**
Srcin1	2,47E+07	3,915203237	**5,3**
Cdkl5	1,47E+06	4,252712097	**0,3**
Grin1	1,43E+07	4,420301844	**3,1**
Gprin1	4,55E+06	3,564901709	**1,0**
Adam22	1,45E+06	9,593105936	**0,3**
Tjp2	9,95E+05	9,513281987	**0,2**
Rasal2	2,58E+06	9,386670809	**0,6**
Rpl18	7,18E+06	9,199564961	**1,5**
Dnm3	8,22E+05	9,158123868	**0,2**
Akap5	1,35E+06	9,05477409	**0,3**
Grm5	6,86E+05	8,831663707	**0,1**
Cep170	3,97E+05	8,741493432	**0,1**
Ckb	2,78E+06	8,741192399	**0,6**
Mecp2	2,05E+06	8,718608218	**0,4**
Arpc3	1,07E+07	8,6354054	**2,3**
Atp2b1	5,71E+05	8,616326445	**0,1**
Rpl15	3,25E+06	8,574307792	**0,7**
Ppp2r1a	9,89E+05	8,525218364	**0,2**
Clasp1	3,45E+05	8,516868351	**0,1**
Sipa1l3	3,01E+05	8,400737142	**0,1**
Hp1bp3	1,15E+06	8,388586787	**0,2**
Atp2b2	4,69E+05	8,369892117	**0,1**
Flii	5,48E+05	8,358618276	**0,1**
Scai	7,93E+05	8,292835178	**0,2**
Mtfr1l	2,03E+06	8,201747068	**0,4**
Sh3kbp1	7,70E+05	8,191934095	**0,2**
Arhgef2	4,23E+05	8,141528158	**0,1**
Efr3b	5,60E+05	8,123924755	**0,1**
Usp31	3,16E+05	8,088119812	**0,1**
Cep170b	5,60E+05	8,052935561	**0,1**
Sh3bgrl2	3,18E+06	8,047261514	**0,7**
2010300C02Rik	2,97E+05	8,009972341	**0,1**
Arc	1,42E+06	7,984309617	**0,3**
Csnk1d	1,15E+06	7,976632686	**0,2**
Cntfr	1,15E+06	7,962220538	**0,2**
Rims2	2,59E+05	7,924452978	**0,1**
Dmd	1,22E+05	7,924185779	**0,0**
Mapk8ip3	3,21E+05	7,92044633	**0,1**
Rps5	2,88E+06	7,87253828	**0,6**
Dync1li1	6,46E+05	7,871105395	**0,1**
Gabbr2	6,57E+05	7,852359732	**0,1**
Des	4,01E+07	7,835784777	**8,6**
Kcnq2	4,70E+05	7,81836806	**0,1**
Rpl4	5,99E+06	7,807086734	**1,3**
Rab11fip2	7,56E+05	7,750776866	**0,2**
Igsf9b	3,50E+05	7,685907634	**0,1**
Map4	3,62E+05	7,681229181	**0,1**
Rpl36	5,13E+06	7,680350256	**1,1**
Mark4	6,08E+05	7,672786215	**0,1**
Rpl35	6,01E+06	7,630775625	**1,3**
Sv2a	5,76E+05	7,620753993	**0,1**
Efhd1	1,14E+06	7,594575859	**0,2**

ACKNOWLEDGMENTS

Vorrei ringraziare innanzitutto la professoressa Defilippi per avermi accolto da diversi anni nel suo laboratorio ed aver sempre supportato la possibilità di esprimere le mie idee scientifiche. È stata sia un capo che una persona speciale con cui poter condividere momenti di vita quotidiana.
Ringrazio anche la professoressa Turco per avermi sempre spronato a migliorare e per tutti i preziosi consigli forniti in questi anni.

Ringrazio tutte le persone con cui ho collaborato e che hanno dato le loro competenze e il loro tempo per riuscire a concludere gli esperimenti necessari al lavoro. In particolare ad Antonia per tutti i suggerimenti ricevuti, ma anche per le sue richieste di transfettare un numero indefinito di piastre il venerdì sera per fare settordici IP in triplicato la settimana successiva!

Grazie alla mia mentore Annalisa, che mi ha insegnato un'infinità di cose!!! Grazie a tutti i compagni di laboratorio del gruppo Defilippi, sia presenti che passati. In particolare Costanza per l'aiuto, per i consigli, per tutte le risate fatte in questi anni! Grazie di cuore anche a Dora per aver condiviso tutte le mie sbroccate. Grazie ai miei studenti Federico, Olga e Rebecca che mi hanno stimolato a fare il meglio e che si sono dimostrati sempre anche degli ottimi aiuti per gli esperimenti e degli ottimi collaboratori con cui confrontarmi. A tutti loro auguro uno squisito futuro.
Grazie a Tiziana per tutte le risate e i momenti trascorsi in questi anni, ma soprattutto per il caffè delle 8:30 che ormai è un rito quotidiano senza il quale la giornata non può iniziare. Grazie a tutte le tecniche e i tecnici per tutti i loro preziosi consigli.

Grazie a tutti gli amici dell'MBC. Ogni momento con voi è stato speciale! Vorrei ringraziarvi tutti uno per uno, ma probabilmente servirebbero altre 100 pagine! Preferisco farlo con una buona bottiglia di prosecco quando festeggeremo il dottorato!

Grazie, grazie, grazie alla mia famiglia, mio padre Giuseppe, mia madre Manuela a mia sorella Elisa che mi hanno sempre fatto sentire la loro vicinanza anche se siamo lontani. E un ringraziamento di cuore a Sara per essermi stata accanto in tutto questo tempo per avermi sempre viziato e per aver condiviso tutti questi anni e spero molti altri ancora. Grazie a Mario, Marie, Silvia e Matteo per tutti i giorni trascorsi insieme. Grazie a Maki, la mia gattina, anche per aver tentato a contribuire, sebbene le avessi chiesto di non farlo, alla stesura di parte di questo elaborato.

Last but not the least, grazie ai "miei" topi"!!! Hanno sempre collaborato e anche a loro ci si affeziona. Inoltre, senza di loro, questo lavoro sarebbe stato molto più limitato.

BIBLIOGRAPHY

Al Dhaheri, N., Wu, N., Zhao, S., Wu, Z., Blank, R. D., Zhang, J., Raggio, C., Halanski, M., Shen, J., Noonan, K.*, et al.* (2020). KIAA1217: A novel candidate gene associated with isolated and syndromic vertebral malformations. American journal of medical genetics Part A *182*, 1664-1672.

Alfieri, A., Sorokina, O., Adrait, A., Angelini, C., Russo, I., Morellato, A., Matteoli, M., Menna, E., Boeri Erba, E., McLean, C.*, et al.* (2017). Synaptic Interactome Mining Reveals p140Cap as a New Hub for PSD Proteins Involved in Psychiatric and Neurological Disorders. Frontiers in molecular neuroscience *10*, 212.

Alie, A., and Manuel, M. (2010). The backbone of the post-synaptic density originated in a unicellular ancestor of choanoflagellates and metazoans. BMC evolutionary biology *10*, 34.

Ammer, A. G., and Weed, S. A. (2008). Cortactin branches out: roles in regulating protrusive actin dynamics. Cell motility and the cytoskeleton *65*, 687-707.

Attar, A., Liu, T., Chan, W. T., Hayes, J., Nejad, M., Lei, K., and Bitan, G. (2013). A shortened Barnes maze protocol reveals memory deficits at 4-months of age in the triple-transgenic mouse model of Alzheimer's disease. PloS one *8*, e80355.

Banker, G. (2018). The Development of Neuronal Polarity: A Retrospective View. The Journal of neuroscience : the official journal of the Society for Neuroscience *38*, 1867-1873.

Baron, M. K., Boeckers, T. M., Vaida, B., Faham, S., Gingery, M., Sawaya, M. R., Salyer, D., Gundelfinger, E. D., and Bowie, J. U. (2006). An architectural framework that may lie at the core of the postsynaptic density. Science *311*, 531-535.

Bats, C., Groc, L., and Choquet, D. (2007). The interaction between Stargazin and PSD-95 regulates AMPA receptor surface trafficking. Neuron *53*, 719-734.

Bayes, A., van de Lagemaat, L. N., Collins, M. O., Croning, M. D., Whittle, I. R., Choudhary, J. S., and Grant, S. G. (2011). Characterization of the proteome, diseases and evolution of the human postsynaptic density. Nature neuroscience *14*, 19-21.

Bean, B. P. (2007). The action potential in mammalian central neurons. Nature reviews Neuroscience *8*, 451-465.

Ben Abdallah, N. M., Fuss, J., Trusel, M., Galsworthy, M. J., Bobsin, K., Colacicco, G., Deacon, R. M., Riva, M. A., Kellendonk, C., Sprengel, R.*, et al.* (2011). The puzzle box as a simple and efficient behavioral test for exploring impairments of general cognition and executive functions in mouse models of schizophrenia. Experimental neurology *227*, 42-52.

Benarroch, E. E. (2013). Synaptic vesicle exocytosis: molecular mechanisms and clinical implications. Neurology *80*, 1981-1988.

Benes, F. M. (2000). Emerging principles of altered neural circuitry in schizophrenia. Brain research Brain research reviews *31*, 251-269.

Bey, A. L., Wang, X., Yan, H., Kim, N., Passman, R. L., Yang, Y., Cao, X., Towers, A. J., Hulbert, S. W., Duffney, L. J.*, et al.* (2018). Brain region-specific disruption of Shank3 in mice reveals a dissociation for cortical and striatal circuits in autism-related behaviors. Translational psychiatry *8*, 94.

Bhattacharyya, S., Biou, V., Xu, W., Schluter, O., and Malenka, R. C. (2009). A critical role for PSD-95/AKAP interactions in endocytosis of synaptic AMPA receptors. Nature neuroscience *12*, 172-181.

Bishop, A. L., and Hall, A. (2000). Rho GTPases and their effector proteins. The Biochemical journal *348 Pt 2*, 241-255.

Bockers, T. M., Mameza, M. G., Kreutz, M. R., Bockmann, J., Weise, C., Buck, F., Richter, D., Gundelfinger, E. D., and Kreienkamp, H. J. (2001). Synaptic scaffolding proteins in rat brain. Ankyrin repeats of the multidomain Shank protein family interact with the cytoskeletal protein alpha-fodrin. The Journal of biological chemistry *276*, 40104-40112.

Bockers, T. M., Segger-Junius, M., Iglauer, P., Bockmann, J., Gundelfinger, E. D., Kreutz, M. R., Richter, D., Kindler, S., and Kreienkamp, H. J. (2004). Differential expression and dendritic transcript localization of Shank family members: identification of a dendritic targeting element in the 3' untranslated region of Shank1 mRNA. Molecular and cellular neurosciences *26*, 182-190.

Boeckers, T. M., Bockmann, J., Kreutz, M. R., and Gundelfinger, E. D. (2002). ProSAP/Shank proteins - a family of higher order organizing molecules of the postsynaptic density with an emerging role in human neurological disease. Journal of neurochemistry *81*, 903-910.

Bonaglia, M. C., Giorda, R., Borgatti, R., Felisari, G., Gagliardi, C., Selicorni, A., and Zuffardi, O. (2001). Disruption of the ProSAP2 gene in a t(12;22)(q24.1;q13.3) is associated with the 22q13.3 deletion syndrome. American journal of human genetics *69*, 261-268.

Bourne, J., and Harris, K. M. (2007). Do thin spines learn to be mushroom spines that remember? Current opinion in neurobiology *17*, 381-386.

Bozdagi, O., Sakurai, T., Papapetrou, D., Wang, X., Dickstein, D. L., Takahashi, N., Kajiwara, Y., Yang, M., Katz, A. M., Scattoni, M. L.*, et al.* (2010). Haploinsufficiency of the autism-associated Shank3 gene leads to deficits in synaptic function, social interaction, and social communication. Molecular autism *1*, 15.

Brigman, J. L., Graybeal, C., and Holmes, A. (2010). Predictably irrational: assaying cognitive inflexibility in mouse models of schizophrenia. Frontiers in neuroscience *4*.

Cane, M., Maco, B., Knott, G., and Holtmaat, A. (2014). The relationship between PSD-95 clustering and spine stability in vivo. The Journal of neuroscience : the official journal of the Society for Neuroscience *34*, 2075-2086.

Chakravarthy, S., Keck, T., Roelandse, M., Hartman, R., Jeromin, A., Perry, S., Hofer, S. B., Mrsic-Flogel, T., and Levelt, C. N. (2008). Cre-dependent expression of multiple transgenes in isolated neurons of the adult forebrain. PloS one *3*, e3059.

Chan, C. S., Guzman, J. N., Ilijic, E., Mercer, J. N., Rick, C., Tkatch, T., Meredith, G. E., and Surmeier, D. J. (2007). 'Rejuvenation' protects neurons in mouse models of Parkinson's disease. Nature *447*, 1081-1086.

Chapelle, J., Baudino, A., Torelli, F., Savino, A., Morellato, A., Angelini, C., Salemme, V., Centonze, G., Natalini, D., Gai, M.*, et al.* (2020). The N-terminal domain of the adaptor protein p140Cap interacts with Tiam1 and controls Tiam1/Rac1 axis. American journal of cancer research *10*, 4308-4324.

Chatr-Aryamontri, A., Breitkreutz, B. J., Oughtred, R., Boucher, L., Heinicke, S., Chen, D., Stark, C., Breitkreutz, A., Kolas, N., O'Donnell, L.*, et al.* (2015). The BioGRID interaction database: 2015 update. Nucleic acids research *43*, D470-478.

Cheah, J. S., and Yamada, S. (2017). A simple elution strategy for biotinylated proteins bound to streptavidin conjugated beads using excess biotin and heat. Biochemical and biophysical research communications *493*, 1522-1527.

Chen, H. J., Rojas-Soto, M., Oguni, A., and Kennedy, M. B. (1998). A synaptic Ras-GTPase activating protein (p135 SynGAP) inhibited by CaM kinase II. Neuron *20*, 895-904.

Cirulli, E. T., Kasperaviciute, D., Attix, D. K., Need, A. C., Ge, D., Gibson, G., and Goldstein, D. B. (2010). Common genetic variation and performance on standardized cognitive tests. European journal of human genetics : EJHG *18*, 815-820.

Cox, J., and Mann, M. (2008). MaxQuant enables high peptide identification rates, individualized p.p.b.-range mass accuracies and proteome-wide protein quantification. Nature biotechnology *26*, 1367-1372.

Craven, S. E., El-Husseini, A. E., and Bredt, D. S. (1999). Synaptic targeting of the postsynaptic density protein PSD-95 mediated by lipid and protein motifs. Neuron *22*, 497-509.

Di Stefano, P., Damiano, L., Cabodi, S., Aramu, S., Tordella, L., Praduroux, A., Piva, R., Cavallo, F., Forni, G., Silengo, L.*, et al.* (2007). p140Cap protein suppresses tumour cell properties, regulating Csk and Src kinase activity. The EMBO journal *26*, 2843-2855.

Dickson, B. J. (2001). Rho GTPases in growth cone guidance. Current opinion in neurobiology *11*, 103-110.

Dityatev, A., and Rusakov, D. A. (2011). Molecular signals of plasticity at the tetrapartite synapse. Current opinion in neurobiology *21*, 353-359.

Durand, C. M., Perroy, J., Loll, F., Perrais, D., Fagni, L., Bourgeron, T., Montcouquiol, M., and Sans, N. (2012). SHANK3 mutations identified in autism lead to modification of dendritic spine morphology via an actin-dependent mechanism. Molecular psychiatry *17*, 71-84.

Engert, F., and Bonhoeffer, T. (1999). Dendritic spine changes associated with hippocampal long-term synaptic plasticity. Nature *399*, 66-70.

Farhy-Tselnicker, I., and Allen, N. J. (2018). Astrocytes, neurons, synapses: a tripartite view on cortical circuit development. Neural development *13*, 7.

Fischer, M., Kaech, S., Wagner, U., Brinkhaus, H., and Matus, A. (2000). Glutamate receptors regulate actin-based plasticity in dendritic spines. Nature neuroscience *3*, 887-894.

Gallone, G., Simpson, T. I., Armstrong, J. D., and Jarman, A. P. (2011). Bio::Homology::InterologWalk--a Perl module to build putative protein-protein interaction networks through interolog mapping. BMC bioinformatics *12*, 289.

Gavello, D., Vandael, D. H., Cesa, R., Premoselli, F., Marcantoni, A., Cesano, F., Scarano, D., Fubini, B., Carbone, E., Fenoglio, I., and Carabelli, V. (2012). Altered excitability of cultured chromaffin cells following exposure to multi-walled carbon nanotubes. Nanotoxicology *6*, 47-60.

Grabrucker, S., Proepper, C., Mangus, K., Eckert, M., Chhabra, R., Schmeisser, M. J., Boeckers, T. M., and Grabrucker, A. M. (2014). The PSD protein ProSAP2/Shank3 displays synapto-nuclear shuttling which is deregulated in a schizophrenia-associated mutation. Experimental neurology *253*, 126-137.

Grant, S. G. (2013). SnapShot: Organizational principles of the postsynaptic proteome. Neuron *80*, 534 e531.

Grant, S. G. N. (2019). Synapse diversity and synaptome architecture in human genetic disorders. Human molecular genetics *28*, R219-R225.

Grove, J., Ripke, S., Als, T. D., Mattheisen, M., Walters, R. K., Won, H., Pallesen, J., Agerbo, E., Andreassen, O. A., Anney, R.*, et al.* (2019). Identification of common genetic risk variants for autism spectrum disorder. Nature genetics *51*, 431-444.

Guan, X., Ni, B., Zhang, J., Man, C., Cai, Z., Meng, W., Shi, L., and Ross-Degnan, D. (2020). The Impact of Physicians' Working Hours on Inappropriate Use of Outpatient Medicine in a Tertiary Hospital in China. Applied health economics and health policy *18*, 443-451.

Guilmatre, A., Huguet, G., Delorme, R., and Bourgeron, T. (2014). The emerging role of SHANK genes in neuropsychiatric disorders. Developmental neurobiology *74*, 113-122.

Gundelfinger, E. D., Boeckers, T. M., Baron, M. K., and Bowie, J. U. (2006). A role for zinc in postsynaptic density asSAMbly and plasticity? Trends in biochemical sciences *31*, 366-373.

Ha, H. T. T., Leal-Ortiz, S., Lalwani, K., Kiyonaka, S., Hamachi, I., Mysore, S. P., Montgomery, J. M., Garner, C. C., Huguenard, J. R., and Kim, S. A. (2018). Shank and Zinc Mediate an AMPA Receptor Subunit Switch in Developing Neurons. Frontiers in molecular neuroscience *11*, 405.

Haeckel, A., Ahuja, R., Gundelfinger, E. D., Qualmann, B., and Kessels, M. M. (2008). The actin-binding protein Abp1 controls dendritic spine morphology and is important for spine head and synapse formation. The Journal of neuroscience : the official journal of the Society for Neuroscience *28*, 10031-10044.

Harris, K. P., Akbergenova, Y., Cho, R. W., Baas-Thomas, M. S., and Littleton, J. T. (2016). Shank Modulates Postsynaptic Wnt Signaling to Regulate Synaptic Development. The Journal of neuroscience : the official journal of the Society for Neuroscience *36*, 5820-5832.

Hassani Nia, F., and Kreienkamp, H. J. (2018). Functional Relevance of Missense Mutations Affecting the N-Terminal Part of Shank3 Found in Autistic Patients. Frontiers in molecular neuroscience *11*, 268.

Hayashi, Y., and Majewska, A. K. (2005). Dendritic spine geometry: functional implication and regulation. Neuron *46*, 529-532.

Hering, H., and Sheng, M. (2003). Activity-dependent redistribution and essential role of cortactin in dendritic spine morphogenesis. The Journal of neuroscience : the official journal of the Society for Neuroscience *23*, 11759-11769.

Holtmaat, A. J., Trachtenberg, J. T., Wilbrecht, L., Shepherd, G. M., Zhang, X., Knott, G. W., and Svoboda, K. (2005). Transient and persistent dendritic spines in the neocortex in vivo. Neuron *45*, 279-291.

Hung, A. Y., and Sheng, M. (2002). PDZ domains: structural modules for protein complex assembly. The Journal of biological chemistry *277*, 5699-5702.

Iasevoli, F., Tomasetti, C., and de Bartolomeis, A. (2013). Scaffolding proteins of the post-synaptic density contribute to synaptic plasticity by regulating receptor localization and distribution: relevance for neuropsychiatric diseases. Neurochemical research *38*, 1-22.

Jahn, R., and Fasshauer, D. (2012). Molecular machines governing exocytosis of synaptic vesicles. Nature *490*, 201-207.

Jaworski, J., Kapitein, L. C., Gouveia, S. M., Dortland, B. R., Wulf, P. S., Grigoriev, I., Camera, P., Spangler, S. A., Di Stefano, P., Demmers, J.*, et al.* (2009). Dynamic microtubules regulate dendritic spine morphology and synaptic plasticity. Neuron *61*, 85-100.

Jiang, Y. H., and Ehlers, M. D. (2013). Modeling autism by SHANK gene mutations in mice. Neuron *78*, 8-27.

Karasugi, T., Semba, K., Hirose, Y., Kelempisioti, A., Nakajima, M., Miyake, A., Furuichi, T., Kawaguchi, Y., Mikami, Y., Chiba, K.*, et al.* (2009). Association of the tag SNPs in the human SKT gene (KIAA1217) with lumbar disc herniation. Journal of bone and mineral research : the official journal of the American Society for Bone and Mineral Research *24*, 1537-1543.

Kerrien, S., Aranda, B., Breuza, L., Bridge, A., Broackes-Carter, F., Chen, C., Duesbury, M., Dumousseau, M., Feuermann, M., Hinz, U.*, et al.* (2012). The IntAct molecular interaction database in 2012. Nucleic acids research *40*, D841-846.

Kim, E., and Sheng, M. (2004). PDZ domain proteins of synapses. Nature reviews Neuroscience *5*, 771-781.

Kim, J. H., Liao, D., Lau, L. F., and Huganir, R. L. (1998). SynGAP: a synaptic RasGAP that associates with the PSD-95/SAP90 protein family. Neuron *20*, 683-691.

Kingston, R. E., Chen, C. A., and Okayama, H. (2003). Calcium phosphate transfection. Current protocols in cell biology *Chapter 20*, Unit 20 23.

Knowles, E. E., Mathias, S. R., McKay, D. R., Sprooten, E., Blangero, J., Almasy, L., and Glahn, D. C. (2014). Genome-Wide Analyses of Working-Memory Ability: A Review. Current behavioral neuroscience reports *1*, 224-233.

Koleske, A. J. (2013). Molecular mechanisms of dendrite stability. Nature reviews Neuroscience *14*, 536-550.

Kumar, P., Nagarajan, A., and Uchil, P. D. (2019). Transfection of Mammalian Cells with Calcium Phosphate-DNA Coprecipitates. Cold Spring Harbor protocols *2019*.

Lee, K., Vyas, Y., Garner, C. C., and Montgomery, J. M. (2019). Autism-associated Shank3 mutations alter mGluR expression and mGluR-dependent but not NMDA receptor-dependent long-term depression. Synapse *73*, e22097.

Lee, T., Winter, C., Marticke, S. S., Lee, A., and Luo, L. (2000). Essential roles of Drosophila RhoA in the regulation of neuroblast proliferation and dendritic but not axonal morphogenesis. Neuron *25*, 307-316.

Lendvai, B., Stern, E. A., Chen, B., and Svoboda, K. (2000). Experience-dependent plasticity of dendritic spines in the developing rat barrel cortex in vivo. Nature *404*, 876-881.

Li, X., Saint-Cyr-Proulx, E., Aktories, K., and Lamarche-Vane, N. (2002a). Rac1 and Cdc42 but not RhoA or Rho kinase activities are required for neurite outgrowth induced by the Netrin-1 receptor DCC (deleted in colorectal cancer) in N1E-115 neuroblastoma cells. The Journal of biological chemistry *277*, 15207-15214.

Li, Z., Aizenman, C. D., and Cline, H. T. (2002b). Regulation of rho GTPases by crosstalk and neuronal activity in vivo. Neuron *33*, 741-750.

Liebermeister, W., Noor, E., Flamholz, A., Davidi, D., Bernhardt, J., and Milo, R. (2014). Visual account of protein investment in cellular functions. Proceedings of the National Academy of Sciences of the United States of America *111*, 8488-8493.

Lim, S., Naisbitt, S., Yoon, J., Hwang, J. I., Suh, P. G., Sheng, M., and Kim, E. (1999). Characterization of the Shank family of synaptic proteins. Multiple genes, alternative splicing, and differential expression in brain and development. The Journal of biological chemistry *274*, 29510-29518.

Lu, C., Chen, Q., Zhou, T., Bozic, D., Fu, Z., Pan, J. Q., and Feng, G. (2016). Micro-electrode array recordings reveal reductions in both excitation and inhibition in cultured cortical neuron networks lacking Shank3. Molecular psychiatry *21*, 159-168.

Luo, F., Yang, Y., Chen, C. F., Chang, R., Zhou, J., and Scheuermann, R. H. (2007). Modular organization of protein interaction networks. Bioinformatics *23*, 207-214.

Luo, L. (2000). Rho GTPases in neuronal morphogenesis. Nature reviews Neuroscience *1*, 173-180.

Luo, L., Hensch, T. K., Ackerman, L., Barbel, S., Jan, L. Y., and Jan, Y. N. (1996a). Differential effects of the Rac GTPase on Purkinje cell axons and dendritic trunks and spines. Nature *379*, 837-840.

Luo, L., Jan, L., and Jan, Y. N. (1996b). Small GTPases in axon outgrowth. Perspectives on developmental neurobiology *4*, 199-204.

Maletic-Savatic, M., Malinow, R., and Svoboda, K. (1999). Rapid dendritic morphogenesis in CA1 hippocampal dendrites induced by synaptic activity. Science *283*, 1923-1927.

Martinez-Quiles, N., Ho, H. Y., Kirschner, M. W., Ramesh, N., and Geha, R. S. (2004). Erk/Src phosphorylation of cortactin acts as a switch on-switch off mechanism that controls its ability to activate N-WASP. Molecular and cellular biology *24*, 5269-5280.

Matsuzaki, M., Ellis-Davies, G. C., Nemoto, T., Miyashita, Y., Iino, M., and Kasai, H. (2001). Dendritic spine geometry is critical for AMPA receptor expression in hippocampal CA1 pyramidal neurons. Nature neuroscience *4*, 1086-1092.

McGee, A. W., Dakoji, S. R., Olsen, O., Bredt, D. S., Lim, W. A., and Prehoda, K. E. (2001). Structure of the SH3-guanylate kinase module from PSD-95 suggests a mechanism for regulated assembly of MAGUK scaffolding proteins. Molecular cell *8*, 1291-1301.

Meng, X. L., Shen, J. S., Kawagoe, S., Ohashi, T., Brady, R. O., and Eto, Y. (2010). Induced pluripotent stem cells derived from mouse models of lysosomal storage disorders. Proceedings of the National Academy of Sciences of the United States of America *107*, 7886-7891.

Meyer, D., Bonhoeffer, T., and Scheuss, V. (2014). Balance and stability of synaptic structures during synaptic plasticity. Neuron *82*, 430-443.

Migaud, M., Charlesworth, P., Dempster, M., Webster, L. C., Watabe, A. M., Makhinson, M., He, Y., Ramsay, M. F., Morris, R. G., Morrison, J. H.*, et al.* (1998). Enhanced long-term potentiation and impaired learning in mice with mutant postsynaptic density-95 protein. Nature *396*, 433-439.

Mirnics, K., Middleton, F. A., Lewis, D. A., and Levitt, P. (2001). Analysis of complex brain disorders with gene expression microarrays: schizophrenia as a disease of the synapse. Trends in neurosciences *24*, 479-486.

Monteiro, P., and Feng, G. (2017). SHANK proteins: roles at the synapse and in autism spectrum disorder. Nature reviews Neuroscience *18*, 147-157.

Morabito, M. A., Sheng, M., and Tsai, L. H. (2004). Cyclin-dependent kinase 5 phosphorylates the N-terminal domain of the postsynaptic density protein PSD-95 in neurons. The Journal of neuroscience : the official journal of the Society for Neuroscience *24*, 865-876.

Murakoshi, H., Wang, H., and Yasuda, R. (2011). Local, persistent activation of Rho GTPases during plasticity of single dendritic spines. Nature *472*, 100-104.

Naisbitt, S., Kim, E., Tu, J. C., Xiao, B., Sala, C., Valtschanoff, J., Weinberg, R. J., Worley, P. F., and Sheng, M. (1999). Shank, a novel family of postsynaptic density proteins that binds to the NMDA receptor/PSD-95/GKAP complex and cortactin. Neuron *23*, 569-582.

Naisbitt, S., Kim, E., Weinberg, R. J., Rao, A., Yang, F. C., Craig, A. M., and Sheng, M. (1997). Characterization of guanylate kinase-associated protein, a postsynaptic density protein at excitatory synapses that interacts directly with postsynaptic density-95/synapse-associated protein 90. The Journal of neuroscience : the official journal of the Society for Neuroscience *17*, 5687-5696.

Nakayama, A. Y., Harms, M. B., and Luo, L. (2000). Small GTPases Rac and Rho in the maintenance of dendritic spines and branches in hippocampal pyramidal neurons. The Journal of neuroscience : the official journal of the Society for Neuroscience *20*, 5329-5338.

Ovchinnikov, D. (2009). Alcian blue/alizarin red staining of cartilage and bone in mouse. Cold Spring Harbor protocols *2009*, pdb prot5170.

Owald, D., and Sigrist, S. J. (2009). Assembling the presynaptic active zone. Current opinion in neurobiology *19*, 311-318.

Pagani, M., Bertero, A., Liska, A., Galbusera, A., Sabbioni, M., Barsotti, N., Colenbier, N., Marinazzo, D., Scattoni, M. L., Pasqualetti, M., and Gozzi, A. (2019). Deletion of Autism Risk Gene Shank3 Disrupts Prefrontal Connectivity. The Journal of neuroscience : the official journal of the Society for Neuroscience *39*, 5299-5310.

Paulin, J. J., Haslehurst, P., Fellows, A. D., Liu, W., Jackson, J. D., Joel, Z., Cummings, D. M., and Edwards, F. A. (2016). Large and Small Dendritic Spines Serve Different Interacting Functions in Hippocampal Synaptic Plasticity and Homeostasis. Neural plasticity *2016*, 6170509.

Pavlos, N. J., Gronborg, M., Riedel, D., Chua, J. J., Boyken, J., Kloepper, T. H., Urlaub, H., Rizzoli, S. O., and Jahn, R. (2010). Quantitative analysis of synaptic vesicle Rabs uncovers distinct yet overlapping roles for Rab3a and Rab27b in Ca2+-triggered exocytosis. The Journal of neuroscience : the official journal of the Society for Neuroscience *30*, 13441-13453.

Peca, J., Feliciano, C., Ting, J. T., Wang, W., Wells, M. F., Venkatraman, T. N., Lascola, C. D., Fu, Z., and Feng, G. (2011). Shank3 mutant mice display autistic-like behaviours and striatal dysfunction. Nature *472*, 437-442.

Penzes, P., Cahill, M. E., Jones, K. A., VanLeeuwen, J. E., and Woolfrey, K. M. (2011). Dendritic spine pathology in neuropsychiatric disorders. Nature neuroscience *14*, 285-293.

Penzes, P., Johnson, R. C., Sattler, R., Zhang, X., Huganir, R. L., Kambampati, V., Mains, R. E., and Eipper, B. A. (2001). The neuronal Rho-GEF Kalirin-7 interacts with PDZ domain-containing proteins and regulates dendritic morphogenesis. Neuron *29*, 229-242.

Perea, G., Navarrete, M., and Araque, A. (2009). Tripartite synapses: astrocytes process and control synaptic information. Trends in neurosciences *32*, 421-431.

Perfitt, T. L., Stauffer, P. E., Spiess, K. L., and Colbran, R. J. (2020). CaMKIIalpha phosphorylation of Shank3 modulates ABI1-Shank3 interaction. Biochemical and biophysical research communications *524*, 262-267.

Phelan, K., Rogers, R. C., and Boccuto, L. (1993). Phelan-McDermid Syndrome. In GeneReviews((R)), M.P. Adam, H.H. Ardinger, R.A. Pagon, S.E. Wallace, L.J.H. Bean, K.W. Gripp, G.M. Mirzaa, and A. Amemiya, eds. (Seattle (WA)).

Phillips, M., and Pozzo-Miller, L. (2015). Dendritic spine dysgenesis in autism related disorders. Neuroscience letters *601*, 30-40.

Qualmann, B., Boeckers, T. M., Jeromin, M., Gundelfinger, E. D., and Kessels, M. M. (2004). Linkage of the actin cytoskeleton to the postsynaptic density via direct interactions of Abp1 with the ProSAP/Shank family. The Journal of neuroscience : the official journal of the Society for Neuroscience *24*, 2481-2495.

Quitsch, A., Berhorster, K., Liew, C. W., Richter, D., and Kreienkamp, H. J. (2005). Postsynaptic shank antagonizes dendrite branching induced by the leucine-rich repeat protein Densin-180. The Journal of neuroscience : the official journal of the Society for Neuroscience *25*, 479-487.

Rajan, I., and Cline, H. T. (1998). Glutamate receptor activity is required for normal development of tectal cell dendrites in vivo. The Journal of neuroscience : the official journal of the Society for Neuroscience *18*, 7836-7846.

Repetto, D., Camera, P., Melani, R., Morello, N., Russo, I., Calcagno, E., Tomasoni, R., Bianchi, F., Berto, G., Giustetto, M.*, et al.* (2014). p140Cap regulates memory and synaptic

plasticity through Src-mediated and citron-N-mediated actin reorganization. The Journal of neuroscience : the official journal of the Society for Neuroscience *34*, 1542-1553.

Roux, K. J., Kim, D. I., Burke, B., and May, D. G. (2018). BioID: A Screen for Protein-Protein Interactions. Current protocols in protein science *91*, 19 23 11-19 23 15.

Roy, M., Sorokina, O., Skene, N., Simonnet, C., Mazzo, F., Zwart, R., Sher, E., Smith, C., Armstrong, J. D., and Grant, S. G. N. (2018). Proteomic analysis of postsynaptic proteins in regions of the human neocortex. Nature neuroscience *21*, 130-138.

Ruchhoeft, M. L., Ohnuma, S., McNeill, L., Holt, C. E., and Harris, W. A. (1999). The neuronal architecture of Xenopus retinal ganglion cells is sculpted by rho-family GTPases in vivo. The Journal of neuroscience : the official journal of the Society for Neuroscience *19*, 8454-8463.

Russo, I., Gavello, D., Menna, E., Vandael, D., Veglia, C., Morello, N., Corradini, I., Focchi, E., Alfieri, A., Angelini, C.,Morellato, A., *et al.* (2019). p140Cap Regulates GABAergic Synaptogenesis and Development of Hippocampal Inhibitory Circuits. Cerebral cortex *29*, 91-105.

Sala, C., Vicidomini, C., Bigi, I., Mossa, A., and Verpelli, C. (2015). Shank synaptic scaffold proteins: keys to understanding the pathogenesis of autism and other synaptic disorders. Journal of neurochemistry *135*, 849-858.

Salemme, V., Angelini, C., Chapelle, J., Centonze, G., Natalini, D., Morellato, A., Taverna, D., Turco, E., Ala, U., and Defilippi, P. (2021). The p140Cap adaptor protein as a molecular hub to block cancer aggressiveness. Cellular and molecular life sciences : CMLS *78*, 1355-1367.

Schafer, M., Lkhagvasuren, O., Klein, H. U., Elling, C., Wustefeld, T., Muller-Tidow, C., Zender, L., Koschmieder, S., Dugas, M., and Ickstadt, K. (2012). Integrative analyses for omics data: a Bayesian mixture model to assess the concordance of ChIP-chip and ChIP-seq measurements. Journal of toxicology and environmental health Part A *75*, 461-470.

Schwanhausser, B., Busse, D., Li, N., Dittmar, G., Schuchhardt, J., Wolf, J., Chen, W., and Selbach, M. (2011). Global quantification of mammalian gene expression control. Nature *473*, 337-342.

Sears, R. M., May, D. G., and Roux, K. J. (2019). BioID as a Tool for Protein-Proximity Labeling in Living Cells. Methods in molecular biology *2012*, 299-313.

Semba, K., Araki, K., Li, Z., Matsumoto, K., Suzuki, M., Nakagata, N., Takagi, K., Takeya, M., Yoshinobu, K., Araki, M.*, et al.* (2006). A novel murine gene, Sickle tail, linked to the Danforth's short tail locus, is required for normal development of the intervertebral disc. Genetics *172*, 445-456.

Sheng, M., and Kim, E. (2000). The Shank family of scaffold proteins. Journal of cell science *113 (Pt 11)*, 1851-1856.

Sheng, M., and Kim, E. (2011). The postsynaptic organization of synapses. Cold Spring Harbor perspectives in biology *3*.

Sheng, M., and Kim, M. J. (2002). Postsynaptic signaling and plasticity mechanisms. Science *298*, 776-780.

Simpson, T. I., Armstrong, J. D., and Jarman, A. P. (2010). Merged consensus clustering to assess and improve class discovery with microarray data. BMC bioinformatics *11*, 590.

Solopov, V. N., and Lunichkina, I. V. (1988). [Endobronchial therapy of patients with chronic bronchitis]. Klinicheskaia meditsina *66*, 33-36.

Song, I., and Dityatev, A. (2018). Crosstalk between glia, extracellular matrix and neurons. Brain research bulletin *136*, 101-108.

Suda, H., Lee, K. J., Semba, K., Kyushima, F., Ando, T., Araki, M., Araki, K., Inomata, Y., and Yamamura, K. (2011). The Skt gene, required for anorectal development, is a candidate for a molecular marker of the cloacal plate. Pediatric surgery international *27*, 269-273.

Sudhof, T. C. (2004). The synaptic vesicle cycle. Annual review of neuroscience *27*, 509-547.

Sudhof, T. C. (2012). The presynaptic active zone. Neuron *75*, 11-25.

Sweet, E. S., Previtera, M. L., Fernandez, J. R., Charych, E. I., Tseng, C. Y., Kwon, M., Starovoytov, V., Zheng, J. Q., and Firestein, B. L. (2011). PSD-95 alters microtubule dynamics via an association with EB3. The Journal of neuroscience : the official journal of the Society for Neuroscience *31*, 1038-1047.

Tao-Cheng, J. H., Toy, D., Winters, C. A., Reese, T. S., and Dosemeci, A. (2016). Zinc Stabilizes Shank3 at the Postsynaptic Density of Hippocampal Synapses. PloS one *11*, e0153979.

Tashiro, A., Minden, A., and Yuste, R. (2000). Regulation of dendritic spine morphology by the rho family of small GTPases: antagonistic roles of Rac and Rho. Cerebral cortex *10*, 927-938.

Tavares, G. A., Panepucci, E. H., and Brunger, A. T. (2001). Structural characterization of the intramolecular interaction between the SH3 and guanylate kinase domains of PSD-95. Molecular cell *8*, 1313-1325.

Threadgill, R., Bobb, K., and Ghosh, A. (1997). Regulation of dendritic growth and remodeling by Rho, Rac, and Cdc42. Neuron *19*, 625-634.

Tomasoni, R., Repetto, D., Morini, R., Elia, C., Gardoni, F., Di Luca, M., Turco, E., Defilippi, P., and Matteoli, M. (2013). SNAP-25 regulates spine formation through postsynaptic binding to p140Cap. Nature communications *4*, 2136.

Trachtenberg, J. T., Chen, B. E., Knott, G. W., Feng, G., Sanes, J. R., Welker, E., and Svoboda, K. (2002). Long-term in vivo imaging of experience-dependent synaptic plasticity in adult cortex. Nature *420*, 788-794.

Traynelis, S. F., Wollmuth, L. P., McBain, C. J., Menniti, F. S., Vance, K. M., Ogden, K. K., Hansen, K. B., Yuan, H., Myers, S. J., and Dingledine, R. (2010). Glutamate receptor ion channels: structure, regulation, and function. Pharmacological reviews *62*, 405-496.

Tu, J. C., Xiao, B., Naisbitt, S., Yuan, J. P., Petralia, R. S., Brakeman, P., Doan, A., Aakalu, V. K., Lanahan, A. A., Sheng, M., and Worley, P. F. (1999). Coupling of mGluR/Homer and PSD-95 complexes by the Shank family of postsynaptic density proteins. Neuron *23*, 583-592.

Uchino, S., Wada, H., Honda, S., Nakamura, Y., Ondo, Y., Uchiyama, T., Tsutsumi, M., Suzuki, E., Hirasawa, T., and Kohsaka, S. (2006). Direct interaction of post-synaptic density-95/Dlg/ZO-1 domain-containing synaptic molecule Shank3 with GluR1 alpha-amino-3-hydroxy-5-methyl-4-isoxazole propionic acid receptor. Journal of neurochemistry *97*, 1203-1214.

Van Aelst, L., and Cline, H. T. (2004). Rho GTPases and activity-dependent dendrite development. Current opinion in neurobiology *14*, 297-304.

Verpelli, C., Dvoretskova, E., Vicidomini, C., Rossi, F., Chiappalone, M., Schoen, M., Di Stefano, B., Mantegazza, R., Broccoli, V., Bockers, T. M.*, et al.* (2011). Importance of Shank3 protein in regulating metabotropic glutamate receptor 5 (mGluR5) expression and signaling at synapses. The Journal of biological chemistry *286*, 34839-34850.

Vuksic, M., Del Turco, D., Bas Orth, C., Burbach, G. J., Feng, G., Muller, C. M., Schwarzacher, S. W., and Deller, T. (2008). 3D-reconstruction and functional properties of GFP-positive and GFP-negative granule cells in the fascia dentata of the Thy1-GFP mouse. Hippocampus *18*, 364-375.

Waga, C., Asano, H., Sanagi, T., Suzuki, E., Nakamura, Y., Tsuchiya, A., Itoh, M., Goto, Y., Kohsaka, S., and Uchino, S. (2014). Identification of two novel Shank3 transcripts in the developing mouse neocortex. Journal of neurochemistry *128*, 280-293.

Wang, X., Bey, A. L., Katz, B. M., Badea, A., Kim, N., David, L. K., Duffney, L. J., Kumar, S., Mague, S. D., Hulbert, S. W.*, et al.* (2016). Altered mGluR5-Homer scaffolds and corticostriatal connectivity in a Shank3 complete knockout model of autism. Nature communications *7*, 11459.

Weaver, A. M., Young, M. E., Lee, W. L., and Cooper, J. A. (2003). Integration of signals to the Arp2/3 complex. Current opinion in cell biology *15*, 23-30.

Whitford, K. L., Dijkhuizen, P., Polleux, F., and Ghosh, A. (2002). Molecular control of cortical dendrite development. Annual review of neuroscience *25*, 127-149.

Wilson, H. L., Wong, A. C., Shaw, S. R., Tse, W. Y., Stapleton, G. A., Phelan, M. C., Hu, S., Marshall, J., and McDermid, H. E. (2003). Molecular characterisation of the 22q13 deletion syndrome supports the role of haploinsufficiency of SHANK3/PROSAP2 in the major neurological symptoms. Journal of medical genetics *40*, 575-584.

Wong, W. T., Faulkner-Jones, B. E., Sanes, J. R., and Wong, R. O. (2000). Rapid dendritic remodeling in the developing retina: dependence on neurotransmission and reciprocal regulation by Rac and Rho. The Journal of neuroscience : the official journal of the Society for Neuroscience *20*, 5024-5036.

Xing, L., Yao, X., Williams, K. R., and Bassell, G. J. (2012). Negative regulation of RhoA translation and signaling by hnRNP-Q1 affects cellular morphogenesis. Molecular biology of the cell *23*, 1500-1509.

Yamashita, T., Tucker, K. L., and Barde, Y. A. (1999). Neurotrophin binding to the p75 receptor modulates Rho activity and axonal outgrowth. Neuron *24*, 585-593.

Yang, M., Bozdagi, O., Scattoni, M. L., Wohr, M., Roullet, F. I., Katz, A. M., Abrams, D. N., Kalikhman, D., Simon, H., Woldeyohannes, L.*, et al.* (2012). Reduced excitatory neurotransmission and mild autism-relevant phenotypes in adolescent Shank3 null mutant mice. The Journal of neuroscience : the official journal of the Society for Neuroscience *32*, 6525-6541.

Yu, G., Wang, L. G., Han, Y., and He, Q. Y. (2012). clusterProfiler: an R package for comparing biological themes among gene clusters. Omics : a journal of integrative biology *16*, 284-287.

Yuste, R., and Bonhoeffer, T. (2001). Morphological changes in dendritic spines associated with long-term synaptic plasticity. Annual review of neuroscience *24*, 1071-1089.

Zhang, H., Maximov, A., Fu, Y., Xu, F., Tang, T. S., Tkatch, T., Surmeier, D. J., and Bezprozvanny, I. (2005). Association of CaV1.3 L-type calcium channels with Shank. The Journal of neuroscience : the official journal of the Society for Neuroscience *25*, 1037-1049.

Zheng, Y., Stephan, M. T., Gai, S. A., Abraham, W., Shearer, A., and Irvine, D. J. (2013). In vivo targeting of adoptively transferred T-cells with antibody- and cytokine-conjugated liposomes. Journal of controlled release : official journal of the Controlled Release Society *172*, 426-435.

PUBLICATIONS

PUBLISHED

- Giorgia Centonze, Dora Natalini, Alessio Piccolantonio, Vincenzo Salemme, **Alessandro Morellato**, Pietro Arina, Chiara Riganti and Paola Defilippi. Cholesterol and its derivatives: multifaceted players in breast cancer progression. Systematic Review, Front. Oncol. - Molecular and Cellular Oncology Received on: 28 Mar 2022, Accepted 15 Apr 2022.
- Camera M, Russo I, Zamboni V, Ammoni A, Rando S, **Morellato A**, Cimino I, Angelini C, Giacobini P, Oleari R, Amoruso F, Cariboni A, Franceschini I, Turco E, Defilippi P, Merlo GR. p140Cap Controls Female Fertility in Mice Acting via Glutamatergic Afference on Hypothalamic Gonadotropin-Releasing Hormone Neurons. Front Neurosci. 2022 Feb 14;16:744693. doi: 10.3389/fnins.2022.744693. PMID: 35237119; PMCID: PMC8884249.
- Giorgia Centonze, Jennifer Chapelle, Costanza Angelini, Dora Natalini, Davide Cangelosi, Vincenzo Salemme, **Alessandro Morellato**, Emilia Turco and Paola Defilippi The Scaffold Protein p140Cap as a Molecular Hub for Limiting Cancer Progression: A New Paradigm in Neuroblastoma Submitted: November 5th 2020Reviewed: February 3rd 2021 Published: March 10th 2021, DOI:10.5772/intechopen.96383
- Chapelle J, Baudino A, Torelli F, Savino A, **Morellato A**, Angelini C, Salemme V, Centonze G, Natalini D, Gai M, Poli V, Kähne T, Turco E, Defilippi P. The N-terminal domain of the adaptor protein p140Cap interacts with Tiam1 and controls Tiam1/Rac1 axis. Am J Cancer Res. 2020 Dec 1;10(12):4308-4324. PMID:33415001; PMCID: PMC7783762.
- Salemme V, Angelini C, Chapelle J, Centonze G, Natalini D, **Morellato A**, Taverna D, Turco E, Ala U, Defilippi P. The p140Cap adaptor protein as a molecular hub to block cancer aggressiveness. Cell Mol Life Sci. 2021 Feb;78(4):1355-1367. doi: 10.1007/s00018-020-03666-w. Epub 2020 Oct 20. PMID:33079227; PMCID: PMC7904710.

- Chapelle J, Sorokina O, McLean C, Salemme V, Alfieri A, Angelini C, **Morellato A**, Adrait A, Menna E, Matteoli M, Couté Y, Ala U, Turco E, Defilippi P, Armstrong JD. Dissecting the Shared and Context-Dependent Pathways Mediated by the p140Cap Adaptor Protein in Cancer and in Neurons. Front Cell Dev Biol. 2019 Oct 15;7:222. doi: 10.3389/fcell.2019.00222. PMID: 31681758; PMCID: PMC6803390.
- Grasso S, Cangelosi D, Chapelle J, Alzona M, Centonze G, Lamolinara A, Salemme V, Angelini C, **Morellato A**, Saglietto A, Bianchi FT, Cabodi S, Salaroglio IC, Fusella F, Ognibene M, Iezzi M, Pezzolo A, Poli V, Di Cunto F, Eva A, Riganti C, Varesio L, Turco E, Defilippi P. The SRCIN1/p140Cap adaptor protein negatively regulates the aggressiveness of neuroblastoma. Cell Death Differ. 2020 Apr;27(4):1448. doi:10.1038/s41418-019-0405-7.
- Russo I, Gavello D, Menna E, Vandael D, Veglia C, Morello N, Corradini I, Focchi E, Alfieri A, Angelini C, Bianchi FT, **Morellato A**, Marcantoni A, Sassoè-Pognetto M, Ottaviani MM, Yekhlef L, Giustetto M, Taverna S, Carabelli V, Matteoli M, Carbone E, Turco E, Defilippi P. p140Cap Regulates GABAergic Synaptogenesis and Development of Hippocampal Inhibitory Circuits. Cereb Cortex. 2019 Jan 1;29(1):91-105. doi: 10.1093/cercor/bhx306. PMID: 29161354.
- Alfieri A, Sorokina O, Adrait A, Angelini C, Russo I, **Morellato A**, Matteoli M, Menna E, Boeri Erba E, McLean C, Armstrong JD, Ala U, Buxbaum JD, Brusco A, Couté Y, De Rubeis S, Turco E, Defilippi P. Synaptic Interactome Mining Reveals p140Cap as a New Hub for PSD Proteins Involved in Psychiatric and Neurological Disorders. Front Mol Neurosci. 2017 Jun 30;10:212. doi:10.3389/fnmol.2017.00212. PMID: 28713243; PMCID: PMC5492163.

IN REVISION AND SUBMITTED

In revision on *Journal of Neuroscience*

- Costanza Angelini*, **Alessandro Morellato***, Annalisa Alfieri, Lisa Pavinato, Tiziana Cravero, Vincenzo Salemme, Dora Natalini, Giorgia Centonze, Alessandra Raspanti, Tina Garofalo, Donatella Valdembri, Guido Serini, Maurizio Giustetto, Emilia Turco, Paola Defilippi. p140Cap potentiates GluN2A-PSD95 association and increases NMDAR recruitment to synaptic lipid raft

Submitted on *Nature Communications*

- Vincenzo Salemme, Mauro Vedelago, Alessandro Sarcinella, Federico Moietta, Enrico Moiso, Giorgia Centonze, Marta Manco, Andrea Guala, Alessia Lamolinara, Costanza Angelini, **Alessandro Morellato**, Dora Natalini, Raffaele Calogero, Danny Incarnato, Salvatore Oliviero, Laura Conti, Manuela Iezzi , Daniela Tosoni, Giovanni Bertalot, Francesco De Sanctis, Cristina Frusteri, Stefano Ugel, Vincenzo Bronte, Federica Cavallo, Paolo Provero, Daniela Taverna, Emilia Turco, Professor Salvatore Pece, Paola Defilippi. The protein p140Cap imparts a protective immune response in the tumor microenvironment by reducing the cancer stem cell compartment through inhibition of the β-Catenin

Prepared for *International Journal of Molecular Sciences*

- Costanza Angelini*, **Alessandro Morellato***, Nikolina Stojanović, Andreja Ambriović Ristov, Emilia Turco, Paola Defilippi. Integrins role in synapse maintenance in health and disease

CONGRESS AND WORKSHOPS

- 6th EUROPEAN SYNAPSE MEETING 04-06/12/2017 Milano
- 11th FENS, Forum of Neuroscience 7-11/07/2018 Berlin
- ABCD, Signal transduction in Cancer, 22-24/11/2018 Torino
- PhD in Neuroscience Day, 01/03/2019 Torino
- Embo Workshop, 7-10/05/2019, Heraklion, Greece
- Guido Tarone Day, 16/05/2019, Torino
- 7th European Synapse Meeting, 02-04/09/2019 Lausanne
- FENS 2020 virtual forum 11-15/07/2020
- ASBMB virtual conference 30/06/2020, 01/07/2020, 07/07/2020
- Thermofisher “Stay Connected Webinar Tour”- 21/04/2020-07/05/2020
- Tarone Day, 17/05/2021
- Corso DAAD intensivo per Tedesco A1 18/03/20221 al 11/05/2021
- PhD Cross Boarder WorkShop 16/06/2021- 18/06/2021